

**Ana Beatriz Melo Villas Bôas**

***The impact of mesoscale eddies on the air–sea  
turbulent heat fluxes in the South Atlantic***

A thesis submitted to the Oceanographic  
Institute of the University of São Paulo,  
in partial fulfillment of the requirements  
for the degree of Master of Sciences in  
Oceanography, with emphasis in Physical  
Oceanography.

**Advisor:** Prof. Dr. Olga T. Sato

São Paulo

2014

UNIVERSITY OF SÃO PAULO  
OCEANOGRAPHIC INSTITUTE

*The impact of mesoscale eddies on the air–sea  
turbulent heat fluxes in the South Atlantic*

**Ana Beatriz Melo Villas Bôas**

A thesis submitted to the Oceanographic  
Institute of the University of São Paulo,  
in partial fulfillment of the requirements  
for the degree of Master of Sciences in  
Oceanography, with emphasis in Physical  
Oceanography.

Evaluated in \_\_\_\_ / \_\_\_\_ / \_\_\_\_\_ by

---

Prof. Dr.

---

Grade

---

Prof. Dr.

---

Grade

---

Prof. Dr.

---

Grade

*“Alone to go fast, together to go far.”  
To Guilherme.*

# Contents

	<b>Contents</b> . . . . .	<b>i</b>
	<b>List of Figures</b> . . . . .	<b>iii</b>
	<b>List of Tables</b> . . . . .	<b>viii</b>
<b>1</b>	<b>Introduction</b> . . . . .	<b>1</b>
1.1	Theoretical Background . . . . .	4
1.1.1	Air-Sea Heat Fluxes . . . . .	4
1.1.1.1	Sensible Heat Flux . . . . .	6
1.1.1.2	Latent Heat Flux . . . . .	6
1.1.2	The Dynamics of Mesoscale Eddies . . . . .	6
1.2	Thesis hypothesis and objectives . . . . .	10
<b>2</b>	<b>The South Atlantic Ocean</b> . . . . .	<b>11</b>
2.1	Mesoscale Eddies in the South Atlantic . . . . .	13
2.1.1	The Brazil–Malvinas Confluence . . . . .	14
2.1.2	The Agulhas Current Retroflexion . . . . .	16
<b>3</b>	<b>Data and Methods</b> . . . . .	<b>20</b>
3.1	Altimetry data and eddy identification . . . . .	20
3.1.1	Sea level anomaly data . . . . .	20
3.1.2	The Winding-Angle Method . . . . .	22
3.2	Surface turbulent heat fluxes data and anomalies . . . . .	24
3.2.1	Surface turbulent heat fluxes data . . . . .	25
3.2.2	Definition of the surface turbulent heat fluxes anomalies . . . . .	27
3.2.2.1	Moving Average Filters . . . . .	27
3.2.2.2	Composite maps . . . . .	30
3.2.2.3	Statistical Analysis . . . . .	31
<b>4</b>	<b>Results and Discussion</b> . . . . .	<b>32</b>
4.1	Characteristics of Mesoscale Eddies in the South Atlantic . . . . .	32
4.1.1	Eddy frequency and polarity . . . . .	32
4.1.2	Eddy Radius . . . . .	34
4.1.3	Eddy Amplitude . . . . .	35
4.2	Surface Turbulent Heat Fluxes Analysis . . . . .	41
4.2.1	Mean and Standard Deviation of the Surface Turbulent Heat Fluxes . . . . .	41
4.2.2	Geographical Distribution of the Mean Turbulent Heat Fluxes Anomalies Associated With Mesoscale Eddies . . . . .	46

4.2.3	Averaged Composite Maps . . . . .	52
<b>5</b>	<b>Conclusions and Future Work . . . . .</b>	<b>68</b>
	<b>A – The Okubo–Weiss method . . . . .</b>	<b>71</b>
	<b>Bibliography . . . . .</b>	<b>73</b>

# List of Figures

Figure 1	– The numerous processes by which the ocean and atmosphere interact. Illustration by Jayne Doucette, Woods Hole Oceanographic Institution (< <a href="http://www.whoi.edu/ooi_cgsn/page.do?pid=53278">http://www.whoi.edu/ooi_cgsn/page.do?pid=53278</a> >). . . . .	3
Figure 2	– Global zonal mean of the shortwave and longwave radiation, sensible and latent heat fluxes, and net surface heat flux. Positive fluxes are from the atmosphere to the ocean, and negative fluxes are in the opposite sense (Source: Talley <i>et al.</i> (2011)). . . . .	5
Figure 3	– Schematic representation of structure of an unstable growing meander closing off to form an eddy. Source: ??). . . . .	8
Figure 4	– Schematic representation of the structure of an anticyclonic (left) and a cyclonic (right) eddy in the southern hemisphere (adapted from Robinson (2010)). . . . .	9
Figure 5	– Schematic representation of the main surface currents of the South Atlantic Ocean. Black arrows represent the currents and the respective directions of the flow. The brackets near 50°S and 65°S mark the branches of the Antarctic Circumpolar Current. Shades of gray indicate the mean depth of the water column in meters, where white represents the open ocean, and dark-gray, the continents. Figure from Talley <i>et al.</i> (2011). . . . .	12
Figure 6	– Standard deviation ( $\sigma$ , in cm) of the sea level anomaly (SLA) over the South Atlantic between 1999 and 2009; Black contours correspond to $\sigma = 15$ cm and delimit the Brazil-Malvinas confluence region (BMC, contour 1) and the Agulhas Current Retroflexion region (AGR, contour 2). . . . .	13
Figure 7	– Mesoscale activity near the BMC region. The encounter of the relatively warm waters of the BC (reddish) with the relatively cold waters of the MC (greenish) creates instabilities that feature growing meanders which eventually close off and separate from the main current forming eddies. Figure from Olson <i>et al.</i> (1988) . . . . .	15
Figure 8	– Schematic representation of the dynamics near the AGR region. When the AC reaches the tip of Africa, it turns to the west and then retroflects back shedding anticyclonic Agulhas rings. The major currents are represented by thick black lines, the Agulhas rings are the solid anti-clockwise arrows and some cyclonic eddies are represented by dashed clockwise arrows. Figure from Talley <i>et al.</i> (2011). . . . .	17

Figure 9 – Timeline of all satellite altimetry missions since 1985. Colors indicate the repetition period of each satellite, which is the time it takes for the satellite to sample the same point again. Since 1992, it has been at least two altimeters operating at the same time. Figure obtained from: < <a href="http://www.pecad.fas.usda.gov/">http://www.pecad.fas.usda.gov/</a> > . . . . .	22
Figure 10 – Illustration of the eddy identification method of Chaigneau <i>et al.</i> (2009). The left panel is a snapshot of the SLA from AVISO corresponding to May 13, 2009. A zoom of the area limited by the dashed line is shown in the right panel, where the eddy centers are marked with black dots, and contours of cyclonic and anticyclonic eddies are drawn in blue and red, respectively. . . . .	25
Figure 11 – Graphical example of a Hann window given by Equation 3.4, with $l = 60$ . The left panel represents a two-dimensional window, while the right panel represents the same function in only one dimension. In both cases the window weight has its maximum value at the center ( $r = 0$ ), and decays to zero at $ r  = l$ . . . . .	28
Figure 12 – Example of the time filtering process applied to the LHF timeseries at ( $50^{\circ}\text{W}$ , $38^{\circ}\text{S}$ ). The upper panel shows three years of the original LHF timeseries (grey line), and the corresponding long period signal ( $T \geq 90$ ), calculated by the filter (thick black line). A zoom for the period marked by the red lines in the upper panel (Jan 2007 – Sep 2007) is shown in the lower panel. The dashed line corresponds to the original signal minus the long-period variabilities. The mesoscale component is shown in the thin black line. . . . .	29
Figure 13 – Steps for the definition of the surface heat fluxes anomalies in relation to a large-scale reference level. To illustrate, the contour a chosen eddy is drawn in solid black and its center marked with a dot. Points within a radius of 600 km from the eddy center are limited by the dashed circle, that corresponds to the window length. In this example the colors in all panels represents the LHF. Panel (A) is the time-filtered signal, which still contains large-scale spatial patterns. Panel (B) is the same map as panel (A), but with all gridpoints inside eddies set to mask. Panel (C) is the output from the spatial filter, corresponding to spatial scales larger than 600 km. Panel (D) is the anomaly map obtained by the subtraction of the large-scale smoothed maps (C) from the time-filtered maps (A). . . . .	30

Figure 14 – Example of the eddy normalization method, applied to construct the composite maps. To let it more explicit, the example is shown for the SLA field. The left panel shows the contour (solid black line) and the center (red dot) of an eddy in the original spatial coordinate system (latitude, longitude). The field inside the region limited by twice the eddy contour is then interpolated onto a high resolution regular grid, normalized by the distance between the eddy center and the edge in each direction. The result of such normalization is shown in the right panel, where the dashed circle limits the eddy interior. . . . .	31
Figure 15 – Map of the eddy frequency (in %) for the SA, which represents the percentage of time that the grid points are within an eddy. In the SA eddies can occur up to 70% of the time near the energetic regions of the BMC and AGR, while the frequency strongly weakens north of 20° S.	33
Figure 16 – Polarity map for the eddies in the SA. Red (blue) regions, with $p > 0$ ( $p < 0$ ), are characterized by a predominance of anticyclonic (cyclonic) eddies over cyclonic (anticyclonic). . . . .	34
Figure 17 – Mean eddy radii, on the top panel. In the bottom panel it is shown the comparison between the zonal mean of the first baroclinic mode of the Rossby radii ( $Rd_i$ ) (gray) and the zonal mean of the eddy radii (blue), as a function of latitude. The values for $Rd_i$ were obtained from (CHELTON <i>et al.</i> , 1998). . . . .	36
Figure 18 – Global distribution of the mean eddy scale (equivalent to the eddy radius) from Chelton <i>et al.</i> (2011b) (left). The right panel shows the zonally averaged eddy scale (solid black line) and the zonally averaged $Rd_i$ (short dashed line). . . . .	37
Figure 19 – Distribution of the eddy radius for cyclonic (blue) and anticyclonic eddies (red). The mode of the distribution for cyclonic eddies is $\sim 70.8$ km and for anticyclonic eddies is $\sim 72$ km. . . . .	38
Figure 20 – Geographical distribution of the mean eddy amplitude in the SA. . . .	38
Figure 21 – Distribution of the eddy amplitude for cyclonic (blue) and anticyclonic eddies (red). The mode of the distribution for both polarities is $\sim 3$ cm. . . . .	39
Figure 22 – Zonally averaged eddy amplitude as a function of latitude (solid black line) and the respective interquartile range (25% –75%), in gray, and standard deviation, in the dashed line. . . . .	39
Figure 23 – Mean eddy amplitude (left) and zonally averaged amplitude (right) from Chelton <i>et al.</i> (2011b). In the right panel the mean is shown in the solid black line, the standard deviation, in the dashed line, and the interquartile (25% –75%,) in the gray shadow. . . . .	40

Figure 24 – Temporal mean (A) and standard deviation (B) of the LHF in the SA, for the period from 1999 to 2009, in $W/m^2$ . Positive upward fluxes indicate ocean heat loss, while downward negative, ocean heat gain. . . . .	42
Figure 25 – Same as Figure 24, but for the SHF. . . . .	43
Figure 26 – Maps of the mean surface turbulent heat fluxes averaged for the summer (January) and winter (August). Results for the LHF are shown in the left panels and for the SHF in the right panels. . . . .	44
Figure 27 – Zonally averaged surface turbulent heat fluxes in the SA. The LHF is shown in solid black, the SHF in light grey and, the sum of the two in the dashed line. . . . .	45
Figure 28 – Mean surface turbulent heat fluxes anomalies associated with mesoscale eddies in the South Atlantic. Mean latent heat flux (LHF, in $W/m^2$ ) anomalies within (A) anticyclonic and (B) cyclonic eddies. Mean sensible heat flux (SHF, in $W/m^2$ ) anomalies within (C) anticyclonic and (D) cyclonic eddies. . . . .	49
Figure 29 – Maps of the mean LHF anomaly (top) for the combined contribution of cyclonic and anticyclonic eddies (A), and for gridpoints outside eddies (B). Mean SHF anomaly (bottom) for the combined contribution of cyclonic and anticyclonic eddies (C), and for gridpoints outside eddies (D). . . . .	51
Figure 30 – Maximum (minimum, for cyclonic eddies) surface turbulent heat fluxes anomalies within anticyclonic (red lines) and cyclonic (blue lines) eddies as a function of the eddy amplitude. The solid and dashed lines are the LHF and SHF, respectively. Mean turbulent heat fluxes anomalies were computed by individually averaging each subgroup of normalized maps. . . . .	54
Figure 31 – Averaged composite maps of LHF (A, B) and SHF (E, F) anomalies associated with anticyclonic (A, E) and cyclonic (B, F) eddies. Composites were obtained from eddies having the 5% highest absolute amplitudes ( $\geq 27.3$ cm) that corresponds to 4564 cyclonic and 3974 anticyclonic eddies. The axes in the maps are the normalized distance $d$ between the eddy center ( $d = 0$ ) and twice the eddy edge ( $d = 2$ ). Contour intervals are shown every $2 W/m^2$ . Panels (C, D) show the absolute value of the zonal and meridional profile of the LHF anomalies in the composites, respectively. Profiles were traced crossing the point of maximum (minimum for cyclones) anomalies. Anomalies of anticyclonic eddies are in red lines, and cyclonic eddies in blue lines. The positions where the extreme values in the profiles occur, are marked by a dashed line. Panels (G, H) are the same, for the SHF. . . . .	57

Figure 32 – Similar to Figure 31, but for eddies with amplitudes in the 90–95 <sup>th</sup> percentile range (18.8–27.3 cm). Contour intervals in the composite maps are shown every 1 W/m <sup>2</sup> . . . . .	58
Figure 33 – Similar to Figure 31, but for eddies with amplitudes between 12.1–18.8 cm, corresponding to ~8600 anticyclonic and ~9000 cyclonic eddies. Contour intervals in the composite maps are shown every 0.4 W/m <sup>2</sup> . . . . .	59
Figure 34 – Similar to Figure 33, but for eddies with amplitudes between 8.9–12.1 cm. Contour intervals in the composite maps are shown every 0.3 W/m <sup>2</sup> . . . . .	60
Figure 35 – Similar to Figure 33, but for eddies with amplitudes between 6.8–8.9 cm. Contour intervals in the composite maps are shown every 0.3 W/m <sup>2</sup> . . . . .	61
Figure 36 – Similar to Figure 33, but for eddies with amplitudes between 5.4–6.8 cm. Contour intervals in the composite maps are shown every 0.3 W/m <sup>2</sup> . . . . .	62
Figure 37 – Similar to Figure 33, but for eddies with amplitudes between 4.3–5.4cm. Contour intervals in the composite maps are shown every 0.2 W/m <sup>2</sup> . . . . .	63
Figure 38 – Similar to Figure 33, but for eddies with amplitudes between 3.5–4.3 cm. Contour intervals in the composite maps are shown every 0.2 W/m <sup>2</sup> . . . . .	64
Figure 39 – Similar to Figure 33, but for eddies with amplitudes between 2.9–3.5 cm. Contour intervals in the composite maps are shown every 0.2 W/m <sup>2</sup> . . . . .	65
Figure 40 – Similar to Figure 33, but for eddies with amplitudes between 2.4–2.9 cm. Contour intervals in the composite maps are shown every 0.2 W/m <sup>2</sup> . . . . .	66
Figure 41 – Similar to Figure 33, but for eddies with amplitudes between 2.1–2.4 cm. Contour intervals in the composite maps are shown every 0.2 W/m <sup>2</sup> . . . . .	67

# List of Tables

Table 1	– List and description of the parameters obtained from the AVISO SLA maps by the pre-processing routine of the Chaigneau <i>et al.</i> (2009) eddy identification algorithm. . . . .	23
Table 2	– List and description of the parameters obtained by the eddy identification algorithm. For each eddy, it is possible to assess its respective radius, amplitude and contour, which are the most important variables for this work. . . . .	24
Table 3	– Anticyclonic (Cyclonic): Mean and maximum (minimum) values of LHF and SHF anomalies associated with anticyclonic (cyclonic) eddies observed in the BMC and AGR regions. For the whole SA just the mean is shown. Annual Range: large-scale LHF and SHF annual cycle. Exp. Var.: mean and maximum percentage of the variance of the total LHF and SHF signals explained by the variance of the heat fluxes anomalies caused by the eddies. All values are statistically significant at the 95% confidence level. . . . .	50
Table 4	– Eddy amplitude range representative for each percentile, calculated with a 10% increment from each other, except for the 90–95 <sup>th</sup> and 95–100 <sup>th</sup> , that have a 5% interval. . . . .	52

There are the rushing waves  
mountains of molecules  
each stupidly minding its own business  
trillions apart  
yet forming white surf in unison.

Ages on ages  
before any eyes could see  
year after year  
thunderously pounding the shore as now.  
For whom, for what?  
On a dead planet  
with no life to entertain.

Never at rest  
tortured by energy  
wasted prodigiously by the sun  
poured into space.  
A mite makes the sea roar.

Deep in the sea  
all molecules repeat  
the patterns of one another  
till complex new ones are formed.  
They make others like themselves  
and a new dance starts.

Growing in size and complexity  
living things  
masses of atoms  
DNA, protein  
dancing a pattern ever more intricate.

Out of the cradle  
onto dry land  
here it is  
standing:  
atoms with consciousness;  
matter with curiosity.

Stands at the sea,  
wonders at wondering: I  
a universe of atoms  
an atom in the universe.

*Richard. P. Feynman*

*In "What do you care what other people think"*

# Acknowledgements

Foremost I would like to thank to my advisor Professor Olga T. Sato for taking me as her student and first introducing me to physical oceanography. During the past two years she gave me all her support and unconditional trust, always wisely balancing between guiding me through science and letting me think independently. This work is my humble way to give back. I am also very thankful to Professor Paulo Polito for always giving up of his time to answer my (several) curious questions.

When I started my master I couldn't imagine that I would get a "combo" advisory. I feel very lucky for having the chance to collaborate with Dr. Alexis Chaigneau during my internship at the "Laboratoire d'Etudes en Geophysique et Oceanographie Spatiales" (LEGOS) in Toulouse, France. Dr. Chaigneau have never measured any effort to help me in all ways. His enormous ability of getting work done have strongly influenced me and shaping the kind of scientist I want to become. Our fruitful discussions were essential for the development of this work and I will be always deeply thankful for that.

I also thank the Oceanographic Institute of the University of São Paulo (IOUSP) and all the professors and staff that contributed to my formation. Very specially, I deep thank to Professor Ilson da Silveira, who was with no doubts, responsible for teaching me most of the physical oceanography that I know today and who have always encouraged me to pursue my goals. I will always remember with care his enthusiastic lectures and wise advices. To all my colleagues from IOUSP, who shared with me good coffees and not so good homework assignments during many weekends. Specially, to my buddies Gilberto Watanabe and Patrícia Baldasso, for the waves, cakes, laughs, beers and arms, with big hugs.

Even far from my hometown all these years, I cannot forget those who have shared with me the best moments of my youth and who have broadly influenced my values and personality. Thanks to Hanoch Griner, Alan Michel, Paulo Maurício and Bárbara Felipe: *I get by with a little help from my friends*. Also thanks to my very dear "complex conjugate" friend, José Dias Neto. You are my inspiration of persistence and simplicity. I know I can count on you always, and I am very proud of what we have become. I thank to Professor Enivaldo Bonelli who have always remembered me to never forget the big picture and notice the beauty of nature around us.

I deeply thank to my parents, Hilton Villas Bôas and Lygia Melo, for their respect, support and unconditional love. To my sisters, Gabriella e Bianca Villas Bôas, for the most true and beautiful friendship. To my grandparents, Zulmira e Sebastião Villas Bôas, for always sharing their wisdom with me and forgiving me for spending so much time without

calling. To my grandmother, Maria José Melo, for putting my dreams before everything else. I would not be where I am today if wasn't for her care. Thanks to my mirror, uncle Dr. Claudio Melo, the greatest scientist and human being that I know. Whom since I was a little kid, taught me lessons about nature, kindness, respect and who showed me the way of the empty hand. To my aunt Lucivanda, for keeping remembering me to follow my heart.

This work would not have been possible without the intellectual and emotional support of the only one who was every single day by my side, regardless of my mood and patience. My most deep and sincere thanks to Guilherme Pimenta Castelão: my co-worker, husband, and partner in life. No calm seas make good sailors. I will always be indebted to you for crossing those storms with me. O nosso carnaval está pra chegar.

During my master I was funded by the São Paulo Research Agency (FAPESP). I sincerely thank to FAPESP for the financial support under grants 2012/21243-6 (MSc scholarship) and 2013/02355-0 (BEPE).

# Abstract

By collocating 10 years (1999–2009) of remotely sensed surface turbulent heat fluxes with satellite altimetry data, we investigate the impact of ocean mesoscale eddies on the latent and sensible heat fluxes in the South Atlantic ocean. Eddies were identified using the method proposed by Chaigneau *et al.* (2009), which is based on closed contours of sea level anomaly. Most of the identified eddies had a radius of  $\sim 70$  km and amplitude of  $\sim 5$  cm. On average, in the South Atlantic, eddies play a minor role on the ocean–atmosphere heat exchange. However, in strongly energetic regions such as the Brazil–Malvinas confluence or Agulhas Current retroflexion regions, eddies can account up to 20–30% of the total variance of the surface turbulent heat fluxes with averaged anomalies of  $\pm 10$ – $20$  W/m<sup>2</sup> for both heat flux components. Cyclonic (anticyclonic) eddies, associated with negative (positive) heat fluxes anomalies tend to cool (warm) the overlying atmosphere. A composite analysis of the turbulent heat fluxes anomalies within the eddies reveals a direct relationship between the eddy amplitude and the intensity of the latent and sensible fluxes anomalies, such that large–amplitude eddies have a stronger signature in the turbulent surface heat fluxes. Heat fluxes anomalies are also much stronger near the eddy centers and decay radially to reach minimum values outside the eddies.

**Key-words:** Mesoscale eddies. Surface turbulent heat fluxes. South Atlantic. Air–sea interactions.

# Resumo

Uma combinação de 10 anos (1999–2009) de fluxos turbulentos de calor pela superfície, medidos a partir de satélites, e dados altimétricos de anomalia da altura da superfície do mar, foram utilizados com objetivo de investigar o impacto de vórtices de meso–escala nos fluxos de calor sensível e latente na bacia do Atlântico Sul. Para a detecção dos vórtices foi aplicado o método proposto por Chaigneau *et al.* (2009), que baseia-se em contornos fechados de anomalia da altura da superfície do mar. A maior parte dos vórtices identificados possui raio de  $\sim 70$  km e amplitude de  $\sim 5$  cm. Em média, no Atlântico Sul, o impacto dos vórtices para as trocas de calor entre oceano e atmosfera é relativamente fraco. Entretanto, em regiões de alta variabilidade energética como na Confluência Brasil–Malvinas e na retroflexão da Corrente das Agulhas, vórtices de meso–escala podem contribuir com anomalias médias de até  $\pm 10$ – $20$  W/m<sup>2</sup> nos fluxos turbulentos. Vórtices ciclônicos (anti–ciclônicos), associados com anomalias negativas (positivas) de fluxos de calor, tendem a esfriar (esquentar) a atmosfera adjacente. Mapas *composite* foram analisados para milhares de vórtices, mostrando uma relação direta entre a magnitude das anomalias dos fluxos e a amplitude dos vórtices, de tal modo que vórtices de maior amplitude contribuem com maiores anomalias de calor latente e sensível. Além disso, os padrões espaciais dos *composites* médios revelam que as anomalias são significativamente maiores próximo ao centro dos vórtices e decaem radialmente até atingirem valores absolutos mínimos fora dos contornos dos vórtice.

**Palavras-chaves:** Vórtices de meso–escala. Fluxos turbulentos de calor pela superfície. Atlântico Sul. Interações oceano–atmosfera.

# 1 Introduction

The Earth's climate is forced by the energetic balance between ocean, atmosphere, and land. Such balance is driven by processes that couple those three systems and it is dominated by the incoming energy radiated by the sun (TRENBERTH *et al.*, 2009). Nearly half of this energy is absorbed at the Earth's surface as shortwave radiation and about 20% of the absorbed energy is emitted back to the atmosphere and space as outgoing longwave radiation. Because of the Earth's sphericity and the inclination of its rotation axis, the incoming solar radiation is unevenly distributed around the globe, depending mostly on latitude and the season of the year. The angle of incidence of solar radiation decreases with latitude, thus the incoming shortwave radiation per unit area decreases from the equator to the poles. This promotes a meridional temperature gradient, with lower average temperatures in polar regions and higher average temperatures in equatorial regions. However, because of the ocean's circulation, this temperature gradient is redistributed by ocean currents, that transport warm equatorial waters to higher latitudes. Owing the water's high heat capacity, the ocean has a great potential of heat storage, accumulating heat during the summer and releasing it to the atmosphere during the winter. In that way the ocean behaves as reservoir, that minimizes seasonal temperature changes. Indeed, the annual amplitude of temperature in coastal regions is much lower than in interior regions.

The ocean and the atmosphere interact in a number of forms, exchanging energy, momentum, and gases at the air–sea interface (Figure 1). In addition to the transfer of heat through incoming and outgoing radiation, turbulent heat exchanges also occur at the sea surface in the form of sensible and latent heat, associated with conduction, evaporation, and precipitation. Such fluxes are a fundamental part of the ocean surface heat budget (YU; WELLER, 2007), being one of the primary means by which the ocean releases heat to the atmosphere (CAYAN, 1992). The incoming radiation from the sun also forces the winds that, in turn, transfer momentum to the ocean and drives the ocean surface currents. In addition, the winds force surfaces waves, that in storm conditions can break and exchange momentum with the atmosphere in the form of aerosols and sprays. Such highly turbulent coupling is fundamental to the dynamics of both fluids, being responsible for triggering a variety of climatic phenomena at scales comprehending from synoptic to interannual scale (POND, 1971).

The complexity of air–sea interactions becomes even greater when considering the possible feedbacks involved. An anomaly on the sea surface temperature (SST), for example, can promote diabatic cooling or heating of the overlying atmosphere, that impact the wind stress and the heat fluxes. As a response, the winds impact back the sea surface

and the thermohaline structure below, which can act to reinforce or attenuate the original SST anomaly (FEDOROV, 2008). Due to the relatively coarse resolution of observations, whether in time or space, air–sea interactions were for long explored mostly on synoptic and large scales. Weare (1984), for example, used marine weather reports from 1957 to 1976 to explore interannual variations of the sea surface specific humidity and latent heat flux (LHF). The author proposed that such variations were linked to the El Niño Southern Oscillation (ENSO) phenomenon, in a way that during ENSO, changes in SST precede changes in the LHF. Similar results were also presented by Rasmusson and Carpenter (1982), that found anomalies in the surface wind and SST preceding ENSO events.

The variability of the LHF in the tropical and subtropical ocean was explored by Liu and Curry (2006). The authors compared the decadal trend and interannual variability of the LHF from satellite–based and reanalysis products for the period between 1989–2000. They found a positive trend in the LHF present in all datasets, that reached values as high as  $17 \text{ W/m}^2$  per decade, and that was associated with an increasing trend on the wind speed. In agreement with the results of Liu and Curry (2006), Yu and Weller (2007) also found a positive trend in the global LHF from the *Objectively Analyzed Air–Sea Fluxes* (OAFlux) project. The authors have estimated that between 1981 and 2002 the LHF increased by  $9 \text{ W/m}^2$ , which corresponded to about 10% of the mean value. These increasing in the LHF was also accompanied by a positive trend in the wind speed and in SST, which suggested a response from the atmosphere to oceanic forcing.

Exploring the other extreme of the spectrum, Neiman and Shapiro (1993) analyzed wind, temperature, and sea level pressure anomalies precursor to the genesis of an extratropical marine cyclone near the Gulf Stream. Near the cyclone core, the authors reported fluxes of sensible and latent heat from the ocean surface to the atmosphere exceeding  $300 \text{ W/m}^2$  and  $1000 \text{ W/m}^2$ , respectively, with associated air minus sea temperature of  $-5^\circ\text{C}$  and air minus sea moisture of  $-6 \text{ g kg}^{-1}$ , which reflected the extreme variability associated with the cyclone passage. An example of complex feedbacks that can result from air–sea interactions was given by Dewar and Flierl (1987), that were the first to describe how the wind responds, locally, to the presence of mesoscale oceanic eddies. The authors have conducted numerical experiments to analyze the effects of the wind on a Gulf Stream ring, concluding that eddies not only impact the wind stress, because of the top drag, but also that the resulting stress has consequences for the eddy propagation and decay, such as shifting the eddy trajectory. However, it was only with the advent of satellite altimeters, radiometers, and scatterometers that the influence of mesoscale features on the ocean–atmosphere processes could start to be better explored. It is known nowadays that mesoscale eddies are omnipresent in the world’s ocean (MORROW; TRAON, 2006; FU *et al.*, 2010). As a consequence, extensively work have been done to determine their role on the ocean and atmosphere dynamics and fluxes, as presented bellow.

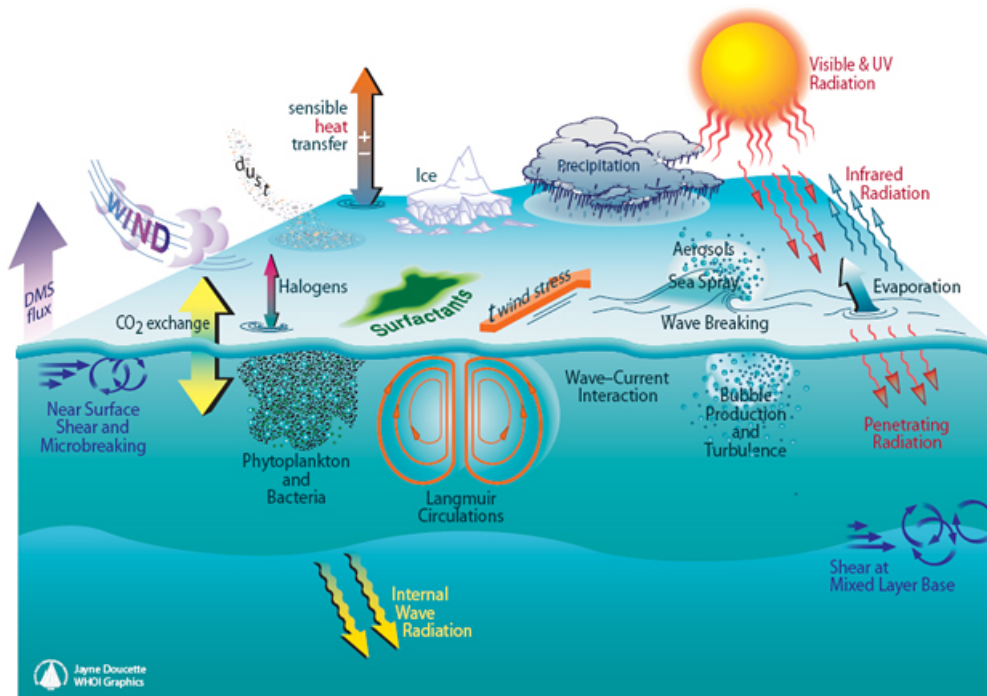


**Figure 1** – The numerous processes by which the ocean and atmosphere interact. Illustration by Jayne Doucette, Woods Hole Oceanographic Institution (<[http://www.whoi.edu/ooi\\_cgsn/page.do?pid=53278](http://www.whoi.edu/ooi_cgsn/page.do?pid=53278)>).

Recent work by Chelton and Xie (2010) analyzed the coupling between ocean and atmosphere at mesoscales. By using SST from radiometer and wind measurements from scatterometer, the authors investigated how changes in the SST are correlated with surface winds. They argued that this correlation comes as a response of the air humidity and temperature to latent and sensible heat fluxes. Looking at eddies specifically, Frenger *et al.* (2013) were able to depict the signature of these features not only on the SST and surface wind, but also on cloud coverage and rain rate. They found that eddies were capable to cause an anomaly of approximately  $\pm 5^{\circ}\text{C}$ , where positive anomalies were associated with anticyclonic eddies and negative anomalies with cyclonic eddies. Such SST anomalies were positively correlated with anomalies in other atmospheric properties. The authors remark that the atmospheric response to the eddy-induced anomalies could be important to numerical models, as well as to the oceanic uptake of carbon dioxide. The impact of eddies on the SST field were also explored by (HAUSMANN; CZAJA, 2012). The authors identified mesoscale eddies from altimetry data in the North Atlantic and Southern ocean and used SST from microwave radiometer to construct composite maps of the SST anomalies associated with eddies. They pointed out that the signature of eddies on the SST is nearly in-phase with sea surface height (SSH) anomalies for eddies detected in energetic region. However, for eddies detected in quiescent regions the anomalies were not only much weaker, but also in quadrature with SSH anomalies. From this asymmetry, the authors were capable to estimate the meridional heat flux associated

with cyclonic and anticyclonic eddies. Although mesoscale eddies are currently known to impact the ocean surface and the overlying atmospheric boundary layer, their role on the heat exchanges at the air–sea interface remains unclear. The need to well understand the physical processes driving these exchanges goes over the representation of mesoscale dynamics itself. Anomalies related to eddies could be strong enough to impact beyond the boundary layer, and thus could affect the large–scale atmospheric circulation. Hence, the accuracy of coupled climate models would be dependent of how well these interactions are represented.

This work is motivated by some questions that are still to be answered: (i) Do eddies have an imprint on the surface turbulent heat fluxes? (ii) Are they able to impact the surface heat fluxes variability? (iii) How are the eddy surface heat fluxes anomalies geographically distributed? In the following section (Section 1.1), I provide the theoretical background necessary to describe the structure and dynamics of mesoscale eddies, as well as to understand the turbulent heat exchanges at the air–sea interface. Then, in Section 1.2, I state the hypothesis and the objectives of the present work. A brief review on the dynamics of the South Atlantic ocean and the previous studies observing mesoscale eddies in the study area is presented in Chapter 2. In Chapter 3, the data and methods used to identify the eddies, and assess their imprints on the surface turbulent heat fluxes are described. Results are presented and discussed in Chapter 4, where I first analyze the mean characteristics of the identified eddies (Section 4.1), and then their anomalies on the surface turbulent heat fluxes (Section 4.2). Finally, in Chapter 5, I present the conclusions and some suggestions for prospective work.

## 1.1 Theoretical Background

### 1.1.1 Air-Sea Heat Fluxes

The heat budget at the air–sea interface ( $Q_{net}$ ) is generally given by the balance between the incoming solar radiation ( $Q_{in}$ ) absorbed by the ocean, and the outgoing ( $Q_{out}$ ) energy lost by the ocean:

$$Q_{net} = Q_{in} - Q_{out}. \quad (1.1)$$

Considering the terms that contribute to heat gain and loss at the ocean’s surface, equation 1.1 can be rewritten as:

$$Q_{net} = \underbrace{Q_s + Q_b}_I + \underbrace{Q_h + Q_e}_{II}, \quad (1.2)$$

where ( $Q_s$ ) is the shortwave radiation, ( $Q_b$ ) is the longwave radiation,  $Q_h$  is the sensible heat flux, and  $Q_e$  is the latent heat flux. Thus the ocean surface heat budget accounts for how much of the energy absorbed by the ocean is emitted back to the space, and how much is lost to the atmosphere as latent and sensible heat. The terms over the brace  $I$  are the radiative components of the surface heat budget. Mostly of the heat gained by the ocean comes as shortwave radiation from the sun ( $Q_s$ ), which is the greatest component on the budget (Figure 2). The amount of shortwave radiation absorbed at the ocean's surface depends on the albedo, that measures how much of the incoming radiation is reflected back to the atmosphere and space. As all bodies with temperatures higher than 0 K, the ocean radiates energy at a rate that depends of its temperature. This rate can be obtained by the Stefan–Boltzmann law, which states that the radiation is proportional to the fourth power of the temperature:  $Q_b \propto T^4$ , where  $T$  is the temperature. Considering the mean temperature of the ocean, it radiates energy in the infrared band of the spectrum, thus the term  $Q_b$  in Equation 1.2 is referred as the longwave radiation. Part of the the longwave radiation can be absorbed by the atmosphere and emitted back to the ocean, although most of it is lost to space.

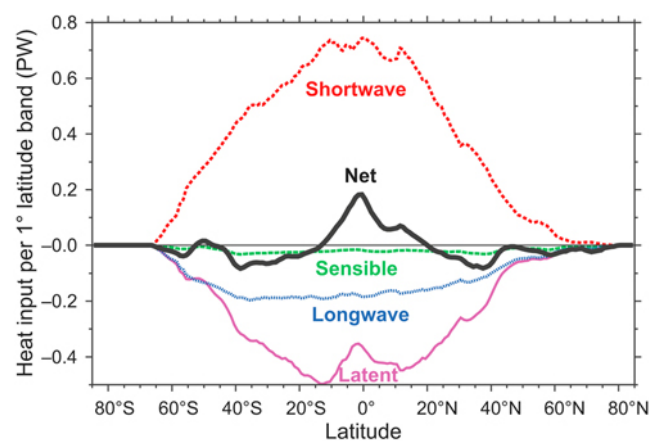


**Figure 2** – Global zonal mean of the shortwave and longwave radiation, sensible and latent heat fluxes, and net surface heat flux. Positive fluxes are from the atmosphere to the ocean, and negative fluxes are in the opposite sense (Source: Talley *et al.* (2011)).

The ocean and atmosphere also exchange heat by conduction and evaporation. These exchanges are driven by turbulent processes involving oceanic and atmospheric properties. The terms over the brace  $II$  in Equation 1.2 are the turbulent components of the surface heat budget. Turbulent fluxes can not be measured directly. They are inferred from bulk formulae that typically involve the product of transfer coefficients with the gradient between air and sea of a property related to the a given flux (ROBINSON, 2010). The surface turbulent heat fluxes are crucial to the heat budget. As emphasized by Cayan (1992), the latent (LHF) and sensible (SHF) heat fluxes together are the primary process by which the ocean releases heat to the atmosphere. In addition, most of the variability of

the net surface heat flux is driven by the variability of the LHF (CHOU *et al.*, 2004).

#### 1.1.1.1 Sensible Heat Flux

The SHF results from the heat conduction due to the difference of temperature between the sea surface and the overlying atmosphere. The energy flows from warmer to cooler surfaces until an state of equilibrium is reached. On average, the SHF is positive, meaning that the heat flux is from the ocean to the atmosphere (ocean heat loss). The parameterization of SHF is given by the following equation (LIU *et al.*, 1979):

$$Q_h = \rho_{air} c_p C_h u (T_s - T_a), \quad (1.3)$$

where  $\rho_{air}$  is the density of air,  $c_p$  is the specific heat of air,  $C_h$  transfer coefficient for sensible heat,  $u$  is the wind speed at 10 m height,  $T_s$  is the sea surface temperature, and  $T_a$  is the potential air temperature at 10 m. It is important to note that the bulk formulae here presented, and the heat fluxes analyzed in this work, consider upward positive fluxes. In other words, positive fluxes are from the ocean to the atmosphere while negative fluxes are from the atmosphere to the ocean.

#### 1.1.1.2 Latent Heat Flux

The LHF at the ocean–atmosphere interface is associated with water phase changes from liquid to vapor and vice versa. The ocean loses heat to the atmosphere as water evaporates, thus the LHF commonly has a positive sign, meaning that the heat flux via latent heat is from the ocean to the atmosphere. The bulk parameterization of the LHF is given by:

$$Q_e = \rho_{air} C_e u (q_s - q_a) L, \quad (1.4)$$

where  $\rho_{air}$  is the density of air,  $C_e$  transfer coefficient for latent heat,  $u$  is the wind speed at 10 m,  $q_s$  is the saturated specific humidity at the sea surface temperature, and  $q_a$  is the measured air specific humidity at 10 m height.

### 1.1.2 The Dynamics of Mesoscale Eddies

The ocean circulation is dominated by mesoscale variability that can feature meanders, rings eddies and fronts. Mesoscale eddies are quasi–circular rotating structures having typical horizontal scales of tens to hundreds of kilometers and time scales ranging from weeks to months. They separate from the mean flow due to instability process, which makes them more likely to occur in regions of strong currents. The first observations of mesoscale eddies goes back to the late 1940’s, when Fuglister (1972) followed a cold core

Gulf Stream ring. Today, with the technology of satellite altimeters it became possible to monitor eddies globally, and it is currently common sense that these are ubiquitous features in the world's ocean.

From Newton's second law, the equation of motion for a inviscid, incompressible, and homogeneous, geophysical fluid can be written as:

$$\frac{\partial \vec{V}}{\partial t} + (\vec{V} \cdot \vec{\nabla}) \vec{V} + 2\vec{\Omega} \times \vec{V} = -\frac{1}{\rho} \vec{\nabla} p + \vec{g} \quad (1.5)$$

where,  $\vec{V}$  is the velocity vector,  $t$  is the time,  $\vec{\Omega}$  is the angular velocity of Earth,  $\rho$  is the fluid density,  $p$  is the pressure, and  $\vec{g}$  is the gravity acceleration vector. For dynamical processes with time scales much longer than the inertial period (or small Rossby numbers  $Ro, Ro_T \ll 1$ ), the dominant balance in Equation 1.5 is between the Coriolis force and the pressure gradient force. In this case, the fluid is in geostrophic balance and the horizontal flow can be expressed by:

$$\begin{aligned} fu &= -\frac{1}{\rho} \frac{\partial p}{\partial y}, \\ fv &= \frac{1}{\rho} \frac{\partial p}{\partial x}, \end{aligned} \quad (1.6)$$

where  $u$  and  $v$  are the horizontal components of the geostrophic velocity,  $f$  is the Coriolis parameter, and  $x$  and  $y$  are the longitudinal and meridional distances, respectively. Furthermore, the pressure is related with the sea level anomaly  $\eta$  and the acceleration of gravity ( $g$ ) by  $p = \rho\eta g$ , therefore we can write the components of the geostrophic velocity as:

$$\begin{aligned} u &= -\frac{g}{f} \frac{\partial \eta}{\partial y}, \\ v &= \frac{g}{f} \frac{\partial \eta}{\partial x}. \end{aligned} \quad (1.7)$$

In the presence of a strongly sheared or stratified flow, the geostrophic balance cannot be maintained, giving rise to instability processes. In regions of western boundary currents for example, barotropic and baroclinic instabilities promote the meandering of the current. As these meanders grow, they are likely to close off and separate from the mean flow, originating an eddy (Figure 3). Moreover, eddies can also result from the intrusion of a parcel of water in a region with very distinct temperature and salinity characteristics, such is the case in the region of the Agulhas Current leakage. The Agulhas current brings warm water from the Indian Ocean into the cooler South Atlantic, shedding eddies (OLSON, 1991).

If we had to make a recipe to create eddies, the primary ingredient would be rotation. Once eddies separate from the mean flow, trapping water from the original currents, they

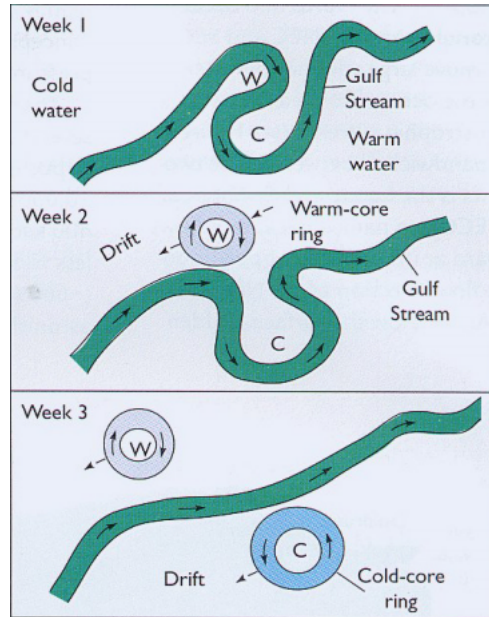


**Figure 3** – Schematic representation of structure of an unstable growing meander closing off to form an eddy. Source: ??).

can generally be classified in two types: cold core and warm core eddies. Cold core eddies, are characterized by negative sea level anomalies and cyclonic rotation, while warm core eddies are characterized by positive sea level anomalies and anticyclonic rotation. If there was no Coriolis effect, the sea level anomalies would rapidly dissipate and propagate as surface gravity waves. However, in the rotating frame, once the flow is started by the pressure gradient force, the Coriolis force acts to the left (Southern Hemisphere) or to the right (Northern Hemisphere) of the flow, shifting it from its original direction. In that way it is established a rotating flow around the horizontal pressure gradient that can be sustained for several weeks. For all these arguments to be valid, eddies must have a proper time and length scale, so they can be affected by Earth rotation. This scale is given by the baroclinic Rossby radius of deformation ( $Rd_i$ ), that is the scale by which the tendency of gravity to dissipate the pressure perturbation is compensated by the effect of the Coriolis acceleration:

$$Rd_i = \frac{\sqrt{g'D}}{f_0}, \quad (1.8)$$

where  $g'$  is the reduced gravity,  $D$  is the depth of the mixed layer, and  $f_0$  is the Coriolis parameter.

In contrast to linear waves, efficient only in transporting energy, eddies are also capable of transporting matter. As a consequence, they can carry salt (CHAIGNEAU *et al.*, 2011), heat (SOUZA *et al.*, 2011a), and biological tracers (GAUBE *et al.*, 2013) along their trajectories, strongly influencing oceanic budgets. Moreover, eddies exhibit distinct thermohaline vertical structures than the surrounding ocean, impacting the density field. Cold core eddies are marked by a positive density and negative temperature anomalies.

The doming of the isopycnals brings cooler and denser water closer to the surface and dips down the sea surface (Figure 4). The opposite is true for warm cores.

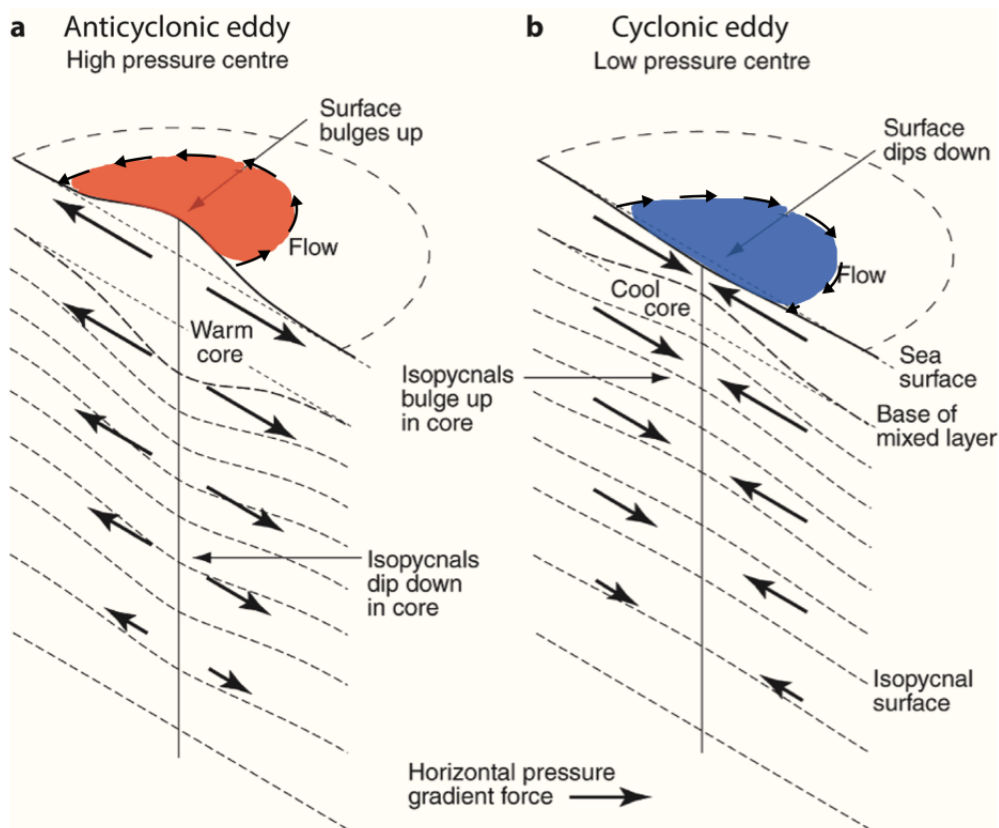


**Figure 4** – Schematic representation of the structure of an anticyclonic (left) and a cyclonic (right) eddy in the southern hemisphere (adapted from Robinson (2010)).

Due to the capability of eddies to alter oceanic surface properties, they have potential to impact the air-sea fluxes and the overlying atmospheric circulation. This comes directly from the fact that as eddies represent an anomaly on the SST, and as shown in Section 1.1.1, the turbulent fluxes depends on SST. We now have access to over two decades of global altimetry data with considerably high spatial and temporal resolution necessary to resolve eddies. To understand the impact of eddies on the surface turbulent fluxes represents another piece in the puzzle of how ocean and atmosphere interact at mesoscales.

## 1.2 Thesis hypothesis and objectives

The present work aims to verify the hypothesis that *mesoscale eddies have a significant impact on the air–sea turbulent heat fluxes. As a result, they should exhibit a well–defined imprint on the latent and sensible heat fluxes and should be capable of explaining a significant portion of the variability in the surface turbulent heat fluxes signal.*

In order to test the hypothesis, the specific objectives of this work are:

- To identify mesoscale eddies in the South Atlantic using a robust detection method and to determine the main eddy characteristics;
- To isolate the anomalies in the latent and sensible heat fluxes associated with the eddies;
- To examine the spatial distribution of the mean eddy anomalies in the South Atlantic from an Eulerian framework, exploring potential differences between eddy polarities;
- To compare the eddy anomalies with the total surface turbulent heat fluxes signal and to estimate the proportion of variance in the total signal explained by the variance of the eddies;
- To assess the spatial pattern of the surface turbulent heat fluxes anomalies within the eddy interiors by analyzing averaged composite maps.

## 2 The South Atlantic Ocean

The overall pattern of the upper (above  $\sim 1000$  m) large-scale circulation in the ocean basins is marked by the presence of great subtropical gyres. Such pattern reflects the strong influence of winds in forcing the upper ocean circulation (PEDLOSKY, 1987). The predominant easterly winds observed near the equator, for example, gradually weakens towards the tropics until they become predominantly westerlies in the subtropics. As predicted by the Ekman's theory, an Ekman transport is induced  $90^\circ$  to the right of the wind direction (northern hemisphere) or to the left (southern hemisphere). Thus, it promotes a convergence of mass near  $30^\circ$  of latitude in both hemispheres, forcing a downward vertical velocity that alters the vorticity balance by the effect of squashing the vortex tube in the water column. To preserve their potential vorticity, the water parcels change their planetary vorticity by moving equatorwards (TALLEY *et al.*, 2011). Sverdrup (1947) was the first to explain the mechanism by which the wind forces this meridional flow, called Sverdrup transport. The equatorward Sverdrup transport integrated across the basin, must be compensated by a strong and narrow flow in the opposite direction. Such flow is established at the western boundary, closing the circulation of the anticyclonic subtropical gyres (STOMMEL, 1948; MUNK, 1950). For more detailed information on the wind-driven circulation, the reader is recommended to refer to Pedlosky (1987) and Gill (1982).

The South Atlantic Subtropical Gyre (SASG) consists of the South Equatorial Current (SEC), Brazil Current (BC), South Atlantic Current (SAC), and Benguela Current system (BCS) (Figure 5). The BCS is the eastern boundary current of the SASG. It begins as a northward flow off the Cape of the Good Hope until approximately  $30^\circ\text{S}$ , when it starts to separate from the African coast by shifting its flow to the northwest (PETERSON; STRAMMA, 1991). Because of the wind patterns in the region, the BCS is characterized by frequent coastal upwelling of cold and nutrient-rich waters that are eventually transported towards the equator and feeds part of the southern branch of the SEC. The SEC is a broad westward flow with three distinct branches separated by the South Equatorial Undercurrent and the South Equatorial Countercurrent (SILVEIRA *et al.*, 1994). The SEC southern branch reaches the Brazilian shelf near  $14^\circ\text{S}$ , where it splits in two new branches, being one stronger than the other. The strongest branch flows northward as the North Brazil Current, while the weaker branch feeds the BC – the western boundary current of the SASG (PETERSON; STRAMMA, 1991). The BC starts its southward flow along the coast of Brazil until approximately  $36^\circ\text{S}$  where its warm saline waters encounter the relatively cold and fresh waters of the Malvinas Current (MC) and starts to flow away from the coast in direction to Africa. The resultant flow from the encounter of the BC with the MC is marked by a strong thermohaline frontal region that characterizes one of the most energetic

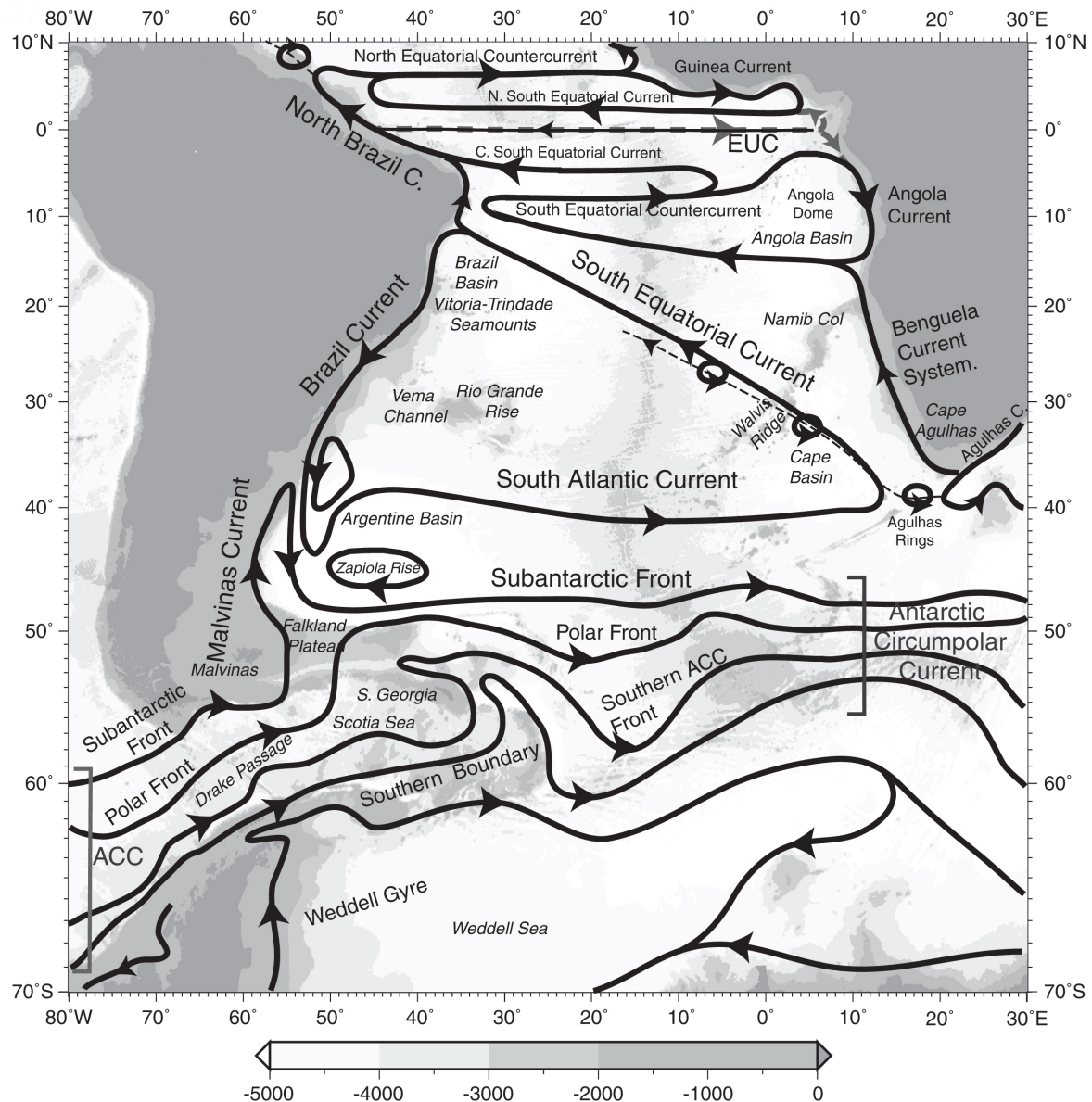


**Figure 5** – Schematic representation of the main surface currents of the South Atlantic Ocean. Black arrows represent the currents and the respective directions of the flow. The brackets near 50°S and 65°S mark the branches of the Antarctic Circumpolar Current. Shades of gray indicate the mean depth of the water column in meters, where white represents the open ocean, and dark-gray, the continents. Figure from Talley *et al.* (2011).

regions of the ocean: the Brazil–Malvinas Confluence (BMC) (PIOLA; MATANO, 2001). After the encounter with the MC, a recirculation cell near 40°S is formed as a branch of the BC turns to the north. The other branch keeps flowing to the south until ~ 45°S, where it turns northeastward to form the SAC (SARACENO *et al.*, 2004). The SAC then, flows eastward in direction to the African continent to close the SASG. Along its path, the SAC feeds the BCS, the Agulhas Current (AC), and the south Indian Current.

## 2.1 Mesoscale Eddies in the South Atlantic

In the South Atlantic Ocean (SA) two regions are characterized by a relatively intense energetic variability associated with mesoscale eddies, namely the Agulhas current retroflexion (AGR) and the Brazil–Malvinas confluence (BMC) (OLSON; EVANS, 1986; GONI *et al.*, 1997; GARZOLI; GARRAFFO, 1989; OLSON *et al.*, 1988). Figure 6 shows the standard deviation of the sea level anomaly (SLA) obtained from satellite altimetry data. Hereinafter, the regions limited by the black contours will be referred as the areas of influence of the BMC (area 1 in Figure 6) and AGR (area 2 in Figure 6), where the variability of the SLA is notably higher than in the rest of the basin. Thus, to encompass both quiescent and energetic areas, the study region of this work will span between 10°S and 50°S, and 60°W and 30°E. It is important to note that when compared with other oceanic

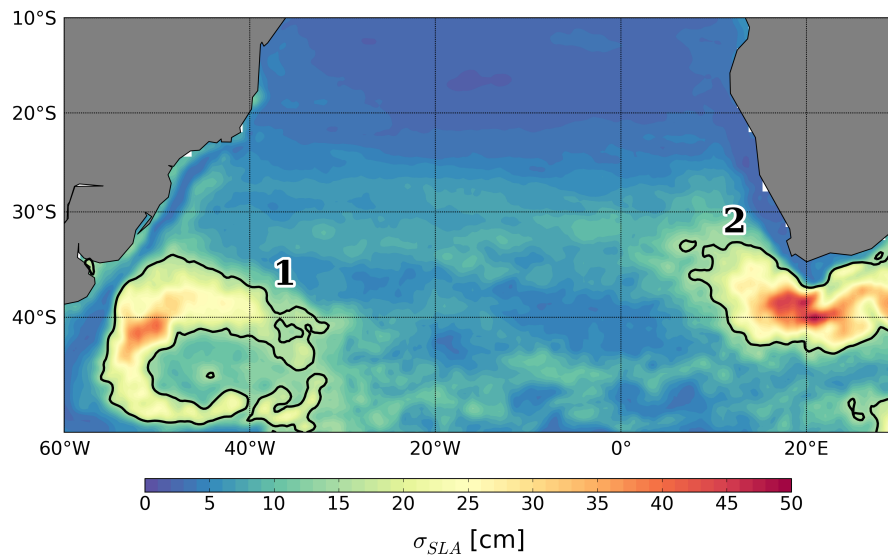


**Figure 6** – Standard deviation ( $\sigma$ , in cm) of the sea level anomaly (SLA) over the South Atlantic between 1999 and 2009; Black contours correspond to  $\sigma = 15$  cm and delimit the Brazil–Malvinas confluence region (BMC, contour 1) and the Agulhas Current Retroflexion region (AGR, contour 2).

basins, the SA remains underexplored and scarcely sampled (GARZOLI; MATANO, 2011; GARZOLI *et al.*, 2013; CAMPOS *et al.*, 1996). The lack of *in situ* measurements in the region makes it harder to validate numerical climate models and calibrate instruments, which in turn have consequences for scientific research and publications in this region. The definition of the study area of this work is an attempt to contribute to a better understanding of the processes that drive the dynamics of the SA. To better contextualize, a more detailed description of the dynamics of the sub–areas of intense mesoscale activity in the SA is presented next.

### 2.1.1 The Brazil–Malvinas Confluence

The BMC is characterized for being one of the regions with the highest mesoscale variability of all the world oceans (PIOLA; MATANO, 2001; CHELTON *et al.*, 1990). The confluence is marked by the encounter of waters from subtropical origin, flowing southward as the BC, with the equatorward flow of the MC, carrying waters from subpolar origin. This promotes strong horizontal thermal gradients that can reach up to 1°C/250 m (GARZOLI; GARRAFFO, 1989). Gordon (1989) have analyzed hydrographic data from the *Thomas Washington Marathon 7* cruise, sampled during October 1984 in the BMC region. The author described the region as being strongly baroclinic and composed by contrasting water masses. He also underlined that the latitude of separation of the BC from the coast is a function of depth. Such intense vertical and horizontal shearing, trigger instabilities that are manifested as meanders and eddies. Indeed, the author have observed one large cold–core cyclonic eddy, with a radius of 135 km, that was formed from the wave–like meandering of the BC as it flows seaward. In addition, two smaller warm–core anticyclones, with radius of 70 km and 55 km, were generated from the poleward end of the western meander of the BC. Gordon (1989) conclude that, as the eddies from the BMC propagate southeastward, they gradually dissipate and exchange heat and salt with their surroundings. Therefore, these eddies could act as sources of heat and salt for the Antarctic zone, contributing to water mass modification.

Despite early hydrographic studies from the 1920–1940 decades <sup>1</sup> have described the behavior of the BMC, it was only with the advent of satellite oceanography that it became possible to better assess the complexity of mesoscale dynamics in the region (OLSON *et al.*, 1988; LEGECKIS; GORDON, 1982). Legeckis and Gordon (1982) used satellite infrared observations from the *Very High Resolution Radiometer* (VHRR) to monitor the BC and MC in the region of the BMC. The authors found that the southernmost position of the BC fluctuates between 38°S and 46°S, with a periodicity of about two months. In addition, between September 1975 and April 1976, they observed 20 warm–core anticyclonic eddies with diameters between 70 km and 350 km and with southward propagation. Even though the exact mechanism of eddy formation was not fully explained by the authors, they suggest that it might be related with instabilities of growing wave–like meanders or with the pinching off from the southern tip of the BC. Olson *et al.* (1988) combined satellite and drifter data to study the separation of the BC and MC from the western boundary. The authors presented what became a classical image to illustrate the dynamics of the BMC region (Figure 7), where temperature contrast between the two currents and the detachment of a large warm–core eddy are evident.

As an extension of the work of Olson *et al.* (1988), Garzoli and Garraffo (1989)

<sup>1</sup> A very detailed review of the research conducted by George Deacon during the *Discovery* Investigations in 1927, for example, can be found on Mills (2004).

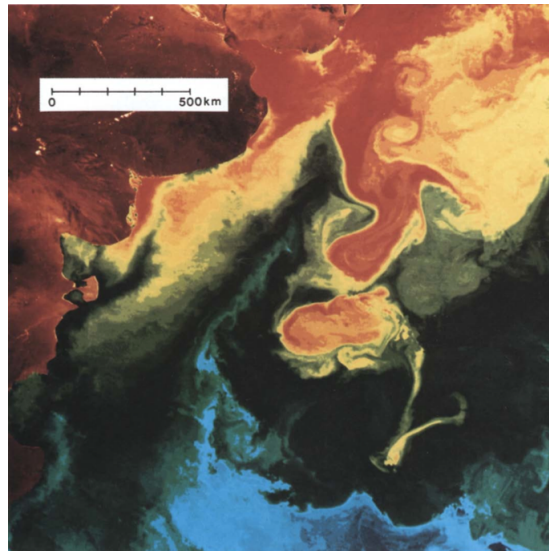


**Figure 7** – Mesoscale activity near the BMC region. The encounter of the relatively warm waters of the BC (reddish) with the relatively cold waters of the MC (greenish) creates instabilities that feature growing meanders which eventually close off and separate from the main current forming eddies. Figure from Olson *et al.* (1988)

used an array of inverted echo sounders (IES) to estimate dynamic height and geostrophic velocities in the region of the BMC from June 1985 to March 1986. The authors detected 3 cold-core cyclonic eddies with approximately  $6.5 \times 10^{15}$  J of available potential energy each. Furthermore, they estimated that the mean position of the BMC have a east-west oscillation with periods close to 12 months, and a north-south oscillation with periods of 1–2 months. By similar means, but using an array of IES with higher spatial resolution, Garzoli (1993) verified that the same high variability in the BMC region, that have been inferred in previous studies using radiometer data, was also present in dynamic height field. The author have also detected mesoscale eddies of both polarities (cyclonic and anticyclonic) with diameters between 100 km and 150 km, which corresponds to 2–3 times the local Rossby radius of deformation. These eddies were observed not only between the BC and MC, but also propagating superimposed to the mean flow. One of the pioneering studies in the BMC region using satellite altimetry data was conducted by Goni *et al.* (1996). The authors combined data from *Advanced Very High Resolution Radiometer* (AVHRR) with Geosat altimeter and IES to expand the analysis of Garzoli (1993) and assess more characteristics of each eddy. One of the detected anticyclones had an elliptical shape, with major and minor axes of 400 km and 60 km, respectively. The surface temperature at the eddy core was of 19.3 °C in comparison to 14.0 °C and 15.3 °C at its surroundings. The feature lasted for about 15 days before being reabsorbed by the BC.

A robust statistics of warm-core mesoscale eddies shed by the BC into the BMC region was presented by Lentini *et al.* (2002). The authors identified and followed a total of 43 anticyclonic eddies using 6 years of SST data from AVHRR. In agreement with

previous studies (GONI *et al.*, 1996; GARZOLI, 1993; LEGECKIS; GORDON, 1982), most of the eddies had an elliptical shape with major and minor radius of  $126 \pm 50$  km and  $65 \pm 22$  km, respectively. On average  $\sim 7$  anticyclones were observed each year, with a mean lifetime of approximately 35 days and translational velocity of  $\sim 7$ – $27$  km/day. The general fate of the eddies was to propagate southeastward, southwestward, or being reabsorbed by their parent current.

Besides modifying physical properties of the ocean, mesoscale eddies also have a signature on biological tracers. Garcia *et al.* (2004) used ocean color data from *Sea-viewing Wide Field-of-view Sensor* (SeaWiFS) to explore the spatial and temporal variability of chlorophyll-a concentration in the BMC region during 5 years. By combining SeaWiFS data with altimetry and AVHRR, the authors were able to identify the generation and evolution of cold-core mesoscale eddies shed by the BC retroflection. At the formation time the identified eddies had a clear signature on the chlorophyll concentration, that gradually diminished as they propagate northward. This decay in the chlorophyll concentration at the eddy cores, was also observed on SST and SLA signals as a consequence of the mixing of the eddies with warmer and low chlorophyll concentration waters. By following the chlorophyll maximum in the eddy centers, the authors estimated a propagation velocity of  $\sim 12$  km/day, which was in accordance with the results of Lentini *et al.* (2002). Moreover, Souza *et al.* (2006) combined satellite SST images from the *Moderate-Resolution Imaging Spectroradiometer* (MODIS) with ship measurements to study a warm-core eddy near  $44^\circ\text{S}$  and  $56^\circ\text{W}$  in November 2002. The eddy shed by the BC propagated for 64 days before being reabsorbed by the mean flow. The eddy had an approximated diameter of 150 km and amplitude of 24 cm. The vertical signature of the eddy reached depths of 150 m, with corresponding heat content of  $4.24 \times 10^{18}$  J and salt anomaly of  $1.37 \times 10^{12}$  kg.

To summarize, the dynamics of the BMC is dominated by mesoscale eddies. The encounter of the cold, strong barotropic flow of subpolar waters of the MC with the warm baroclinic BC, promotes intense shear instabilities that features meanders and mesoscale cold and warm eddies. Although eddies formed in the region of the BMC have relatively short lifetime and do not propagate very farther, they play a crucial role for physical and biogeochemical local budgets.

### 2.1.2 The Agulhas Current Retroflection

The first observations of high variability in the region of the AGR are reported from the beginning of the XIX century, when seafares frequently noticed currents presenting patterns very distinct from the usual (ROBINSON, 1983). Much latter, Duncan (1968) observed an anticyclonic eddy during a cruise to the region of the AGR. The eddy had an amplitude of 60 cm and its anomaly on the temperature field reached depths of the order of  $\sim 1$  km. The author does not present an explanation for the eddy formation,

although it is suggested that such eddy could be caused by baroclinic instabilities of the AC, promoted by its interactions with the Antarctic Circumpolar Current or by topographic effects. Nowadays, the large, warm-core anticyclonic eddies formed in the region of the AGR are known as the Agulhas rings.

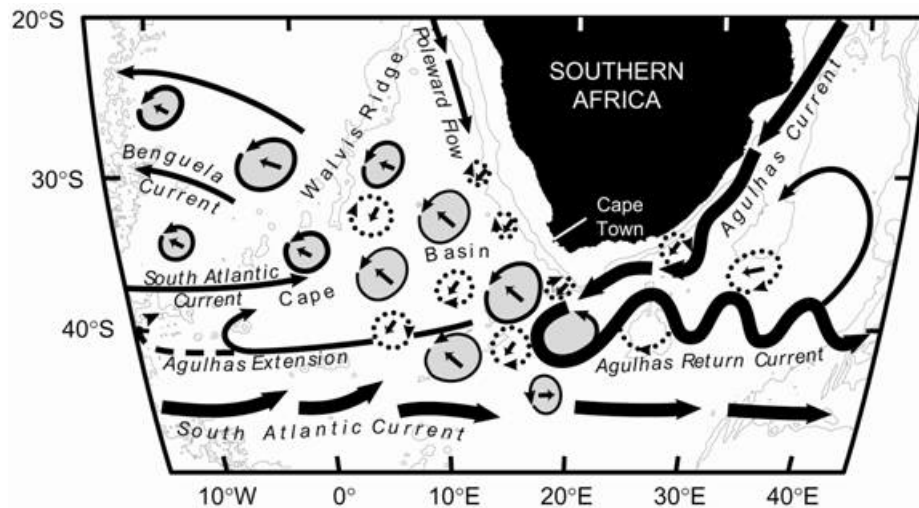


**Figure 8** – Schematic representation of the dynamics near the AGR region. When the AC reaches the tip of Africa, it turns to the west and then retroflects back shedding anticyclonic Agulhas rings. The major currents are represented by thick black lines, the Agulhas rings are the solid anticlockwise arrows and some cyclonic eddies are represented by dashed clockwise arrows. Figure from Talley *et al.* (2011).

In contrast to BMC eddies and most of other mesoscale eddies in the ocean, Agulhas rings are not formed by the pinch off of growing meanders (PICHEVIN *et al.*, 1999). When the southward flowing AC, reaches the tip of the African continent, it turns to the west in direction to the SA. Then, it retroflects back to the east, around 20–15°E, to form the Agulhas Return Current (OLSON; EVANS, 1986). As the AC retroflects, it sheds anticyclonic rings into the SA (Figure 8) that can drift with the BCS and flow northwestward advecting warmer and saltier waters from the Indian ocean along their trajectories (GONI *et al.*, 1997). Agulhas rings are coherent and longlived structures with lifetime of years. Typical Agulhas rings have diameters between 200 and 280 km, and they can trap and transport waters in the ring core to depths of 500–1000 m (GONI *et al.*, 1997; OLSON; EVANS, 1986; GARZOLI *et al.*, 1999). Despite on average 6 to 9 Agulhas rings are shed per year, the shedding is intermittent and strongly variable (BYRNE *et al.*, 1995; SEBILLE *et al.*, 2010; BOEBEL *et al.*, 2003). Goni *et al.* (1997), for example, have used data from the satellite altimeters TOPEX/Posidon to study the dynamics of Agulhas rings between 1992 and 1995. The authors have reported periods as large as 7 months without any ring shedding. Similar periods of no ring shedding were also found by Schonten *et al.* (2000), using data from the same instruments.

Bottom topography plays a major role on the propagation of the Agulhas rings.

Both studies of Goni *et al.* (1997) and Schonten *et al.* (2000) observed that a considerable fraction of the Agulhas rings never propagated farther than the Walvis Ridge<sup>2</sup>. In addition, Schonten *et al.* (2000) have also mentioned bottom topography as a key to ring dissipation. According to the authors, because of the interaction with bottom topography, Agulhas rings can split into two or more weaker rings that eventually lose their anomalous signature to the adjacent waters.

Several studies to quantify the transport from the Indian to the Atlantic ocean by the Agulhas rings have been done during the last decades. Using hydrographic data, Gordon and Haxby (1990) have estimated such transport to be between 5 and 15 Sv (1 Sv =  $10^6 \text{ m}^3 \text{ s}^{-1}$ ). While Byrne *et al.* (1995) have tracked six Agulhas rings from satellite altimetry data and estimated a transport of at least 5 Sv. Besides transporting mass, Agulhas rings can also impact the energy, salt, and heat fluxes. Olson and Evans (1986) have calculated that the averaged energy flux of a single Agulhas ring shed into the SA is equivalent to 7% of the annual wind energy input. Ballegooyen *et al.* (1994) combined altimetry and hydrographic data to estimate the annual heat and salt fluxes of the Agulhas rings into the SA to be of 0.045 PW and  $78 \times 10^{12} \text{ kg}$ , respectively. The influence of the Agulhas rings is far from being local. Their lifetimes can be long enough to allow for them to cross the entire SA basin and reach 30–40°W (BYRNE *et al.*, 1995; GONI *et al.*, 1997). Indeed, Byrne *et al.* (1995) suggests that the Agulhas rings could have impact on the energy and vorticity balance of the BC and could affect the mesoscale activity in the BMC region. More recent research on the interoceanic exchange between the Indian and Atlantic oceans have highlighted the potential influences of the Agulhas rings on the decadal variability of the Atlantic meridional overturning circulation (AMOC) (BIASTOCH *et al.*, 2008; BEAL *et al.*, 2011)

Besides anticyclonic Agulhas rings, cyclonic eddies are also frequently formed in the AGR region. During the years of 1992 and 1993, the Benguela Sources and Transports (BEST) hydrographic program detected 4 cyclonic eddies in the AGR region (RAE *et al.*, 1996). Stramma and Peterson (1990) have also found a cyclone near 39°S, 11°E. However, because cyclonic eddies are smaller and have a shorter lifetime, they were for long subsampled in comparison to the Agulhas rings. More recently, Boebel *et al.* (2003) combined *in situ* Lagrangian data with satellite sea surface height data to extensively study the role of cyclonic eddies on the interocean exchange. From 1997 to 1999, the authors detected on average 20 cyclones per year in the region of the AGR. They suggest that the generation of these cyclonic eddies might have its origin on the cyclonic pulses of the AC (Natal pulses) or on the interaction of Agulhas rings with the shelf. The cyclonic eddies would then strongly interact with Agulhas rings and while losing strength they would mix

<sup>2</sup> The Wavis Ridge is an oceanic ridge originated from hotspot volcanism and located off the coast of Africa between, Cape basin and Angola basin

their water with the BCS.

In summary, the AGR is a primary source of mesoscale eddies in the SA. Agulhas rings are one of the most energetic eddies in the world's ocean and they play an important role on the interocean exchange between the Indian and Atlantic oceans. Furthermore, cyclonic eddies are also formed in the region of the AGR. Although, owing their dynamical characteristics, they impact more locally in comparison to the Agulhas rings.

## 3 Data and Methods

Ten years of SLA (1999–2009) from satellite altimetry data were used to identify mesoscale eddies in this study. The information on the position and contours of eddies were combined with remotely sensed surface turbulent heat fluxes to investigate the impact of ocean mesoscale eddies on the latent and sensible heat fluxes in the South Atlantic. It is presented next the detailed description of both datasets and the methodology applied to process and analyze the data.

### 3.1 Altimetry data and eddy identification

#### 3.1.1 Sea level anomaly data

The satellite altimeter is an active instrument that estimates the distance between itself and a given target by emitting a radar pulse. In the case of the ocean, part of the energy of such pulse is reflected at the sea surface and detected by the satellite antenna after a time interval  $\Delta t$ . Knowing that the pulse travels at the speed of light ( $c$ ), the distance ( $d$ ) between the altimeter and sea surface can be obtained by  $d = c\Delta t$ . Thus, the sea surface height (SSH) is given by the difference between the height of the satellite from the reference ellipsoid and the distance  $d$  measured by the altimeter. Since 1985, several satellites (GEOSAT, TOPEX/Poseidon, ERS1-2, GFO, Jason1–2, etc.) equipped with altimeters have been launched what enables to repetitively observe the SSH with relatively high spatio–temporal resolution.

At the beginning of the 1990 decade the European Space Agency (ESA), launched the first satellite of the *European Remote Sensing* series, the ERS–1, equipped with a radar altimeter capable of measuring SSH with a nominal precision of  $\sim 5$  cm, and a repetition period of  $\sim 35$  days. In August 1992, it was the time for the TOPEX/Poseidon (T/P) satellite to go to space, as part of a joint mission between the French space agency *Centre National d'Études Spatiales* (CNES) and the North American space agency *National Aeronautics and Space Administration* (NASA). T/P had a repetition period of  $\sim 10$  days, carrying onboard a high resolution positioning system (Doris), and two altimeters (one operating at a time) with a nominal precision of 2 cm. The launching of T/P represented the beginning of a new era for the study of mesoscale in the ocean. Despite the satellite itself was designed to have accuracy only to investigate large–scale ocean circulation, its orbit was complemented by the orbit of ERS–1, allowing to create a merged dataset with high enough resolution to resolve mesoscale variability. Since then, it has always been at least two satellites operating at the same time in complementary orbits (Figure

9). In April 1995 it was launched ERS-2, the follow-on from ERS-1, with exactly the same 35 days repetition period. ERS-2 was moved to a lower orbit and deactivated in 2011 due to technical problems. Envisat, the follow-on from the ERS satellite's, was launched in 2002 and operated until April 2012, completing 10 years of measurements. The successor of T/P was the Jason-1 satellite, launched on December 2001. Because of the surprisingly success of the T/P mission, that overcame its expected lifespan by almost 8 years, Jason-1 operated for the first six months in a tandem mission with a shift of one day from T/P. In September 2002, T/P was transferred to a new orbit halfway from its old tracks. Thus, from 2002 to 2005, Jason-1 and T/P operated in a high resolution mission, where the original distance between two satellite tracks was reduced to half. This satellite constellation and the merging of the acquired data allow to reveal the presence of energetic mesoscale eddies that have a clear signal on sea level anomalies (FU *et al.*, 2010). Thus, based on equation 1.7, the merged satellite product can be used to directly infer the dynamics and characteristics of mesoscale eddies from the geostrophic velocity fields. Today we have access to over two decades of satellite altimetry data, with synoptically and all weather observations of the global ocean. Altimetry has been giving a unique contribution to the understanding of many oceanographic phenomena in a broad range of temporal and spatial scales, namely El Niño/La Niña, Rossby waves, sea level rise, and mesoscale eddies, representing therefore a powerful tool for the oceanographic community (FU; TRAON, 2006; MORROW; TRAON, 2006).

In this work we used ten years (1999–2009) of SLA data from the gridded multimission product processed by the *Segment Sol multimissions d'ALTimétrie, d'Orbitographie et de localisation précise* (Ssalto) and the *Data Unification and Altimeter Combination System* (Duacs), distributed by the French *Archiving, Validation and Interpretation of Satellite Ocean data* (AVISO).<sup>1</sup> This merged dataset corresponds to the AVISO reference series, which merges data from only two simultaneous satellite missions, resulting in a spatially homogeneous dataset. The SLA is computed relatively to a 7-year mean (1993–1999), projected on a  $1/3^\circ$  Mercator grid, and objectively interpolated to a uniform  $1/4^\circ$  grid at 7-day intervals, consisting of the best spatial and temporal resolution available to globally monitor mesoscale dynamics in the ocean.<sup>2</sup> Before the SLA product being delivered, Ssalto/Duacs system applies corrections such as atmospheric and ionospheric effects, ocean tide, solid earth tide, sea state bias, among others (see Dibarboure *et al.* (2008)). The final SLA product used in the present study have spatial resolution of  $1/4^\circ \times 1/4^\circ$ , temporal resolution of 7 days and nominal precision of 2 cm (TRAON *et al.*, 2003; DUCET *et al.*, 2000).

<sup>1</sup> <<http://www.aviso.oceanobs.com/duacs/>>

<sup>2</sup> There is currently a new release of SLA data from AVISO interpolated to daily maps.

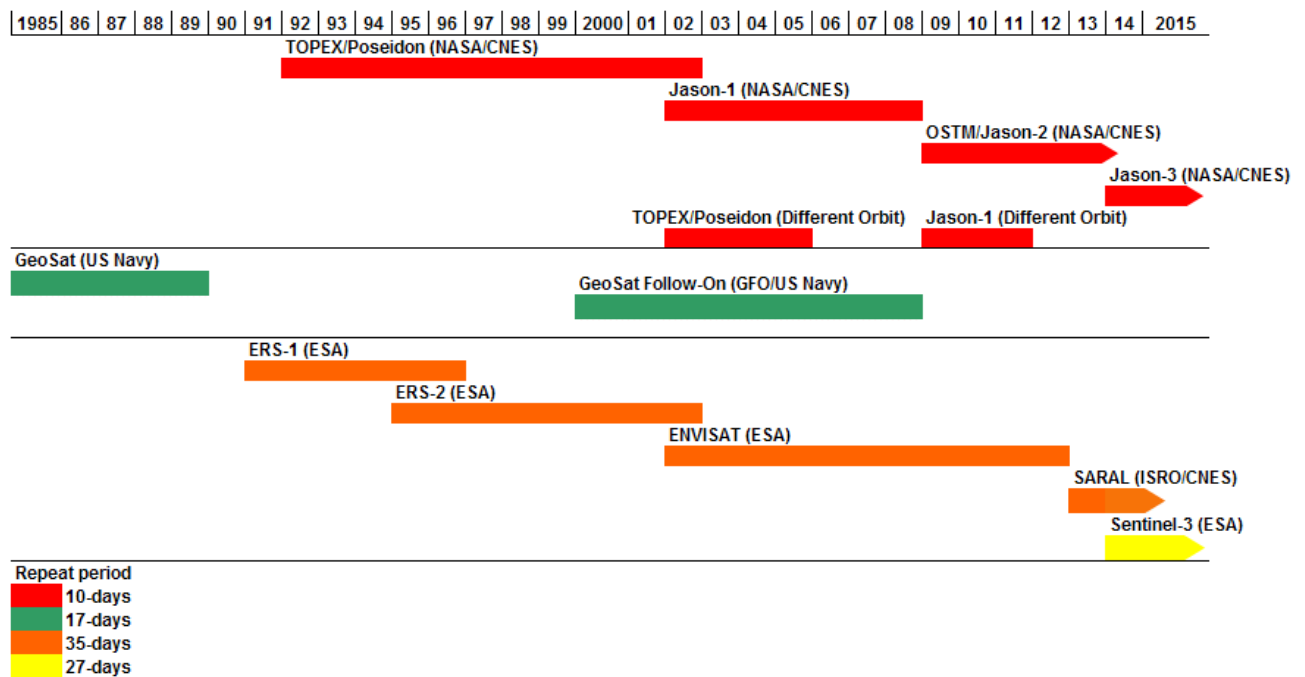


**Figure 9** – Timeline of all satellite altimetry missions since 1985. Colors indicate the repetition period of each satellite, which is the time it takes for the satellite to sample the same point again. Since 1992, it has been at least two altimeters operating at the same time. Figure obtained from: <<http://www.pecad.fas.usda.gov/>>

### 3.1.2 The Winding-Angle Method

Several methods to identify mesoscale eddies from SLA maps have been developed and broadly used in the last decades. These methods rely either on physical or geometrical properties of the flow field. For instance, Isern-Fontanet *et al.* (2003), Morrow *et al.* (2004) and Chelton *et al.* (2007), used a method based on the Okubo-Weiss parameter (OKUBO, 1970; WEISS, 1991), based on the comparison of the vorticity with the deformation of the flow. In this case, eddies are associated with regions where vorticity dominates over deformation. On the other hand, Nencioli *et al.* (2010), Chaigneau *et al.* (2008), and Chaigneau *et al.* (2009), have identified mesoscale eddies based on geometrical properties of the velocity or the SLA field. Although those distinct eddy identification algorithms are relatively well suited to study mesoscale dynamics, most of them fail at some point and have their own limitations (CHAIGNEAU *et al.*, 2008; SOUZA *et al.*, 2011b; KURCZYN *et al.*, 2012). In the last years, there has been a consensus among oceanographers (CHELTON *et al.*, 2011b) to identify eddies using either the Okubo-Weiss (OW) or the winding-angle (WA) method. The OW method was widely used to identify mesoscale-scale eddies in earlier works (ISERN-FONTANET *et al.*, 2003; CHELTON *et al.*, 2007; CHAIGNEAU *et al.*, 2008), however, it has some major problems associated with error maximization and

threshold dependency. Some of these weaknesses were pointed out by (CHELTON *et al.*, 2011b) and are also discussed in detail in the Appendix A. Thus, we have chosen to use in the present work a threshold-free geometric method based on the same concept of the WA method, originally proposed by Chaigneau *et al.* (2008), with a slightly modified version being presented more recently by Chaigneau *et al.* (2009).

The WA method is motivated by the definition given by Robinson (1983) that eddies exist in regions where streamlines have an approximately circular shape. As in the geostrophic approximation (Equation 1.7) streamlines are parallel to contours of SLA, we can by equivalent means associate eddies with closed contours of SLA. To apply the eddy identification in the study area we first downloaded the SLA maps from AVISO database from October 1992 to November 2012. To ensure that the eddy detection algorithm performs in the best possible way, which is to include all the eddies in the study region, we increased our geographical limits by  $3^\circ$  at each border, obtaining a grid spanning from  $7^\circ\text{S}$  to  $53^\circ\text{S}$ , and from  $63^\circ\text{W}$  and  $33^\circ\text{E}$ . In addition, we considered just the part of the AVISO timeseries overlapping the time range of the other dataset used in this work (1999–2009). The data pre-processing consists of calculating and/or extracting from the SLA maps the parameters described in Table 1.

Parameter	Description	units
$(u_g, v_g)$	Zonal and meridional components of the geostrophic velocity	$[\text{m s}^{-1}]$
EKE	Eddy Kinetic Energy	$[\text{m}^2 \text{s}^{-2}]$
$S_n, S_s$	Normal and shear components of strain	$[\text{s}^{-1}]$
$\zeta$	Vorticity	$[\text{s}^{-1}]$
(lat, lon)	Latitude and longitude	[degrees]
(dd,mm,yy)	Day, month and year of the data	

**Table 1** – List and description of the parameters obtained from the AVISO SLA maps by the pre-processing routine of the Chaigneau *et al.* (2009) eddy identification algorithm.

After being pre-processed, the SLA maps are ready to be loaded into the eddy detection algorithm itself. First, the WA identification algorithm searches for local maxima and minima of SLA, that correspond to the center of anticyclonic and cyclonic eddies, respectively. Then, for each detected eddy center, the algorithm looks for closed SLA contours such that the outermost closed contour embedding only the considered center is defined as the eddy edge. To be more specific, the WA method follows the sequence of steps undermentioned:

- (i) On each SLA map, it searches for possible eddy centers corresponding to local maxima (anticyclones) and minima (cyclones) of SLA.
- (ii) Starting from each possible center, look for closed SLA contours with a decrement (anticyclones) or an increment (cyclones) of  $10^{-3}$  m.

- (iii) The eddy edge is determined by the outermost closed SLA contour enclosing just the considered center.

From the output of the WA identification algorithm, we obtain a complete database with all eddy parameters, as listed in Table 2. The equivalent radius ( $R$ ) is calculated as the radius of a hypothetical circular vortex having the same area ( $S$ ):

$$R = \sqrt{\frac{S}{\pi}}. \quad (3.1)$$

The eddy amplitude ( $A$ ) is obtained from the difference between the SLA at the eddy center ( $X_c, Y_c$ ) and the SLA at the eddy edge ( $X_{con}, Y_{con}$ ).

Parameter	Description	units
$(N_{Anti}, N_{Cyclo})$	Number of anticyclonic and cyclonic eddies	
Radius	Eddy equivalent radius	[km]
Amplitude	Eddy Amplitude	[cm]
Area	Area delimited by the eddy edge	[km <sup>2</sup> ]
$(X_c, Y_c)$	Coordinates of the eddy center	[degrees]
$(X_{con}, Y_{con})$	Coordinates of the eddy edge	[degrees]
EKE	Mean EKE inside the eddy	[m <sup>2</sup> s <sup>-2</sup> ]
$\zeta$	Mean vorticity inside the eddy	[s <sup>-1</sup> ]

**Table 2** – List and description of the parameters obtained by the eddy identification algorithm. For each eddy, it is possible to assess its respective radius, amplitude and contour, which are the most important variables for this work.

An example of contours and centers of cyclonic and anticyclonic eddies detected from AVISO SLA maps by the WA method is shown in Figure 10.

## 3.2 Surface turbulent heat fluxes data and anomalies

Owing the importance of the interactions between ocean and atmosphere, to estimate turbulent air–sea fluxes with accuracy represents a major concern for marine and atmospheric sciences. Most of the measurements of such fluxes have been obtained from numerical weather models, remote sensing, and *in situ* data, which contributes to relatively heterogeneous dataset (BENTAMY *et al.*, 2013). During the last decade great efforts have been made to develop new algorithms and methods to better estimate long time series of turbulent fluxes with uniform global coverage, such as the OAflux project (YU; WELLER, 2007) and the J-OFURO project (KUBOTA *et al.*, 2002). In this work we used the most recent turbulent heat fluxes dataset produced by the *Institut Français de Recherche pour l'Exploitation de la Mer* (IFREMER).

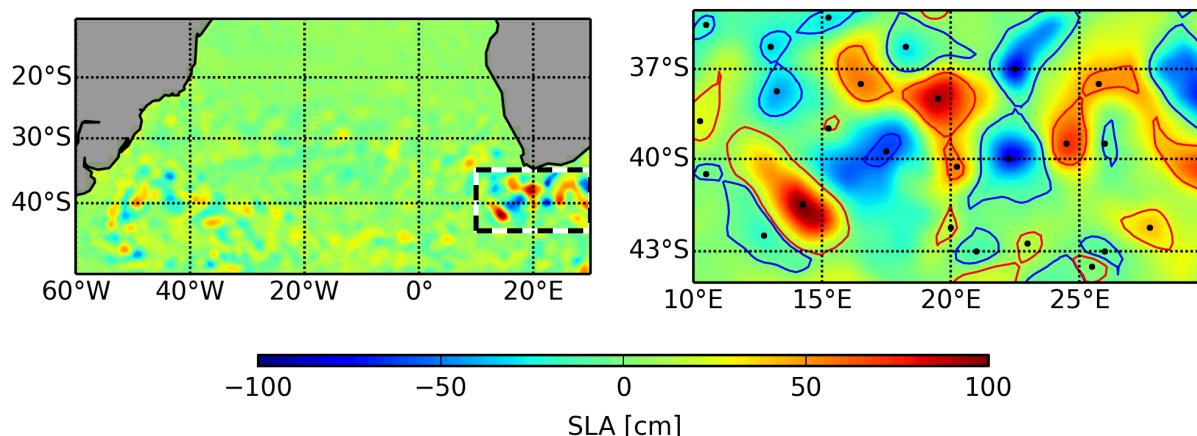


**Figure 10** – Illustration of the eddy identification method of Chaigneau *et al.* (2009). The left panel is a snapshot of the SLA from AVISO corresponding to May 13, 2009. A zoom of the area limited by the dashed line is shown in the right panel, where the eddy centers are marked with black dots, and contours of cyclonic and anticyclonic eddies are drawn in blue and red, respectively.

### 3.2.1 Surface turbulent heat fluxes data

The latest release (V3) of the surface turbulent heat fluxes product by IFREMER was used in this work, to analyze the heat fluxes anomalies associated with eddies. In this product, the LHF and SHF are estimated using the bulk algorithms of Fairall *et al.* (2003) with input parameters obtained from remote sensing (BENTAMY, 2013). The remote sensed parameters necessary to compute the surface turbulent heat fluxes according to equations 1.4 and 1.3 are: surface wind speed at 10 m ( $u$ ), sea surface temperature ( $T_s$ ), air temperature at 10 m ( $T_a$ ), and air specific humidity at 10 m ( $q_a$ ).

The surface wind speed used by IFREMER was obtained from the SeaWinds scatterometer on board of the QuikSCAT satellite, that provided daily global and all weather wind speed measurements, for the period from 1999 to 2009, with spatial resolution of  $1/4^\circ$ . Scatterometers are active instruments that estimate the wind speed and direction by emitting a radar pulse and measuring the backscatter signal power. The backscatter is associated with the scattering from wind-generated surface capillary-gravity waves, that generally have wavelengths with the same order of magnitude as the radar microwaves. Thus, the wind affects the size of capillary-gravity waves that in turn affect the backscatter detected by the scatterometer antenna. The wind speed, can therefore be inferred by the Bragg scattering of the radar pulse at the sea surface, while the wind direction can be estimated by varying the angle of incidence of each pulse. The wind speed from QuikSCAT Version 3 is distributed by NASA's *Jet Propulsion Laboratory/Physical Oceanographic Distributed Active Archive Center* (JPL/PODAAC). The precision of the wind speed is 2 m/s for weak to moderate winds (3–20 m/s), and it is corrected for the equivalent neutral

wind at 10 m height ( $u$ ) (LIU, 2002).

In contrast to altimeters and scatterometers, microwave radiometers are passive instruments that measure the electromagnetic radiation emitted by the Earth's surface. Radiometers have great importance in climate sciences since they are capable of measuring several oceanic and atmospheric properties, namely SST, cloud coverage, rain rate, column integrated water vapour content, and air temperature, among others. The SST used by IFREMER was measured by the *Advanced Microwave Scanning Radiometer* (AMSR) and the *Advanced Very High Resolution Radiometer* (AVHRR) and are available as a single optimum interpolation (OI-SST) product with spatial resolution of  $1/4^\circ$ , provided by *National Oceanic and Atmospheric Administration* (NOAA) of the *National Climatic Data Center* (NCDC) (REYNOLDS *et al.*, 2007). In comparison to the previous IFREMER product (V2) (BENTAMY *et al.*, 2008), the new release of surface turbulent heat fluxes presents a more robust way of estimating the specific air humidity, based on the brightness temperature ( $T_b$ ). The brightness temperature is the temperature a black body would be in order to emit the radiance measured by the radiometer's sensor. The brightness temperature used by IFREMER were obtained from the *Special Sensor Microwave/Imager* SSM/I radiometer on board of the *Defense Meteorological Satellite Program* (DMSP) satellites (F11, F13, F14 and F15), that measures  $T_b$  in several channel operating at distinct frequencies. Such measurements are available online from the *Global Hydrology Resource Center* (GHRC) website (<<http://ghrc.msfc.nasa.gov/>>.)

To retrieve  $q_a$  from satellite measurements, the new IFREMER release uses an empirical model that relates  $q_a$  to  $T_b$  from SSM/I. In addition to  $T_b$ , Bentamy *et al.* (2013) found that dependencies on  $T_s$  and air-sea temperature difference ( $DT$ ) were also important to better estimate  $q_a$ . Thus,  $q_a$  is empirically obtained from the combination of these three parameters:

$$q_a = f_1(T_{b,19V}) + f_2(T_{b,19H}) + f_3(T_{b,22V}) + f_4(T_{b,37V}) + g(T_s) + h(DT), \quad (3.2)$$

where 19V, 19H, 22V and 37V are the radiometer channels, and  $f_{1-4}$ ,  $h$ , and  $g$  are empirical functions. For calibration purpose, the empirical  $q_a$  was compared to  $q_a$  from the latest version of the National Oceanography Centre air-sea 2.0 interaction gridded data set (NOCS2.0). In addition to remote sensed input parameters, the IFREMER surface turbulent heat fluxes product uses the air temperature  $T_a$  estimated from re-analyses (ERA-Interim) by the European Centre for Medium Weather Forecasts (ECMWF). After validation using *in situ* data from buoys, global daily SHF and LHF are provided for the period from October 1999 to November 2009 (the QuikSCAT period), with spatial resolution of  $1/4^\circ$  (BENTAMY *et al.*, 2013). The gridded surface turbulent heat fluxes product (V3) is accessible online on <<ftp://ftp.ifremer.fr/ifremer/cersat/products/gridded/flux-merged/v3/>>.

### 3.2.2 Definition of the surface turbulent heat fluxes anomalies

In the following sections the methodology applied to obtain the surface turbulent heat fluxes anomalies associated with mesoscale eddies are described.

#### 3.2.2.1 Moving Average Filters

Air–sea fluxes are observed on a broad range of temporal and spatial scales, comprising from synoptic to seasonal and interannual scale (GULEV; BELYAEV, 2012). In order to isolate the mesoscale band of the spectrum, both components of the surface turbulent heat flux were firstly time filtered with a band–pass Hann window to preserve only periods ( $T$ ) between 7 and 90 days, which comprehends the typical time scales of mesoscale ocean eddies.

Filtering is an essential part of data analysis. In physical oceanography, they allow to isolate the signal variability within a desired frequency band, which makes possible to study multiple phenomena independently (EMERY; THOMSON, 2001). The main idea behind digital filters is to preserve the signal in the frequency band of interest and to attenuate the signal in all other frequencies. Among low–pass digital filters, the moving average consists of one of the simplest and most powerful tool. In a simplified way, the mechanism of a moving average filter resides in averaging a given number of points ( $M$ ) in the input signal ( $x$ ) to originate the output ( $y$ ) (SMITH, 1997). Thus, depending on the number of points you consider, it is possible to average out the high–frequency variability. Mathematically, such operation can be written as:

$$y[i] = \frac{1}{M} \sum_{j=-(M-1)/2}^{(M-1)/2} x[i + j], \quad (3.3)$$

where  $i$  is the point for which you are computing the moving average and  $j$  is the  $j$ -th neighbor of such point. In the case of the moving average of Equation 3.3, all points have the same weight, and therefore contribute equally to the average. However, moving averages can be weighted by a specific function ( $W$ ), that gives more or less importance to a particular neighboring point, depending on its distance from the center. All filters applied in this work were weighted by a Hann window, which is defined by Equation 3.4 and illustrated in Figure 11.

$$\begin{cases} W_{Hann} = \frac{1}{2} \left[ 1 + \cos \left( 2\pi \frac{r}{l} \right) \right], & |r| \leq \frac{l}{2} \\ W_{Hann} = 0, & |r| > \frac{l}{2}, \end{cases} \quad (3.4)$$

where  $r$  is the distance from each point to the center, and  $l$  is the window length. The Hann window is a general purpose window broadly used in data analysis, mostly because

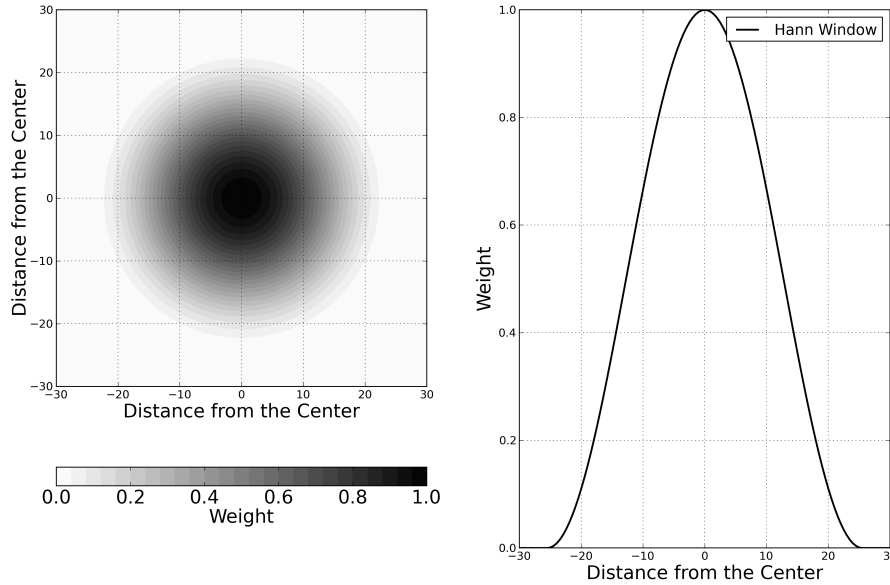


**Figure 11** – Graphical example of a Hann window given by Equation 3.4, with  $l = 60$ . The left panel represents a two-dimensional window, while the right panel represents the same function in only one dimension. In both cases the window weight has its maximum value at the center ( $r = 0$ ), and decays to zero at  $|r| = l$ .

of its capability of minimizing the effects of energy leakage in the filtering process. It gives a higher weight to the points near the center, that decays with the absolute distance  $|r|$ . The output from a moving average filter weighted by the Hann function is then obtained by the convolution of  $W_{Hann}$  with the data. We applied a one-dimensional moving average Hann window (CASTELÃO *et al.*, 2013) to band-pass filter the LHF and SHF, preserving only temporal variabilities between 7 and 90 days.

In contrast to traditional methods that simply remove an adjusted sinusoidal function and the long term mean from the original signal, a band-pass filter consists of a more robust way of isolating the mesoscale variability from the synoptic, annual and interannual variability, since it does not impose any shape or exact frequency to the part of the signal that will be attenuated by the filter. So, the band-pass Hann filter applied to the turbulent surface heat fluxes, removed not only long-period variabilities from the original data ( $T > 90$  days), but also the synoptic variability ( $T \leq 7$  days), that is non-negligible for air-sea interactions (GULEV; BELYAEV, 2012; NEIMAN; SHAPIRO, 1993). After the time filtering, the original turbulent heat fluxes signal ( $Q$ ), can be expressed as the sum of three components, as shown in Equation 3.5:

$$Q = Q_{syn} + Q_{band} + Q_{long}, \quad (3.5)$$

where  $Q_{syn}$  contains the synoptic variability,  $Q_{band}$ , the mesoscale variability, and  $Q_{long}$ , the long-period variability. The daily time-filtered heat fluxes maps ( $Q_{band}$ ) were then subsampled in time to match the SLA weekly maps from AVISO. We highlight the importance of filtering the fluxes for 7 days before subsampling, in order to avoid any

aliasing effect. An example of the time filtering process is presented in Figure 12, where the temporal variability in the scales of Equation 3.5 is clear.

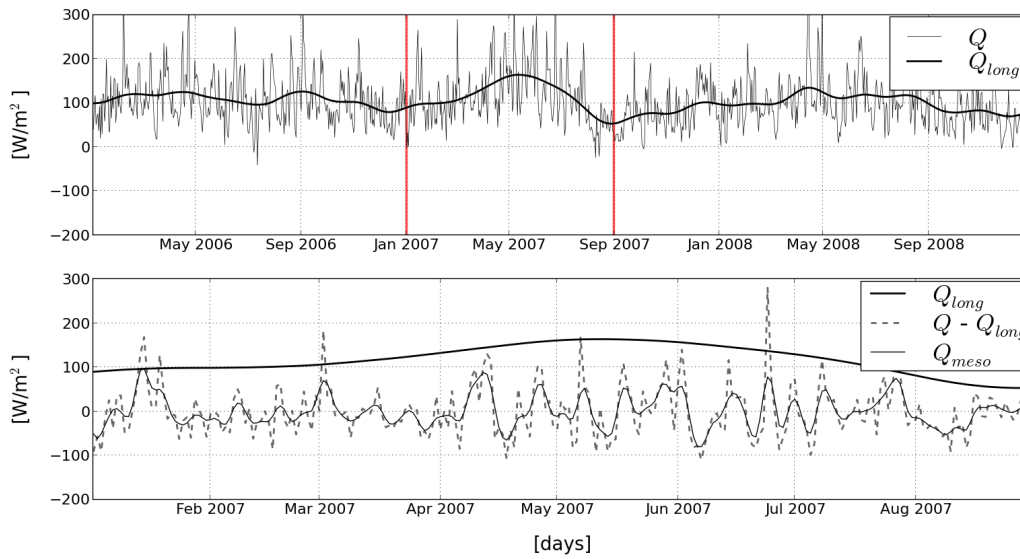


**Figure 12** – Example of the time filtering process applied to the LHF timeseries at ( $50^{\circ}\text{W}$ ,  $38^{\circ}\text{S}$ ). The upper panel shows three years of the original LHF timeseries (grey line), and the corresponding long period signal ( $T \geq 90$ ), calculated by the filter (thick black line). A zoom for the period marked by the red lines in the upper panel (Jan 2007 – Sep 2007) is shown in the lower panel. The dashed line corresponds to the original signal minus the long–period variabilities. The mesoscale component is shown in the thin black line.

Even after time filtering, mesoscale activity could still be masked by the signature of large scale features (HAUSMANN; CZAJA, 2012; GAUBE *et al.*, 2013). To compute the relative anomaly between the heat fluxes inside and outside eddies, it is necessary to define a reference level representative of the components in the heat flux signal that are not related with mesoscale eddies. In order to do so, we collocated the gridpoints limited by eddy contours to the time–filtered LHF and SHF maps (Figure 13A), and removed these points from the maps by setting them to “masks” (Figure 13B). Then, we applied to the masked maps a two–dimensional moving average Hann window of 600 km, obtaining smoothed maps where each gridpoint, including the masked ones, was replaced by the output from the moving average (Figure 13C). Finally, the heat fluxes anomaly maps were calculated by subtracting the smoothed maps (reference level) from the time–filtered maps (Figure 13D). The LHF and SHF anomalies caused by the eddies, were then retrieved from these anomaly maps by collocating the eddy contours to their respective location in the heat fluxes anomaly maps. This approach allows to better define the signature of mesoscale eddies on the surface turbulent heat fluxes, even if they are superimposed by large scale features. The window length was chosen based on the maximum averaged radius of the identified eddies ( $\sim 300$  km) and also on similar methodologies previously applied by other authors (*see* Chelton *et al.* (2011a), Gaube *et al.* (2013)).

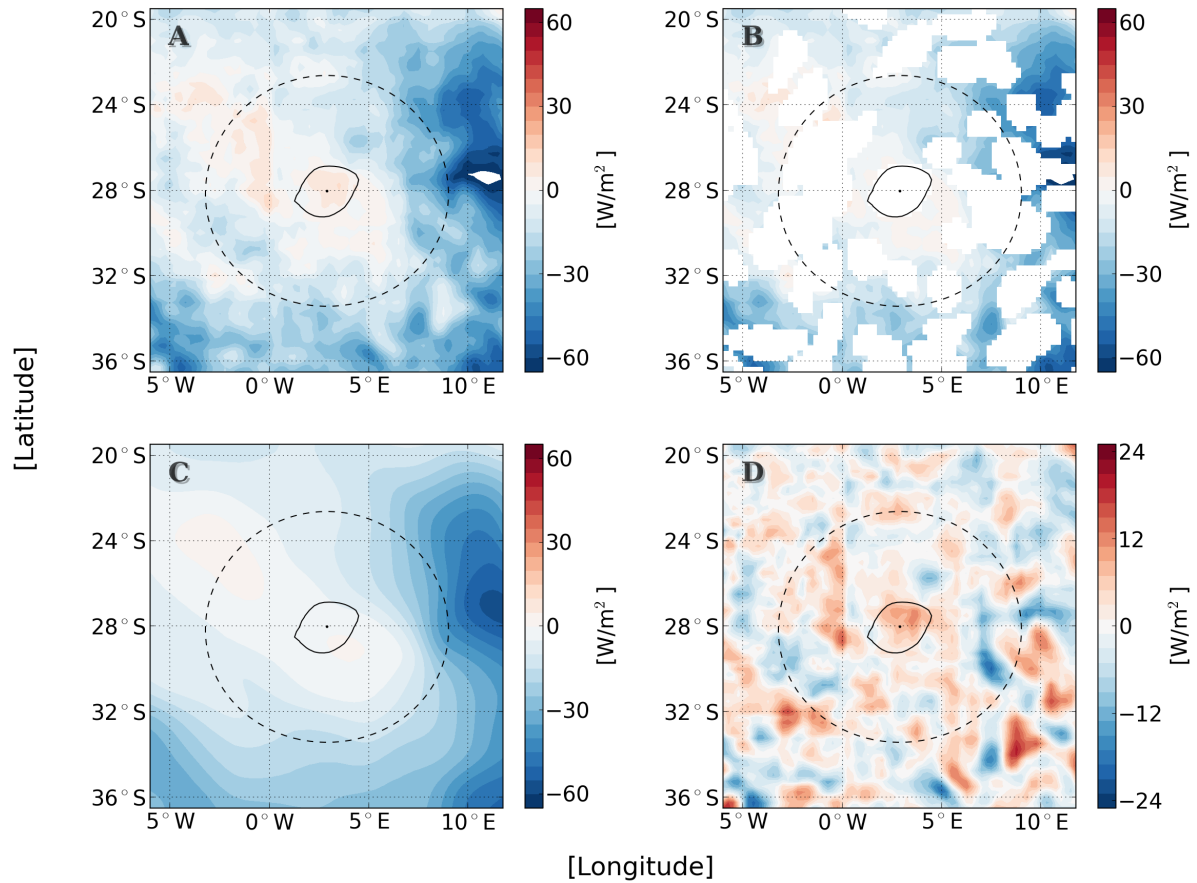


**Figure 13** – Steps for the definition of the surface heat fluxes anomalies in relation to a large-scale reference level. To illustrate, the contour a chosen eddy is drawn in solid black and its center marked with a dot. Points within a radius of 600 km from the eddy center are limited by the dashed circle, that corresponds to the window length. In this example the colors in all panels represents the LHF. Panel (A) is the time-filtered signal, which still contains large-scale spatial patterns. Panel (B) is the same map as panel (A), but with all gridpoints inside eddies set to mask. Panel (C) is the output from the spatial filter, corresponding to spatial scales larger than 600 km. Panel (D) is the anomaly map obtained by the subtraction of the large-scale smoothed maps (C) from the time-filtered maps (A).

### 3.2.2.2 Composite maps

The spatial pattern of the surface turbulent heat fluxes anomaly within the eddy interiors and their immediate surroundings was estimated using composite maps. For each eddy realization, the heat fluxes anomalies were interpolated to an uniform high-resolution grid, centered on the eddy center and normalized by the radial distance from the center to the eddy edge in each direction. The resolution of this normalized grid was such that the interval between two neighboring gridpoints was equal to 0.2 times the normalized radius. Figure 14 illustrates the normalization procedure. The extension of the normalized grid was chosen to represent the anomaly fields to a distance twice the eddy radius in each direction, so any difference between the pattern of the heat fluxes anomalies inside

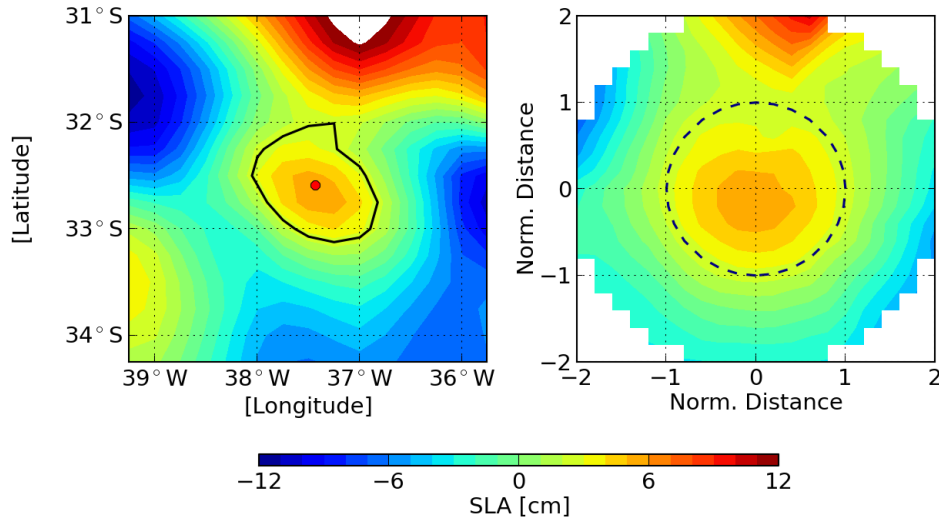


**Figure 14** – Example of the eddy normalization method, applied to construct the composite maps. To let it more explicit, the example is shown for the SLA field. The left panel shows the contour (solid black line) and the center (red dot) of an eddy in the original spatial coordinate system (latitude, longitude). The field inside the region limited by twice the eddy contour is then interpolated onto a high resolution regular grid, normalized by the distance between the eddy center and the edge in each direction. The result of such normalization is shown in the right panel, where the dashed circle limits the eddy interior.

and outside the eddies can be assessed. After the normalization, the anomaly fields of each eddy is represented on the normalized coordinate system as a circle of unitary radius (dashed contour in Figure 14), regardless of the original shape and size of the eddy. This normalization allows to average the anomaly of thousands of eddies as a single composite map, consisting of an efficient way to depict the mean signature of eddies on a given surface tracer (FRENGER *et al.*, 2013; CHELTON *et al.*, 2011a; HAUSMANN; CZAJA, 2012).

### 3.2.2.3 Statistical Analysis

To quantify how much of the variability in the total LHF and SHF signal is associated with the variability of mesoscale eddies we computed the proportion of explained variance ( $\sigma_{EXP}^2$ ) by approximating it to the squared correlation coefficient ( $r$ ) (CHOI, 1978), such that:

$$r^2 \approx \sigma_{EXP}^2 = \frac{\text{Variance Explained by the Eddies}}{\text{Total Variance}}. \quad (3.6)$$

For all the analysis performed, we adopted a threshold of 95% confidence level to consider the results statistically significant. In the averaged composite maps the mean values of the surface heat fluxes anomalies were also compared with the standard deviation of the samples.

## 4 Results and Discussion

### 4.1 Characteristics of Mesoscale Eddies in the South Atlantic

As discussed in Section 3.1.2, several physical and geometrical parameters useful to describe mesoscale eddies can be retrieved from the eddy identification method. We present next the main characteristics of mesoscale eddies in the SA obtained after applying Chaigneau *et al.* (2009)'s algorithm to the SLA maps. The importance of determining such characteristics with precision relies on the fact that the assessment of the contribution of the eddies to the surface turbulent heat fluxes are intrinsically related with how accurate are our estimates of the eddy radius, contour and amplitude, for example. To ensure the reliability of our eddy identification procedure, the results presented next were compared with the literature (e.g. Chelton *et al.* (2011b), Souza *et al.* (2011b)).

#### 4.1.1 Eddy frequency and polarity

Two important parameters that can be used to analyze the geographical distribution of mesoscale eddies are the eddy frequency and polarity. The eddy frequency gives the percentage of time that each grid point is inside an eddy during the whole timeseries. Thus, from a frequency map it is possible to assess in which regions mesoscale eddies occur more often and how often they occur for a given period. Mathematically, considering a gridpoint  $(x, y)$ , the eddy frequency in such point ( $f(x, y)$ ) is obtained by the ratio between the number of eddy realization in that point ( $N_{Eddies}(x, y)$ ) and the total length of the timeseries ( $N_t$ ), as shown in Equation 4.1:

$$f(x, y) = \frac{N_{Eddies}(x, y)}{N_t} 100\%. \quad (4.1)$$

For the 10-year studied period (1999–2009), cyclonic and anticyclonic eddies were frequently observed south of  $\sim 30^\circ$  S and more particularly near the BMC and AGR regions, where eddy frequency reaches 50–70% (Figure 15). In contrast, the eddy frequency strongly weakens in the tropical SA between  $10^\circ$  S and  $20^\circ$  S. As the Rossby radius becomes larger in the tropics (CHELTON *et al.*, 1998), so do the horizontal eddy scales. Thus, these relatively large-scale SLA associated with such eddies will be potentially full of small-scale SLA perturbations superimposed to them. As a result, a large eddy can be mistaken by several small eddies, which represents a challenge to the eddy identification algorithm, that will have a tendency to fail in identifying such features. Moreover, as the horizontal scale of these low-latitude eddies increases, they become more susceptible to the  $\beta$ -effect,

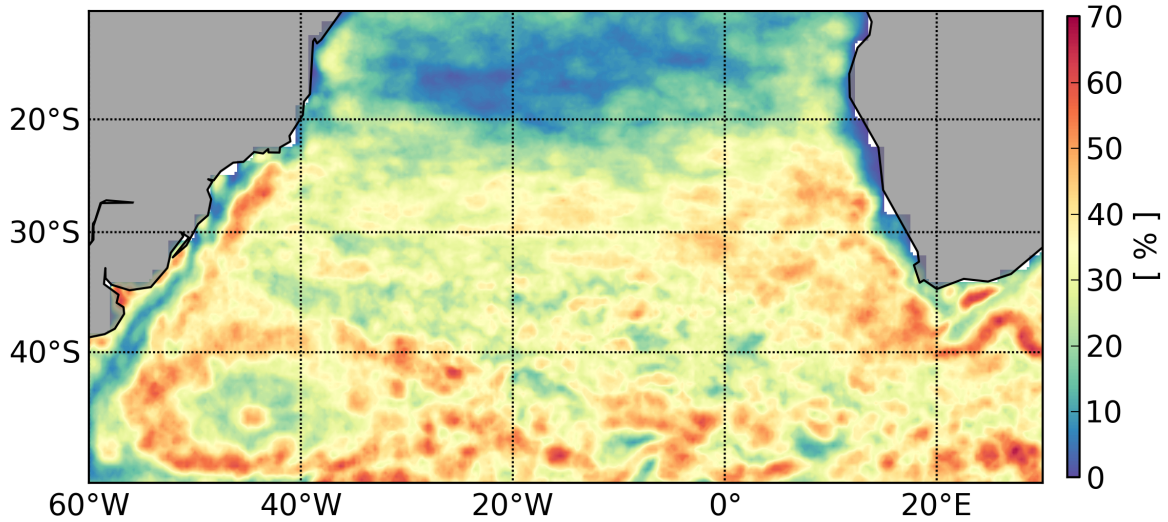


**Figure 15** – Map of the eddy frequency (in %) for the SA, which represents the percentage of time that the grid points are within an eddy. In the SA eddies can occur up to 70% of the time near the energetic regions of the BMC and AGR, while the frequency strongly weakens north of 20° S.

which adds a level of complexity to the geostrophic balance. The response of the ocean to this new balance is to propagate energy in the form of Rossby waves rather than mesoscale eddies (ROBINSON, 2010). Despite our focus is in the BMC and AGR regions, the eddy frequency is also relatively high near the Antarctic Circumpolar Current (ACC), south of 45° S. These results are very similar to the previously presented by other authors (e.g. Chelton *et al.* (2007), Chelton *et al.* (2011b), Saraceno and Provost (2012)), that shows high eddy activity near energetic regions. From Figure 15 it is also possible to note a region of relatively high eddy frequency northwestward off the AGR, associated with the propagation path of the Agulhas rings along the Agulhas ring corridor.

The eddy polarity represents the probability for each grid point to be inside a cyclonic (polarity < 0) or an anticyclonic (polarity > 0) eddy (CHAIGNEAU *et al.*, 2009). Thus, if  $f_c$  and  $f_a$  are respectively the frequency of cyclonic and anticyclonic eddies, the polarity ( $p$ ) is given by:

$$p = \frac{f_a - f_c}{f_a + f_c}. \quad (4.2)$$

Figure 16 shows the polarity map calculated as described in Equation 4.2. Overall, there is no significant preference between cyclones and anticyclones in most parts of the SA basin. Although it is clear that there is a majority of anticyclones in the region of the Agulhas ring corridor, as previously suggested in other studies (OLSON; EVANS, 1986; GONI *et al.*, 1997; SCHONTEN *et al.*, 2000; SOUZA *et al.*, 2011b). Some zonal bands of alternating mean eddy polarity in the middle of the basin (north of 35°S) are also noticeable in the polarity map. Similar banding patterns were reported previously by Chelton *et al.*

(2011b). This cyclonic/anticyclonic banding is also apparent near the BMC region where eddies are generally formed by the pinching off from meanders. On the equatorward side of a meander in the southern hemisphere, water parcels will be exposed to an increase in planetary vorticity and, by the conservation of potential vorticity, they will compensate by acquiring negative relative vorticity (clockwise). Thus, eddies formed in the equatorward side of such meander are more likely to be cyclonic. The opposite occurs in the poleward side, tending to generate more anticyclonic eddies. Such pattern of anticyclonic vorticity in the south and cyclonic in the north, is very clear near  $40^{\circ}\text{S}$  and  $40^{\circ}\text{W}$ .

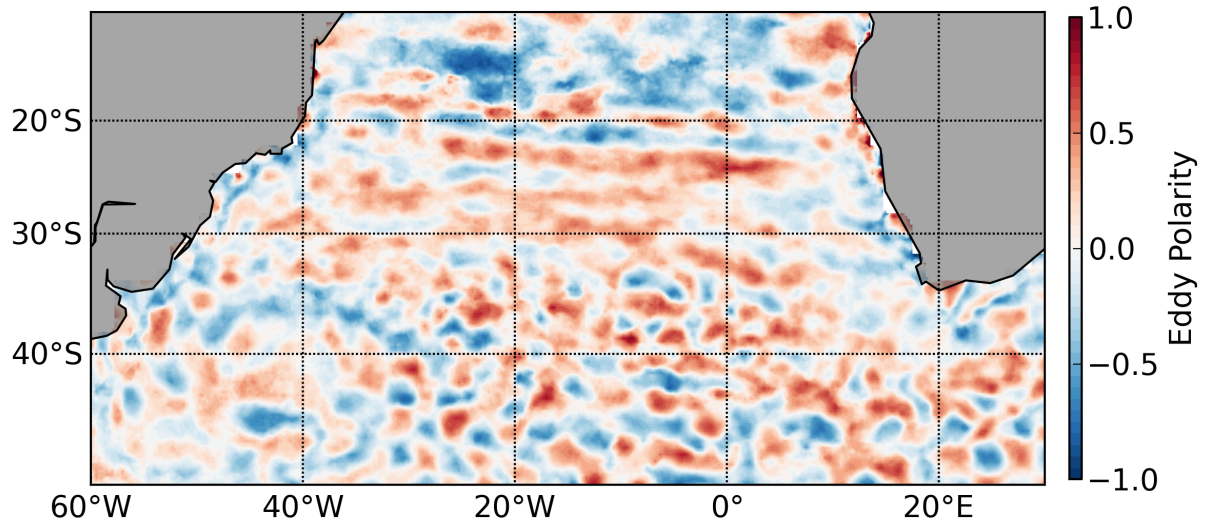


**Figure 16** – Polarity map for the eddies in the SA. Red (blue) regions, with  $p > 0$  ( $p < 0$ ), are characterized by a predominance of anticyclonic (cyclonic) eddies over cyclonic (anticyclonic).

#### 4.1.2 Eddy Radius

The temporal mean of the eddy radius ( $R$ ) computed for each gridpoint is shown in Figure 17 (top). The radii grow towards the equator, reaching their maximum values at latitudes north of  $20^{\circ}\text{S}$ . Such behavior is driven by dependency of the baroclinic Rossby radius of deformation ( $Rd_i$ ) with the Coriolis parameter, and thus with latitude. As discussed in Section 1.1.2,  $Rd_i$  determines the minimum spatial scale for a perturbation in the ocean to adjust to the geostrophic balance. Hence, the minimum eddy radius in each latitude is dictated by the respective value of  $Rd_i$ . Figure 17 (bottom) shows the comparison between the zonally averaged eddy radius, and the zonally averaged values of  $Rd_i$  calculated by (CHELTON *et al.*, 1998). The shape of the two curves are very similar, although the values of  $R$  are always greater than  $Rd_i$ , as predicted by the theory. Values for the zonally averaged  $R$ , ranges from  $\sim 60$  km in subpolar latitudes to  $\sim 150$  km in tropical latitudes. The geographical distribution of the eddy radius found by Chelton *et al.* (2011b), is shown

in Figure 18. Despite of their eddy identification methodology being slightly different from Chaigneau *et al.* (2009)'s, it is also based on closed contours of SLA. Both the mean radius map and the zonally averaged radii curve of Figure 18 are in very good agreement with our results. In addition, Souza *et al.* (2011b) have also obtained similar results by using Chaigneau *et al.* (2009)'s method. As shown in the histogram of Figure 19, there is no significant difference between the eddy radius for cyclonic and anticyclonic eddies. For both polarities, the eddy radii ranges approximately from 25 km to 200 km, with the modes<sup>1</sup> of the distributions approximately equal to 70 km.

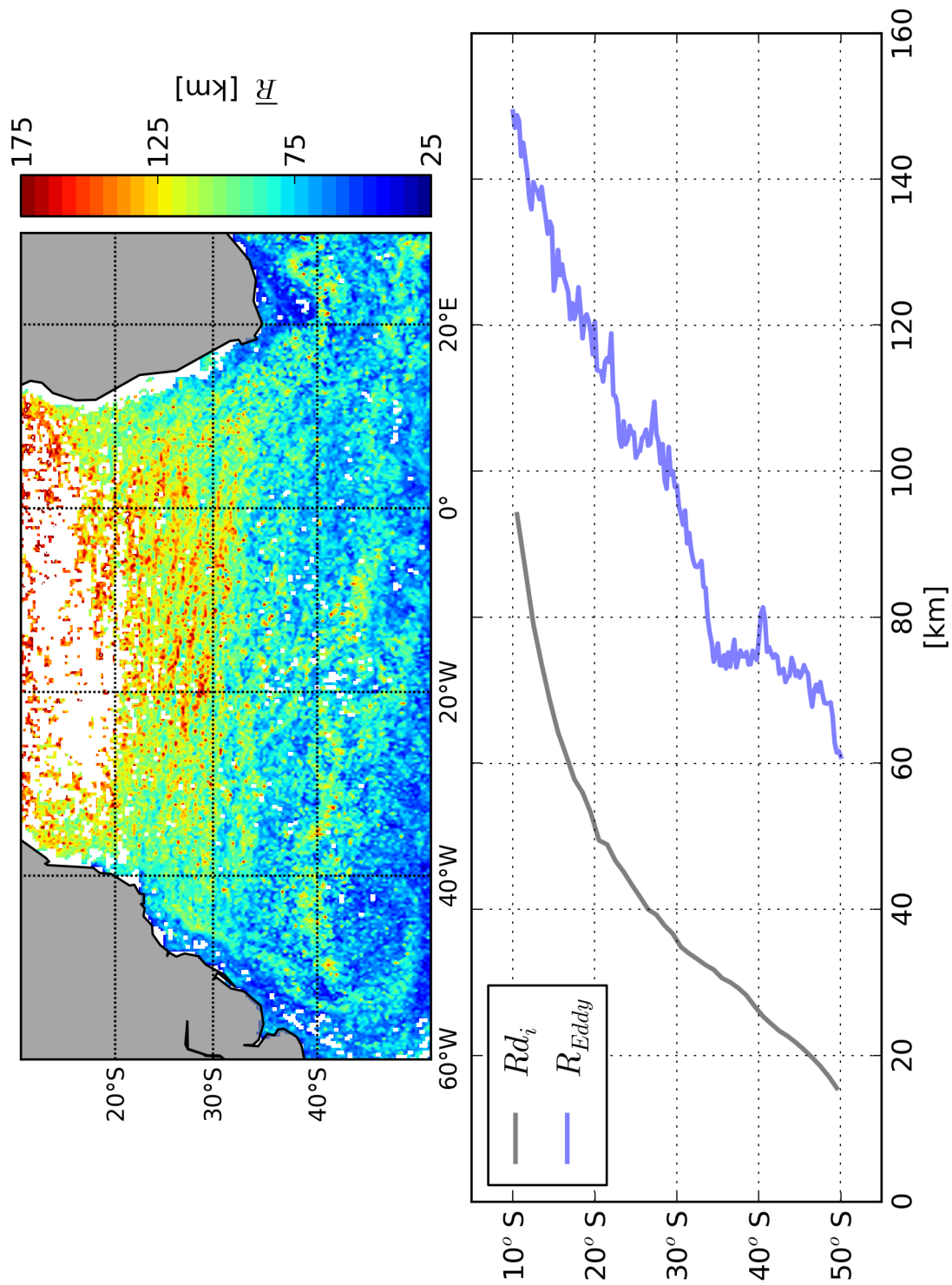
### 4.1.3 Eddy Amplitude

Figure 20 shows the geographical distribution of the mean eddy absolute amplitude. In most regions of the SA, the mean amplitude is lower than 10 cm. However, in the energetic regions of the AGR and BMC, eddy amplitudes can reach up to 50 cm. As described in Section 2.1, these regions are characterized by being highly unstable, with intense SLA variability associated with eddy formation. Indeed the mean amplitude map of Figure 20, strongly resembles the map of the standard deviation of the SLA (Figure 6). As the eddies propagate they start to decay and, therefore, it would also be expected higher mean amplitude in regions of eddy genesis.

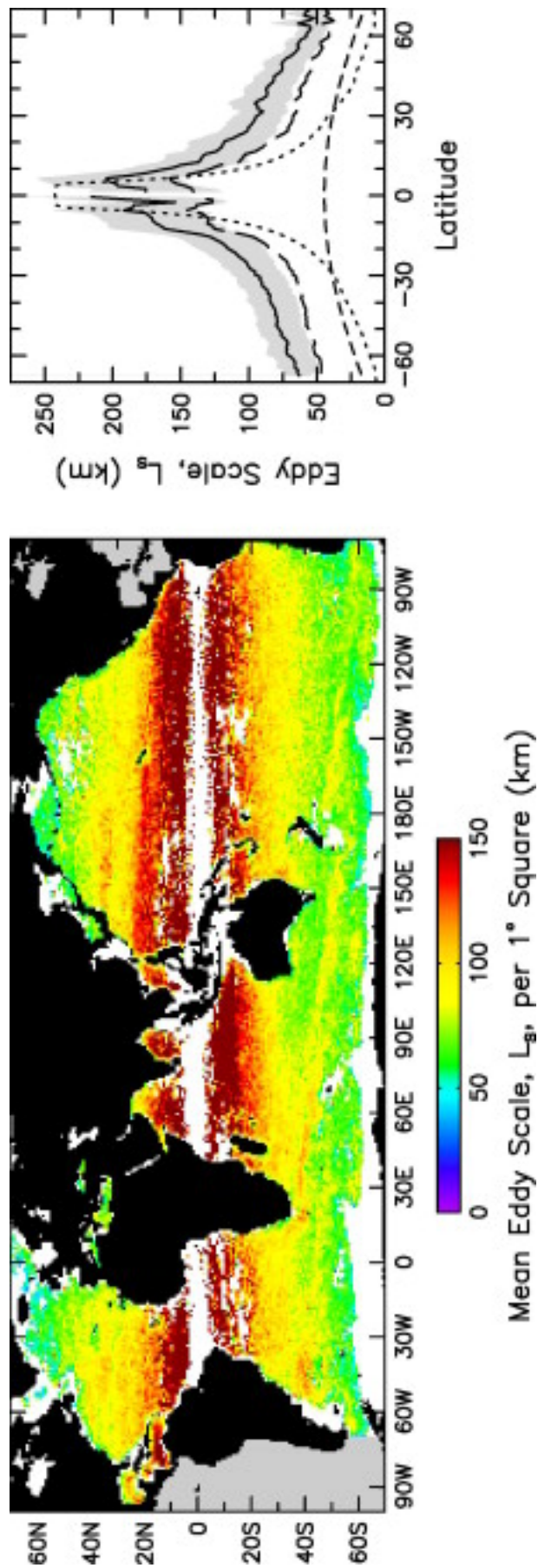
The distribution of the observed amplitudes is shown in the histogram of Figure 21, for cyclonic and anticyclonic eddies separately. Most of the eddy amplitudes are concentrated in low values. As a matter of fact, 50% of the eddies have amplitudes lower than 5 cm, and only 25% have amplitudes higher than 10 cm. Another interesting point that can be observed from the amplitude distribution in Figure 21 is that there is a slight difference between cyclonic and anticyclonic eddies as we look at higher amplitudes. Such difference is in a way that higher amplitude eddies are preferentially cyclonic. One hypotheses to explain this difference could be based on the effect of the gradient wind (PEDLOSKY, 1987), by which in a rotating fluid, the centrifugal force would push the fluid parcels outward, having the effect of attenuating high pressure anomalies caused by anticyclones and enhancing low pressure anomalies in cyclones (CHELTON *et al.*, 2011b).

Figure 22 shows the zonal average of the eddy amplitude as a function of latitude, together with the respective standard deviation and interquartile (25% –75%) range. The main amplitude peak near 40°S, reflects the combined contribution of eddies from the northern part of the BMC with the large–amplitude Agulhas rings and eddies. The secondary amplitude peak near 48°S is associated with eddies formed in the southern portion of the BMC region as well as the eddies of the ACC. For both the geographical and the statistical distribution of the eddy amplitudes, our results are comparable to the results obtained by Chelton *et al.* (2011b) (Figure 23) and Souza *et al.* (2011b).

<sup>1</sup> The mode gives the most common value in a given distribution.



**Figure 17** – Mean eddy radii, on the top panel. In the bottom panel it is shown the comparison between the zonal mean of the first baroclinic mode of the Rossby radii ( $R_{d_i}$ ) (gray) and the zonal mean of the eddy radii (blue), as a function of latitude. The values for  $R_{d_i}$  were obtained from (CHELTON *et al.*, 1998).



**Figure 18** – Global distribution of the mean eddy scale (equivalent to the eddy radius) from Chelton *et al.* (2011b) (left). The right panel shows the zonally averaged eddy scale (solid black line) and the zonally averaged  $Rd_i$  (short dashed line).

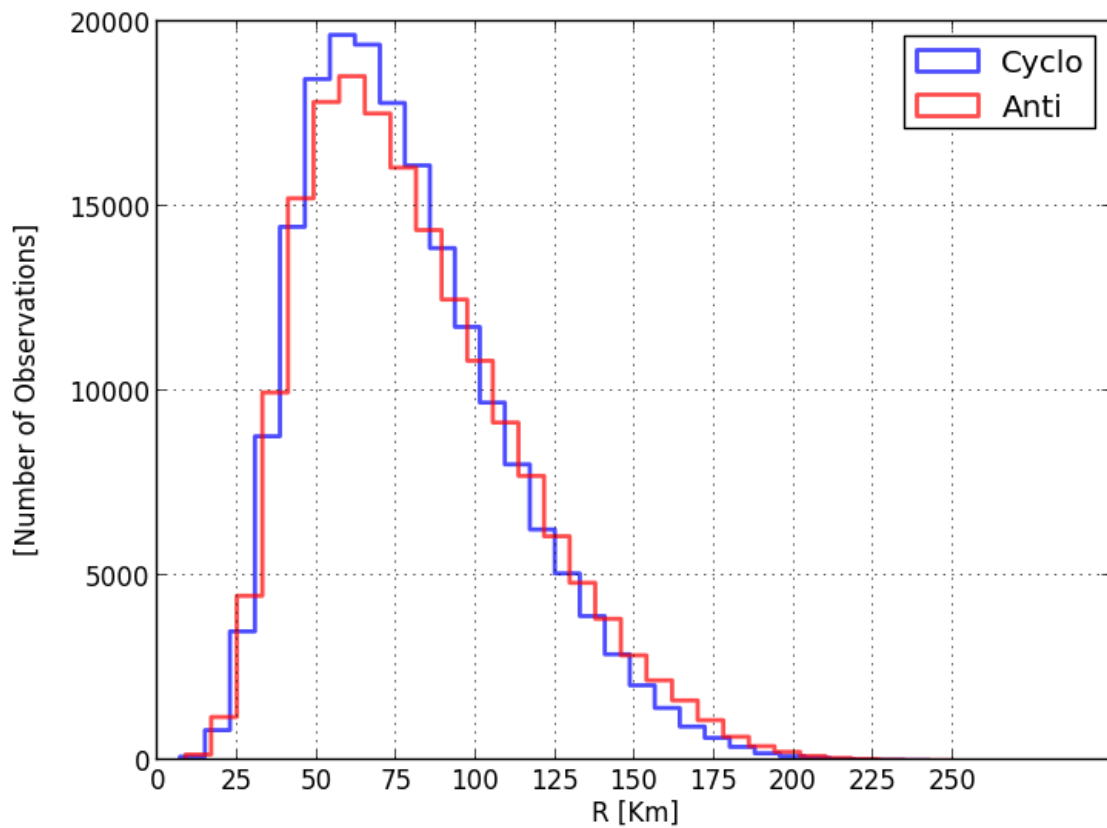


**Figure 19** – Distribution of the eddy radius for cyclonic (blue) and anticyclonic eddies (red). The mode of the distribution for cyclonic eddies is  $\sim 70.8$  km and for anticyclonic eddies is  $\sim 72$  km.

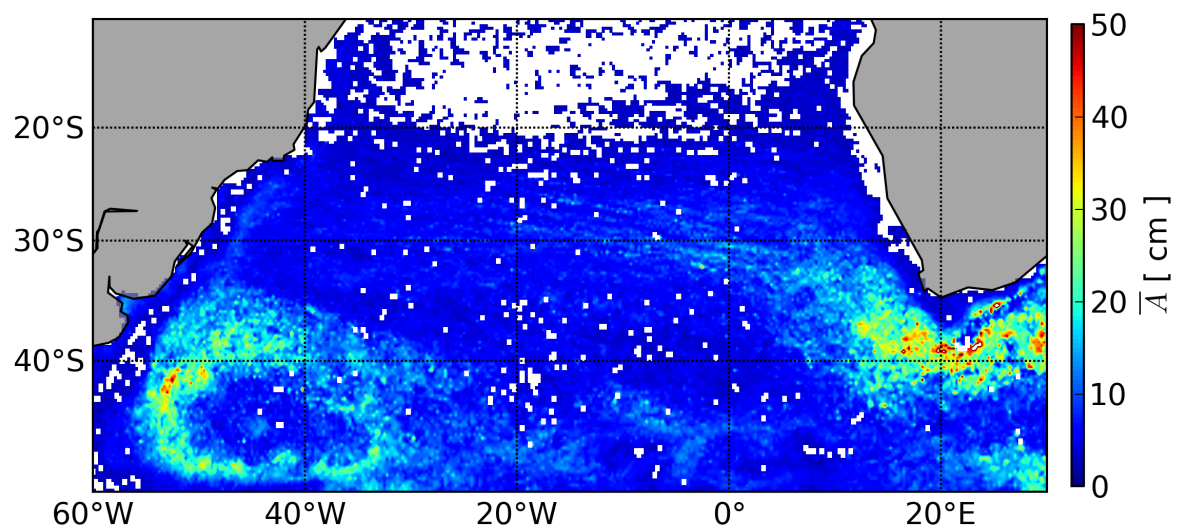


**Figure 20** – Geographical distribution of the mean eddy amplitude in the SA.

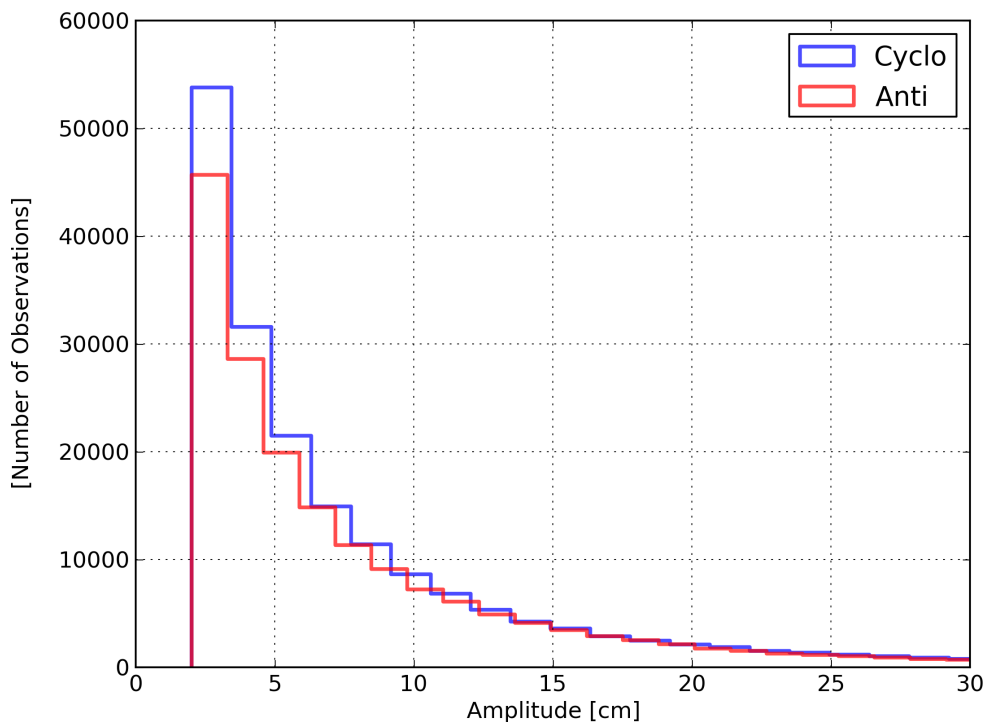


**Figure 21** – Distribution of the eddy amplitude for cyclonic (blue) and anticyclonic eddies (red). The mode of the distribution for both polarities is  $\sim 3$  cm.

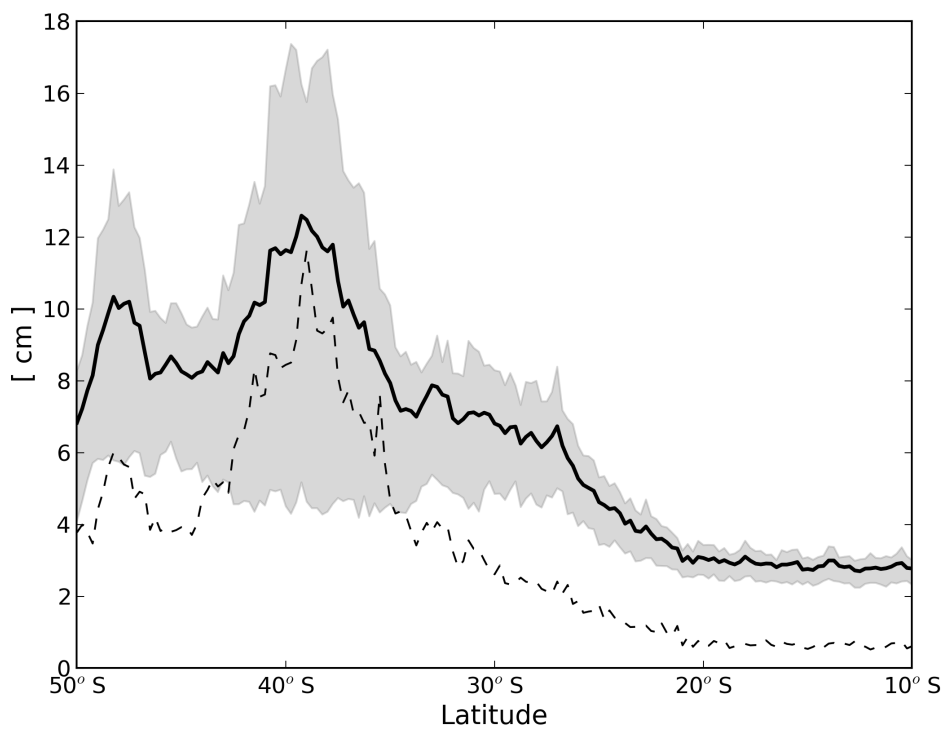


**Figure 22** – Zonally averaged eddy amplitude as a function of latitude (solid black line) and the respective interquartile range (25%–75%), in gray, and standard deviation, in the dashed line.

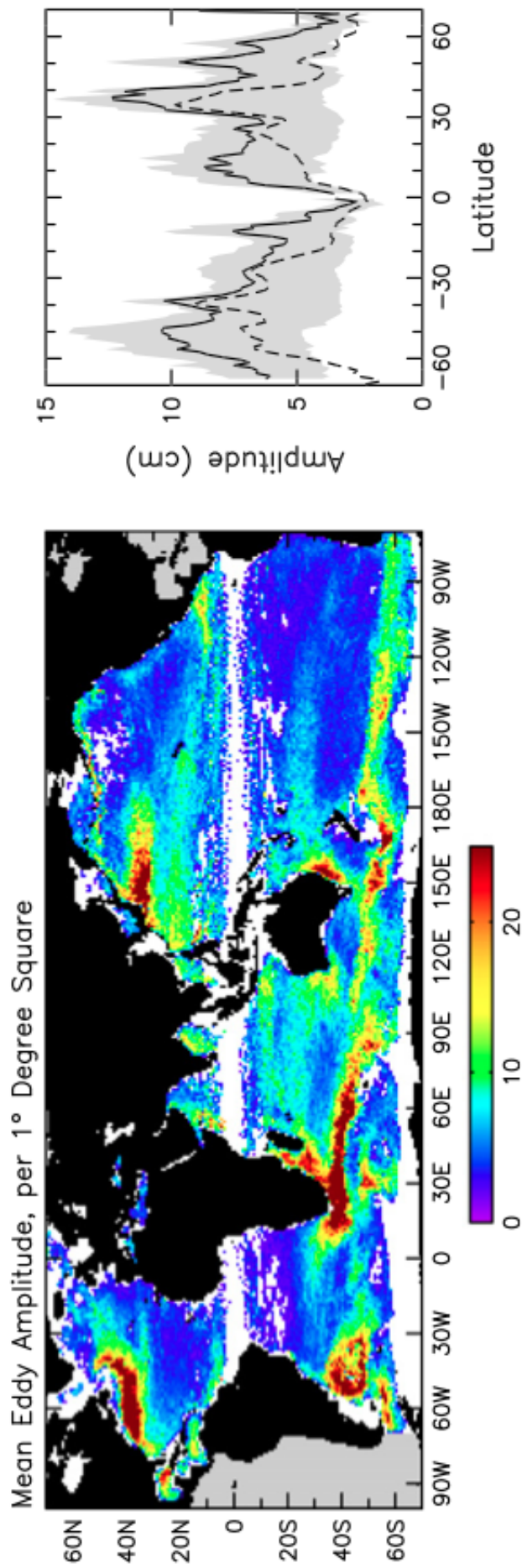


**Figure 23** – Mean eddy amplitude (left) and zonally averaged amplitude (right) from Chelton *et al.* (2011b). In the right panel the mean is shown in the solid black line, the standard deviation, in the dashed line, and the interquartile (25% –75%) in the gray shadow.

## 4.2 Surface Turbulent Heat Fluxes Analysis

To investigate the isolated contribution of mesoscale eddies to the surface turbulent heat fluxes, it is necessary to establish the principal characteristics of the total LHF and SHF signal, in order to quantify how intense and statistically significant the eddy anomalies are when compared to the total heat fluxes signal. In the next sections, we first present and discuss some general results for the total LHF and SHF in the SA (from the original IFREMER data), followed by the results for the heat fluxes **anomalies** associated with the eddies.

### 4.2.1 Mean and Standard Deviation of the Surface Turbulent Heat Fluxes

The average behavior of the surface turbulent heat fluxes in the SA were assessed by calculating maps of the temporal mean and standard deviation of the LHF and SHF. Figure 24 (panel A and B) shows the mean and the standard deviation of the LHF, respectively. The mean LHF is positive over all the SA basin (ocean heat loss), increasing equatorwards. It reaches the highest mean values near the AGR ( $\sim 180\text{--}200\text{ W/m}^2$ ) and its minimum in the region of the ACC, south of  $45^\circ\text{S}$  ( $0\text{--}50\text{ W/m}^2$ ). The region of relatively intense latent heat loss north of  $20^\circ\text{S}$  and between  $10\text{--}40^\circ\text{W}$  is associated with the constant and strong winds in the region. It is possible to notice the intense surface heat flux gradient featured by the encounter of the two major currents of the southwestern SA. On average, the warm BC is characterized by a relatively strong surface latent heat loss of about  $100\text{--}140\text{ W/m}^2$ , while the cold MC is marked by a much weaker latent heat loss of about  $10\text{--}30\text{ W/m}^2$ . Similarly in southeastern SA, the intrusion of the AC, carrying warm water from the Indian ocean to the SA, promotes a strong LHF gradient near the AGR region.

The variability patterns of the SHF (Figure 25) resembles the LHF. Although, heat exchanges between ocean and atmosphere in the form of SHF are much less intense, ranging from  $-20\text{ W/m}^2$  to  $70\text{ W/m}^2$ . A very similar characteristic of strong heat flux gradient near the BMC and AGR observed on the mean LHF, is also apparent in the mean SHF map (Figure 25A). The region of the relatively cold ACC, south of  $45^\circ\text{S}$ , is marked on average by heat gain through SHF. The same occurs in African coast, along the flow of the BCS, where coastal upwelling brings cold water to the surface. The map of the standard deviation of the LHF (Figure 24B) and SHF (Figure 25B) can be complemented by the seasonal variations of both fluxes, shown in Figure 26 (left and right, respectively). The surface turbulent heat fluxes are more intense during the austral winter (August) than in the summer (January). We also note strong seasonal variations of both the LHF and SHF near the energetic regions of the BMC and AGR.

The zonal average of the LHF and SHF, as well as the sum of the two, are shown in Figure 27, where the difference between the magnitudes of LHF and the SHF are even

more explicit. On average the magnitude of the SHF is about one tenth of the magnitude of the LHF, and values in all bands of latitude for both components are positive. There is a maximum in both fluxes near  $40^{\circ}\text{S}$ , reflecting the strong surface turbulent heat loss that is characteristic of the AGR region. It is also noteworthy that the curve for the sum of the total surface turbulent heat fluxes (LHF+SHF) presents almost the same variability than the zonal average of the LHF, reflecting that the variability of the turbulent fluxes is dominated by the variability of the LHF, a fact also addressed by Yu and Weller (2007).

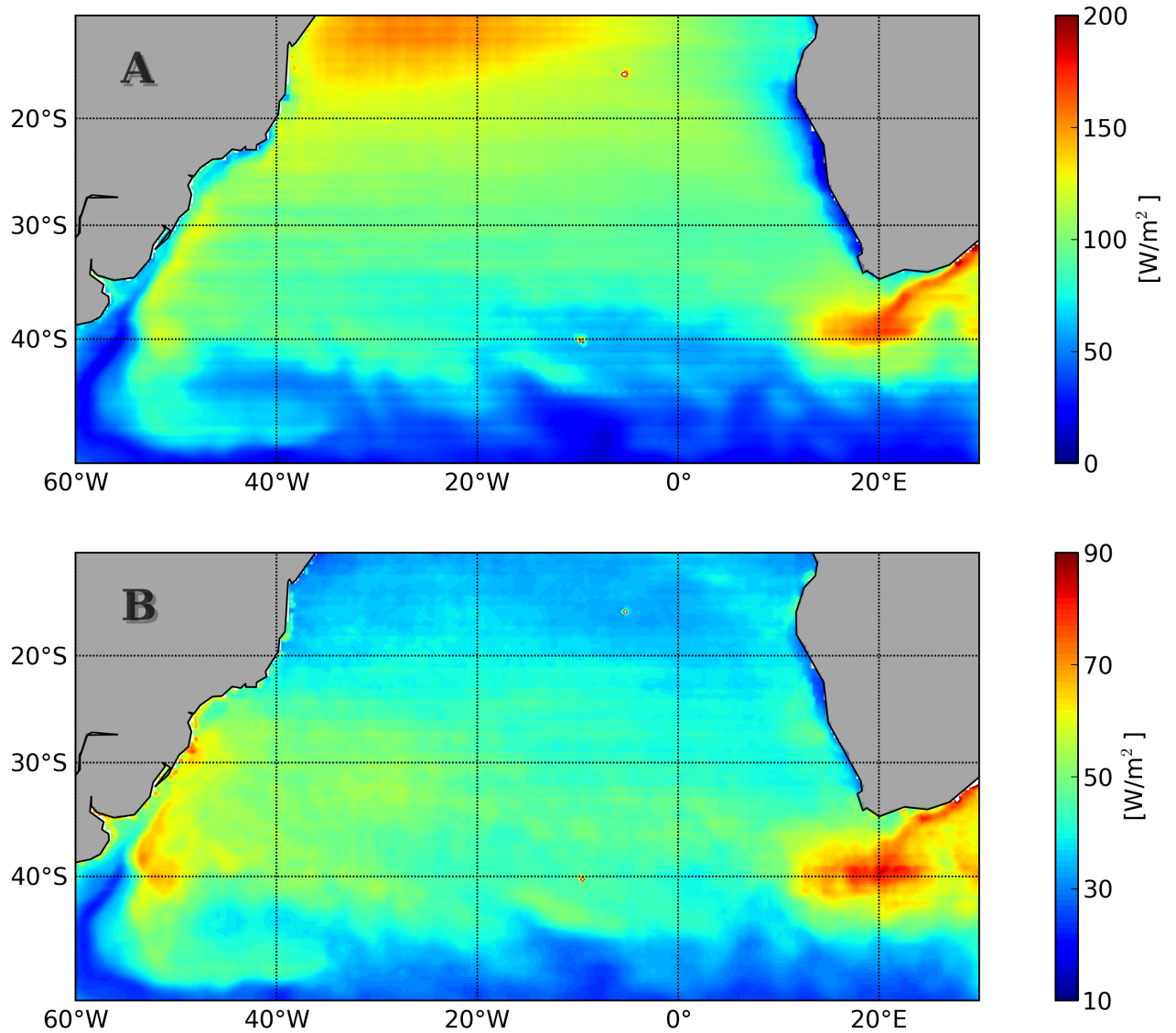


**Figure 24** – Temporal mean (A) and standard deviation (B) of the LHF in the SA, for the period from 1999 to 2009, in  $\text{W}/\text{m}^2$ . Positive upward fluxes indicate ocean heat loss, while downward negative, ocean heat gain.

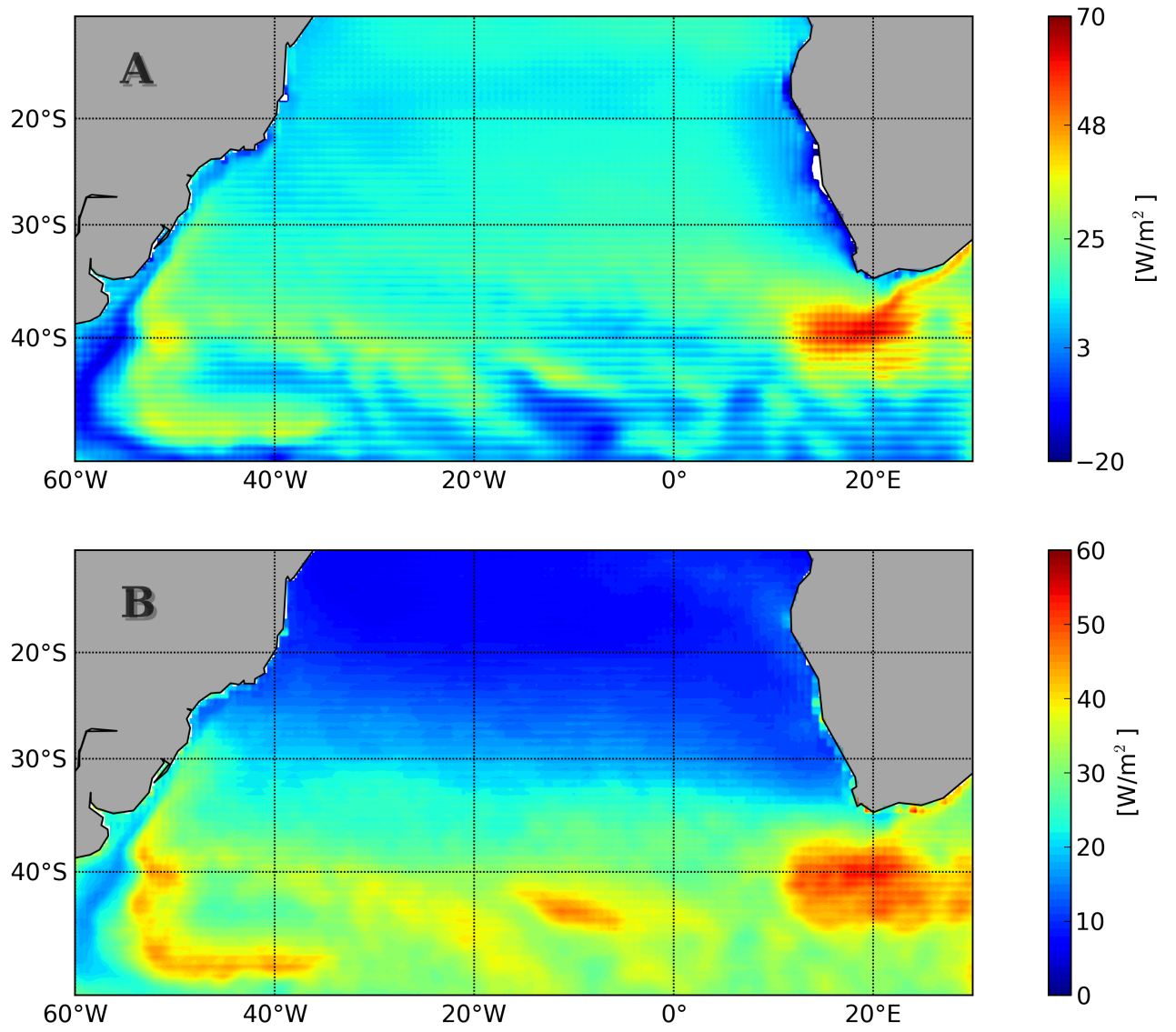


**Figure 25** – Same as Figure 24, but for the SHF.

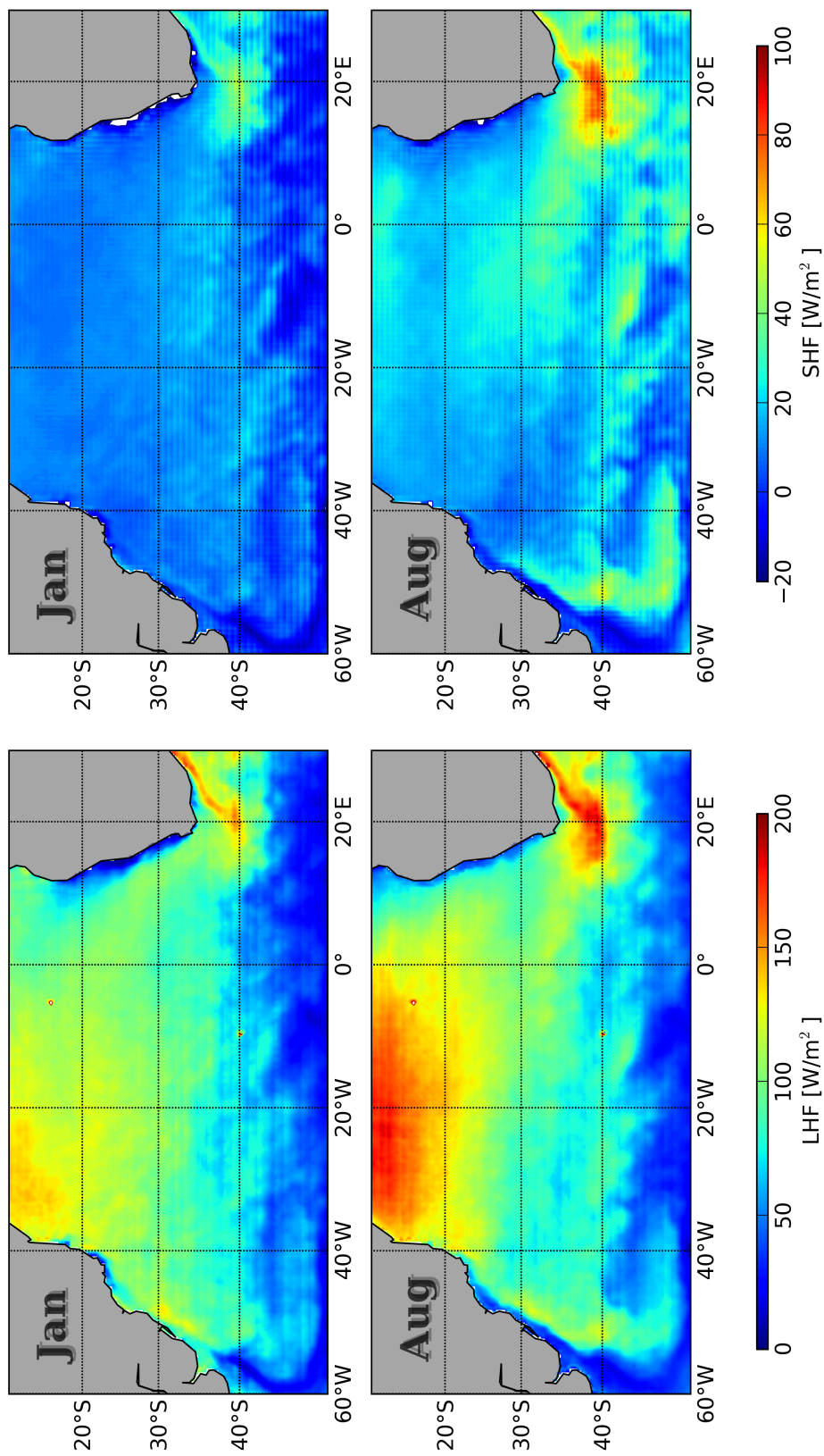


**Figure 26** – Maps of the mean surface turbulent heat fluxes averaged for the summer (January) and winter (August). Results for the LHF are shown in the left panels and for the SHF in the right panels.

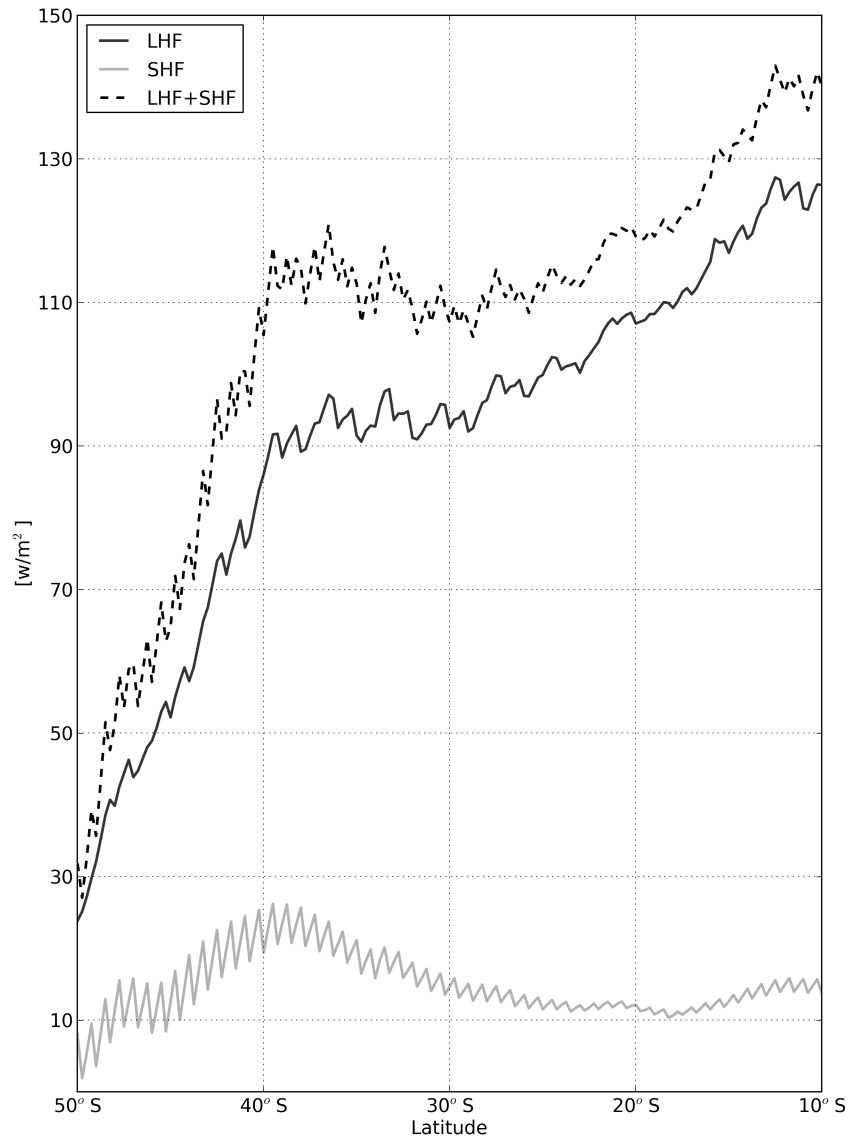


**Figure 27** – Zonally averaged surface turbulent heat fluxes in the SA. The LHF is shown in solid black, the SHF in light grey and, the sum of the two in the dashed line.

## 4.2.2 Geographical Distribution of the Mean Turbulent Heat Fluxes Anomalies Associated With Mesoscale Eddies

Figure 28 shows the mean LHF and SHF anomalies associated with mesoscale eddies in the SA. Such mean maps were obtained by averaging in time the heat fluxes anomalies, as defined in Section 3.2.2.1, considering only the gridpoints inside cyclonic and anticyclonic eddies, separately. It is possible to observe from the maps of Figure 28 a clear signature of eddies on both components of the surface turbulent heat fluxes, particularly in the BMC and AGR regions, where the anomalies are of one order of magnitude more intense than in the rest of the basin, reaching up to  $\pm 20 \text{ W/m}^2$ . Moreover, warm-core anticyclonic eddies contribute on average to positive heat fluxes anomalies (ocean heat loss), while cold-core cyclonic eddies contribute to negative anomalies (ocean heat gain). Such difference regarding the eddy polarity can be explained by the dependency of the turbulent fluxes with some state variables, such as the SST.

From the bulk parameterizations of the SHF (Equation 1.3) it is straightforward that for a given air temperature, positive SST anomalies lead to positive SHF anomalies, while negative SST anomalies, lead to negative SHF anomalies. As explained in Section 1.1.2, cyclonic eddies promote the doming of the isopycnals, bringing cooler water closer to the surface and, therefore, being marked by negative SST anomalies. The opposite occurs for anticyclones. Thus, cyclonic eddies will preferentially be associated with negative SST anomalies and as a consequence, negative SHF anomalies. In contrast, anticyclonic eddies will contribute with positive SHF anomalies. In the case of the LHF, the same argument is valid, although it is necessary to recall that the saturated air specific humidity ( $q_s$ ) is also a function of the SST (LARGE; YEAGER, 2009). Thus, a given SST anomaly indirectly leads to a LHF anomaly with the same sign.

This hypothesis applies for most eddies identified from satellite altimetry. However, we remark that there is also another type of mesoscale eddies, dynamically distinct from those described in Section 1.1.2. Such eddies are known for being subsurface-intensified; they are generally formed from subsurface currents, and are characterized by having a subsurface core. Despite the signature of subsurface-intensified eddies on the SST being generally weak (ROBINSON, 2010), it is important to note that they could lead to opposite SST anomalies (positive for cyclones and negative for anticyclones) (CHAIGNEAU *et al.*, 2011; COLAS *et al.*, 2012) and would probably impact turbulent heat fluxes in a different way. However, determining the exact nature (surface or subsurface-intensified) of the eddies is beyond the scope of this work and exploring potential differences between the impact of surface and subsurface intensified eddies on the LHF and SHF anomalies will deserve future studies.

Table 3 shows the mean and the maximum values of the LHF and SHF anomalies

associated with the eddies, observed in the BMC and AGR regions. For comparison purpose, it is also shown the averages for all the SA basin, as well as the annual range (minimum and maximum) of the total LHF and SHF signal. More specifically, the annual range in each region was obtained from the monthly mean of the original IFREMER data, as in Figure 26. On average over the whole SA, the intensities of the turbulent heat fluxes anomalies related to mesoscale eddies are weak ( $1\text{--}2\text{ W/m}^2$ ), compared to the annual range ( $8\text{--}11\text{ W/m}^2$  for the SHF, and  $70\text{--}82\text{ W/m}^2$  for the LHF). However, anomalies can locally be of the same order of magnitude as the large-scale annual cycle in the energetic regions, such as in the BMC region for the SHF ( $\approx 10\text{ W/m}^2$ ). To assess how significant are the heat fluxes anomalies caused by the eddies in comparison to the total heat fluxes variability, we computed the proportion of the variance of the original LHF and SHF data that can be explained by the variance of the eddy anomalies. Once more, the overall results for the SA show that eddies poorly contribute to the variability of the LHF and SHF signals. Nonetheless, the variance explained by the eddies in the energetic regions is remarkably higher than in rest of the basin, and it can account for up to 20–30% of the variance of the total LHF and SHF signals, at the 95% confidence level.

We have compared the heat fluxes anomalies caused solely by the eddies with the total heat fluxes signal, but how are the anomalies inside the eddies distinct from the outside? Do they have the same magnitude? Figure 29 shows the LHF and SHF anomalies averaged only for gridpoints outside eddies (panels B and D, respectively), as well as the average of the sum of the heat fluxes anomalies inside cyclones and anticyclones (panels A and C, respectively). It is clear that the anomalies caused by the eddies are much intenser than the anomalies outside. The later, are distributed randomly around zero, only assuming slightly greater absolute values near the BMC and AGR. Therefore, eddies indeed stand for the greatest contributors in the mesoscale turbulent heat fluxes.

It is also noteworthy that the geographical distribution of the anomalies inside cyclonic and anticyclonic eddies are not exactly symmetric. Despite the intensity of the anomalies in the combined cyclonic and anticyclonic average, is about half ( $\pm 8\text{ W/m}^2$ ) of the intensity observed in the maps separated by polarity (Figure 28), it is evident from panels A and C of Figure 29, that such anomalies do not cancel each other, particularly in the BMC and AGR region. One hypothesis to explain the patterns observed in the combined cyclonic and anticyclonic averaging of the LHF and SHF anomalies, can be based on the same reasons presented in the discussion of the geographical distribution of the eddy polarity, in Section 4.1.1 and Figure 16. The alternating areas of heat gain, in the northern part, and heat loss, in the southern part, of the BMC and AGR, reflects the predominance of cyclonic and anticyclonic eddies, respectively. Thus, we could extrapolate our results for other ocean basins in a way that, regions where cyclonic eddies are predominant, will be marked by surface turbulent heat gain anomalies, while regions dominated by anticyclonic

eddies will be marked by heat loss anomalies.

Although air–sea interactions have been believed to be dominated by large–scale and synoptic processes (BOURASSA *et al.*, 2010; FRENGER *et al.*, 2013), our results strongly suggest that eddies can play a significant role on the variability of the surface turbulent heat fluxes, at least in some regions, giving evidence of a coupling between ocean and atmosphere at mesoscales. Such evidence reinforces recent findings of (CHELTON; XIE, 2010), (SONG *et al.*, 2009), and (FRENGER *et al.*, 2013). One could question why are the eddy imprints stronger in the eddy–rich regions than in the rest of the basin? Hausmann and Czaja (2012) identified eddies from altimetry data and analyzed their anomalies on the SST using measurements from microwave radiometer, for the North Atlantic and Southern Ocean. The authors found that the SST anomalies associated with mesoscale eddies are stronger in energetic regions near the Gulf Stream and the ACC, both characterized by high SLA variability. Since high SLA variability is indeed associated with large–amplitude eddies (CHELTON *et al.*, 2011b), we explore instead the dependency of LHF and SHF anomalies on the eddy amplitude, as presented in the following section.

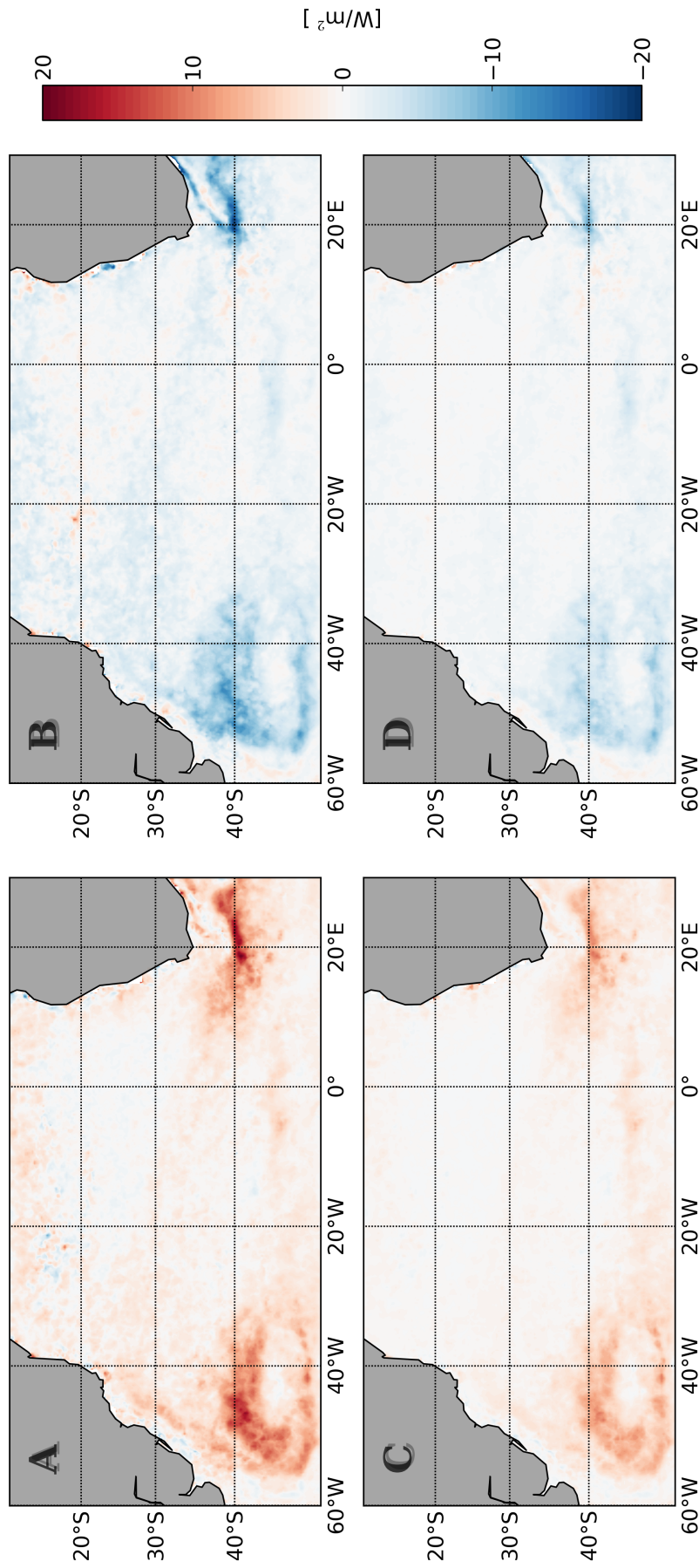


**Figure 28** – Mean surface turbulent heat fluxes anomalies associated with mesoscale eddies in the South Atlantic. Mean latent heat flux (LHF, in  $\text{W/m}^2$ ) anomalies within (A) anticyclonic and (B) cyclonic eddies. Mean sensible heat flux (SHF, in  $\text{W/m}^2$ ) anomalies within (C) anticyclonic and (D) cyclonic eddies.

	LHF			SHF		
	BMC	AGR	SA	BMC	AGR	SA
Anticyclonic [ $\text{W}/\text{m}^2$ ]	6-18	4-20	2	4-11	3-11	1
Cyclonic [ $\text{W}/\text{m}^2$ ]	-(5-13)	-(3-19)	-1	-(3-9)	-(2-10)	-1
Annual Range [ $\text{W}/\text{m}^2$ ]	56-65	81-95	70-82	5-14	22-26	8-11
Exp. Var. [%]	7-21	6-16	3	8-29	7-21	3

**Table 3** – Anticyclonic (Cyclonic): Mean and maximum (minimum) values of LHF and SHF anomalies associated with anticyclonic (cyclonic) eddies observed in the BMC and AGR regions. For the whole SA just the mean is shown. Annual Range: large-scale LHF and SHF annual cycle. Exp. Var.: mean and maximum percentage of the variance of the total LHF and SHF signals explained by the variance of the heat fluxes anomalies caused by the eddies. All values are statistically significant at the 95% confidence level.

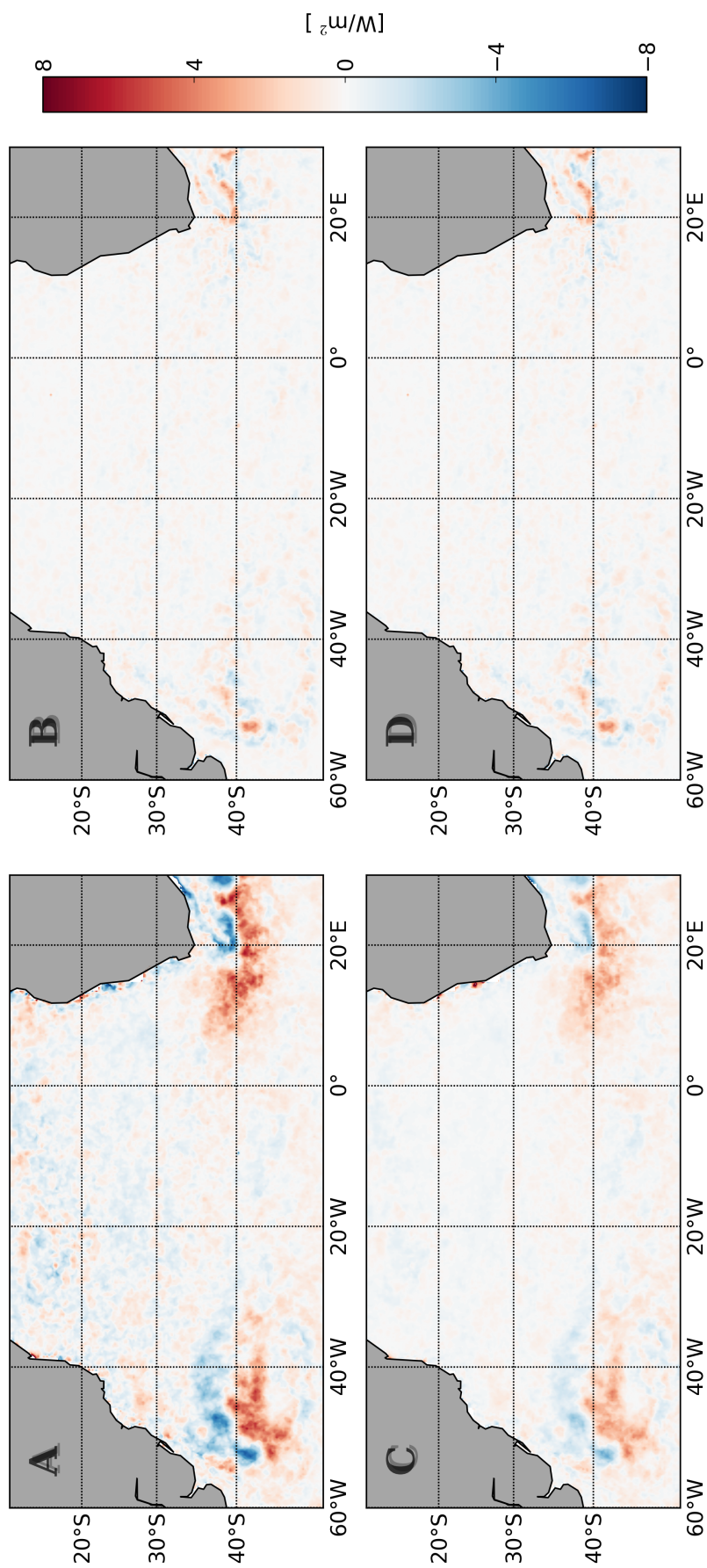


**Figure 29** – Maps of the mean LHF anomaly (top) for the combined contribution of cyclonic and anticyclonic eddies (A), and for gridpoints outside eddies (B). Mean SHF anomaly (bottom) for the combined contribution of cyclonic and anticyclonic eddies (C), and for gridpoints outside eddies (D).

### 4.2.3 Averaged Composite Maps

To assess the mean spatial pattern of the turbulent heat fluxes anomalies within the eddy interiors and their vicinities, normalized maps of the surface turbulent heat fluxes anomalies for cyclonic and anticyclonic eddies were constructed as explained in Section 3.2.2.2, considering all eddies detected in the SA. To explore the connection between the heat fluxes anomalies and the eddy amplitude, the normalized heat fluxes anomaly maps were segregated by eddy polarity and by eddy amplitude range, such that the subgroups would consist of the 10% lowest amplitude eddies, the 10–20% lowest amplitude eddies, the 20–30% lowest amplitude eddies, and so on. Table 4 shows the amplitude ranges associated with the respective percentiles. Since amplitude variations among the percentiles increase nonlinearly, the interval between the 90<sup>th</sup> and the 100<sup>th</sup> was reduced to half (5%), so the variations of the mean heat fluxes inside large–amplitude eddies can be explored with more detail. Each subgroup accounts on average for  $\sim 8600$  anticyclonic eddy realizations and  $\sim 9000$  cyclonic eddy realization, except for the 90–95<sup>th</sup> and 95–100<sup>th</sup> percentiles, where the average number of eddies is reduced to half.

Percentile [%]	Amplitude Range [cm]
0–10	2.1–2.4
10–20	2.4–2.9
20–30	2.9–3.5
30–40	3.5–4.3
40–50	4.3–5.4
50–60	5.4–6.8
60–70	6.8–8.9
70–80	8.9–12.1
80–90	12.1–18.8
90–95	18.8–27.3
95–100	> 27.3

**Table 4** – Eddy amplitude range representative for each percentile, calculated with a 10% increment from each other, except for the 90–95<sup>th</sup> and 95–100<sup>th</sup>, that have a 5% interval.

Composite maps were then calculated by averaging the heat fluxes anomalies in each subgroup individually. Figure 30 shows the maximum (minimum) value of the LHF and SHF anomalies inside the averaged composite maps for anticyclonic (cyclonic) eddies as a function of the respective eddy amplitude.

Regardless of the eddy polarity (cyclonic or anticyclonic), the magnitude of the LHF and SHF anomalies increases with the eddy amplitude in a nonlinear way, varying between  $\pm(1-10)$   $\text{W/m}^2$ , for the LHF, and  $\pm(0.5-6)$   $\text{W/m}^2$ , for the SHF. The order of magnitude is similar for both eddy types but are negative (positive) for cyclonic (anticyclonic) eddies. Similarly to what is observed in large-scale averages of surface turbulent heat fluxes over the SA (YU; WELLER, 2007), the LHF anomalies associated with mesoscale eddies are generally greater than the SHF anomalies.

Considering that the majority of the identified eddies are surface-intensified, cyclonic eddies will promote the doming of the isopycnals leading to negative SLA and SST anomalies, while anticyclonic eddies will dip down the isopycnals, leading to positive SLA and SST anomalies. The larger the eddy amplitude, stronger will be the isopycnal deformation, and the mixed-layer temperature anomalies (e.g. Holte *et al.* (2013)). Consequently, stronger will be the turbulent heat fluxes anomalies. For low-amplitude eddies ( $< 15$  cm), the heat fluxes anomalies are weak and do not significantly vary among the subgroups. However, anomalies strongly increase as we look at amplitudes higher than  $\sim 15$  cm. Such response, becomes even more explicit in the Figures 31 – 41, that will be discussed next.

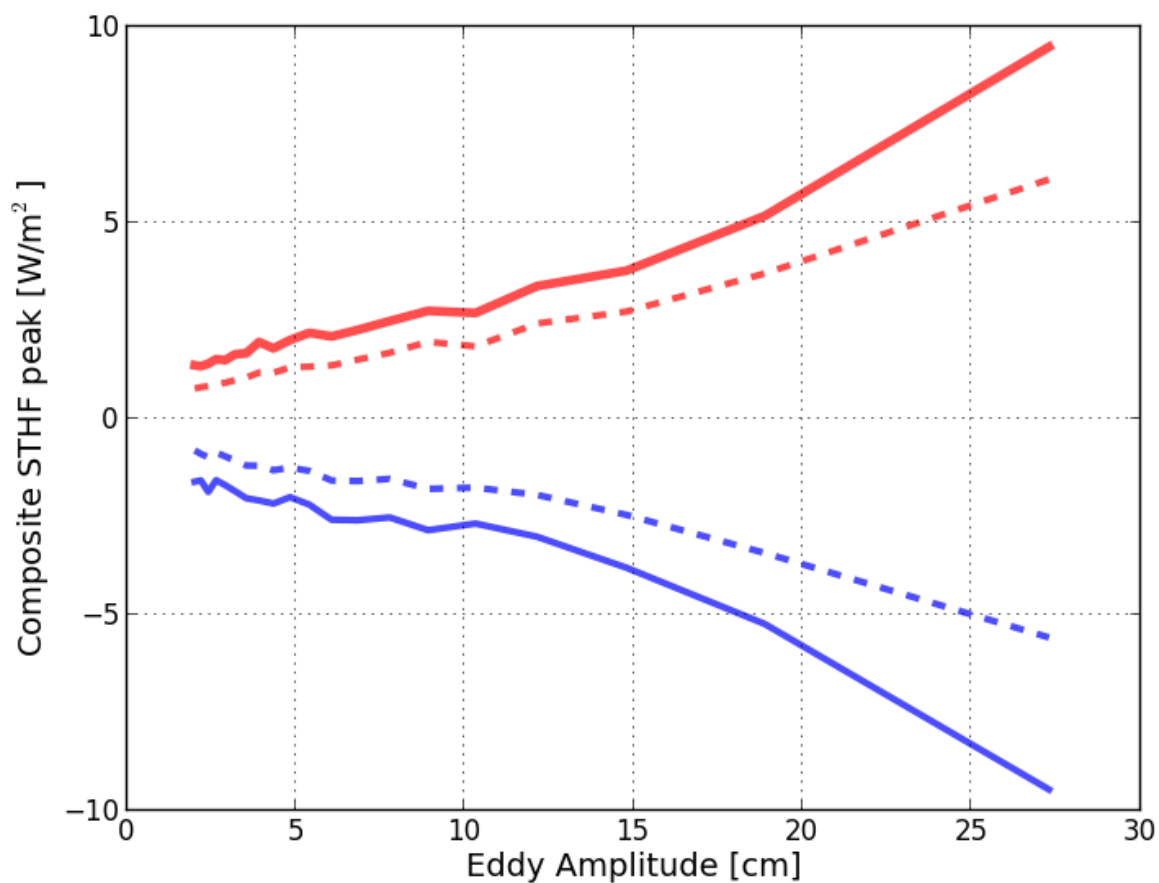


**Figure 30** – Maximum (minimum, for cyclonic eddies) surface turbulent heat fluxes anomalies within anticyclonic (red lines) and cyclonic (blue lines) eddies as a function of the eddy amplitude. The solid and dashed lines are the LHF and SHF, respectively. Mean turbulent heat fluxes anomalies were computed by individually averaging each subgroup of normalized maps.

The mean spatial distribution of the surface turbulent heat fluxes anomalies inside large–amplitude eddies is shown in Figure 31. Such composite maps were obtained by averaging heat fluxes anomalies within all eddies with the 5% largest amplitudes ( $\geq 27$  cm), corresponding to  $\sim 3900$  cyclonic and  $\sim 4500$  anticyclonic eddies. Near the center of large–amplitude eddies, the mean LHF and SHF anomalies are of the order of  $\pm 10$  W/m<sup>2</sup> and  $\pm 6$  W/m<sup>2</sup>, respectively. The LHF and SHF anomalies decrease outward, reaching minimum absolute values ( $\sim 0$  W/m<sup>2</sup>) near the eddy edge ( $|d|=1$ ), and generally changing the sign of the anomalies outside the eddy contours ( $|d| > 1$ ). Such wave–like pattern could be a sign of the radiation of Rossby waves by the eddies, as previously observed in numerical modeling and altimetry data (FLIERL, 1984; MCWILLIAMS; FLIERL, 1979; EARLY *et al.*, 2011). Despite we do not explore here whether or not the pattern observed in the periphery of the eddies in the composite maps are associated with Rossby waves, we acknowledge the similarity between such pattern and the Figure 1 of Early *et al.* (2011), for example.

Figure 31 (C, D, G, H) shows the absolute values of the heat fluxes anomalies, in meridional and zonal profiles of the composite maps, crossing the point of maximum (minimum for cyclones) anomaly. It is possible to note, that the maximum absolute LHF and SHF anomalies are not exactly aligned with the eddy centers. In the meridional profiles (D, H), the maximum absolute anomalies of both the LHF and SHF presents a equatorward shifting for cyclonic eddies and a poleward shifting for anticyclonic eddies. From the zonal profiles (C, G), we note a slightly eastward shifting of the absolute maximum in cyclonic eddies, while for anticyclonic eddies the peak is coincident with the eddy center.

Composite maps averaged for the other amplitude ranges listed in Table 4, are shown in descending order from Figures 32 to 41. Despite of the fact that the intensity of the heat fluxes anomalies can reach very low magnitudes for small–amplitude eddies ( $\pm 0.8$  W/m<sup>2</sup>), it is surprising that the spatial pattern of the anomalies within the eddy cores remains persistent regardless of the eddy amplitude. Even though the standard deviation of the heat fluxes anomalies inside composite maps can be of the same order of magnitude as the anomalies themselves, the mean anomalies in the composite maps are statistically significant at the 95% confidence level. The robustness of our results for heat fluxes anomalies in the averaged composites comes as a consequence of the large number of analyzed eddies in each subgroup ( $\sim 5000$ – $10000$  for each polarity). Indeed, the advantage of using normalized coordinates to analyze the eddies relies in the possibility of averaging thousands of eddies as a single composite, as also highlighted by Frenger *et al.* (2013) and Gaube *et al.* (2013).

As we can see from the meridional profiles of the composite maps (Figures 32 to 41), the direction of the meridional asymmetry is persistent in almost all subgroups. The persistence of the equatorward shifting for cyclones and poleward shifting for anticyclonic,

even for small magnitude heat fluxes anomalies, suggests that such effect might be related with the dynamics of the eddies themselves. Therefore we could explain the observed meridional shifting on the basis of the physics governing mesoscale eddies dynamics and propagation. As suggested by early work on the dynamics of rotating fluids (e.g. Adem (1956), Firing and Beardsley (1976), McWilliams and Flierl (1979)), as the fluid parcels rotate with the eddy, they undergo a change in planetary vorticity due to the  $\beta$ -effect. In order to preserve their potential vorticity, fluid parcels at the northern and southern flanks of the eddy will then compensate the planetary vorticity change by modifying their relative vorticity. In the southern hemisphere, this results in a weak vorticity anomaly dipole that induce upwelling in the northern flank of cyclonic eddies and downwelling in the southern flank. Thus, in cold-core cyclonic eddies, the cooler water brought up by the upwelling would enhance the negative heat fluxes anomalies in the northern flank, as observed in Figure 31–41. The opposite would happen to anticyclonic eddies, producing enhanced positive heat fluxes in the southern flank of the eddies.

Although this hypothesis explains the meridional shifting observed in the composites it does not apply to the zonal shifting. In fact it is hard to establish whether or not the zonal shifting is significant, considering that it strongly varies among the subgroups. We were not able to determine the pattern nor the reason for the east–west oscillations of the position of the heat fluxes anomaly peaks in the composites. Similar results regarding the asymmetric imprint of mesoscale eddies in averaged composite maps were also found by Hausmann and Czaja (2012) when analyzing composite maps of SST anomalies in mesoscale eddies. In contrast to our results, the authors found a persistent westward shifting of the SST anomaly for both cyclonic and anticyclonic eddies. Although the authors discussed the consequences of such shifting for the meridional transport of heat, an explanation for what causes the shifting were not provided. However it is important to note that not only the authors have computed the averaged composites for the SST, instead of the turbulent heat flux, but also they have applied a distinct methodology from ours to define the anomalies in respect to the large-scale. The turbulent heat fluxes are not a function of the SST exclusively, therefore the contribution of other variables, such as the wind, could also be responsible for explaining the differences between our results and those obtained by Hausmann and Czaja (2012). Further analysis considering the anomalies of each input variable of the LHF and SHF are needed to better assess this issue.

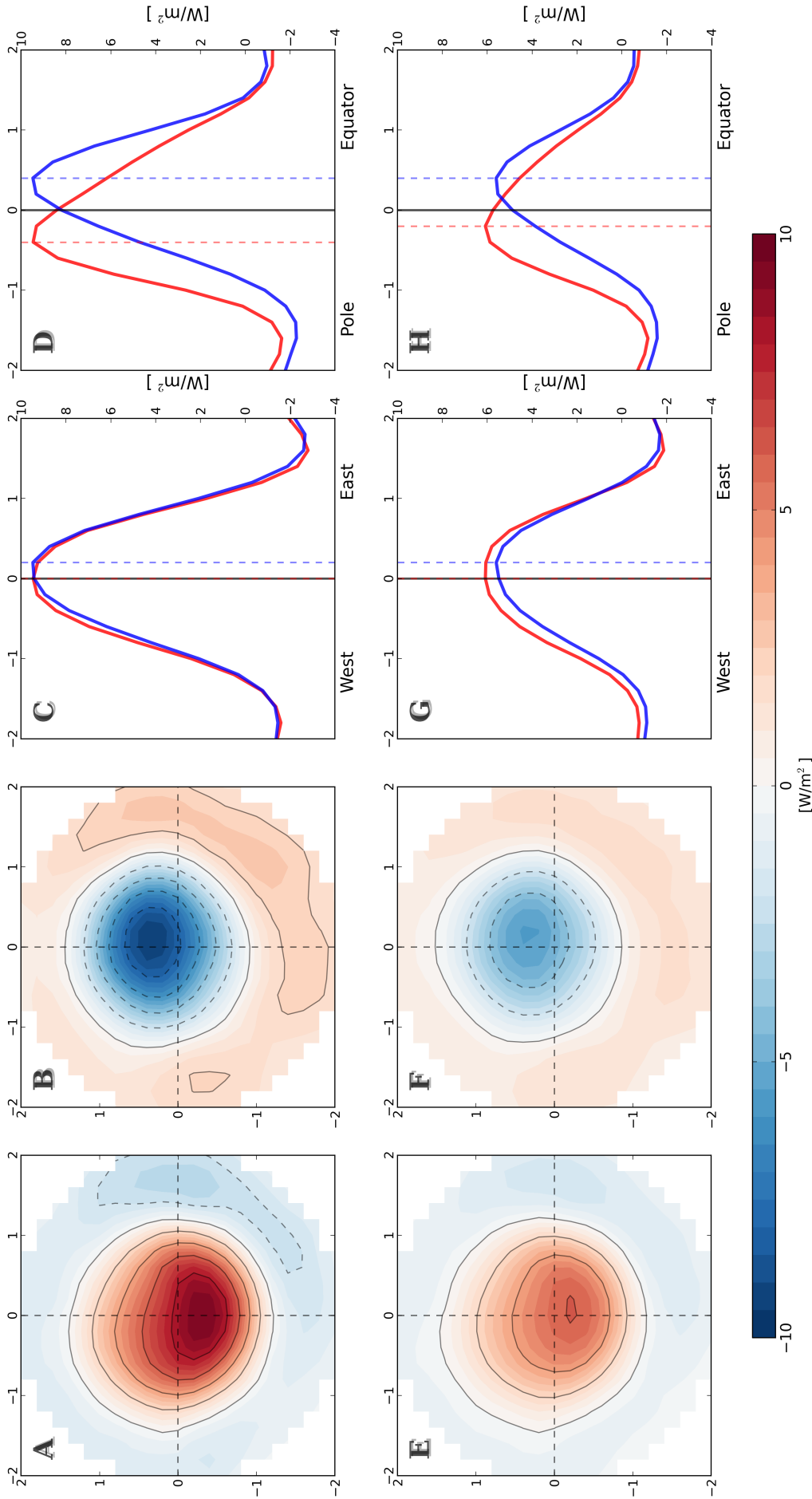


**Figure 31** – Averaged composite maps of LHF (A, B) and SHF (E, F) anomalies associated with anticyclonic (A, E) and cyclonic (B, F) eddies. Composites were obtained from eddies having the 5% highest absolute amplitudes ( $\geq 27.3$  cm) that corresponds to 4564 cyclonic and 3974 anticyclonic eddies. The axes in the maps are the normalized distance  $d$  between the eddy center ( $d = 0$ ) and twice the eddy edge ( $d = 2$ ). Contour intervals are shown every 2  $W/m^2$ . Panels (C, D) show the absolute value of the zonal and meridional profile of the LHF anomalies in the composites, respectively. Profiles were traced crossing the point of maximum (minimum for cyclones) anomalies. Anomalies of anticyclonic eddies are in red lines, and cyclonic eddies in blue lines. The positions where the extreme values in the profiles occur, are marked by a dashed line. Panels (G, H) are the same, for the SHF.

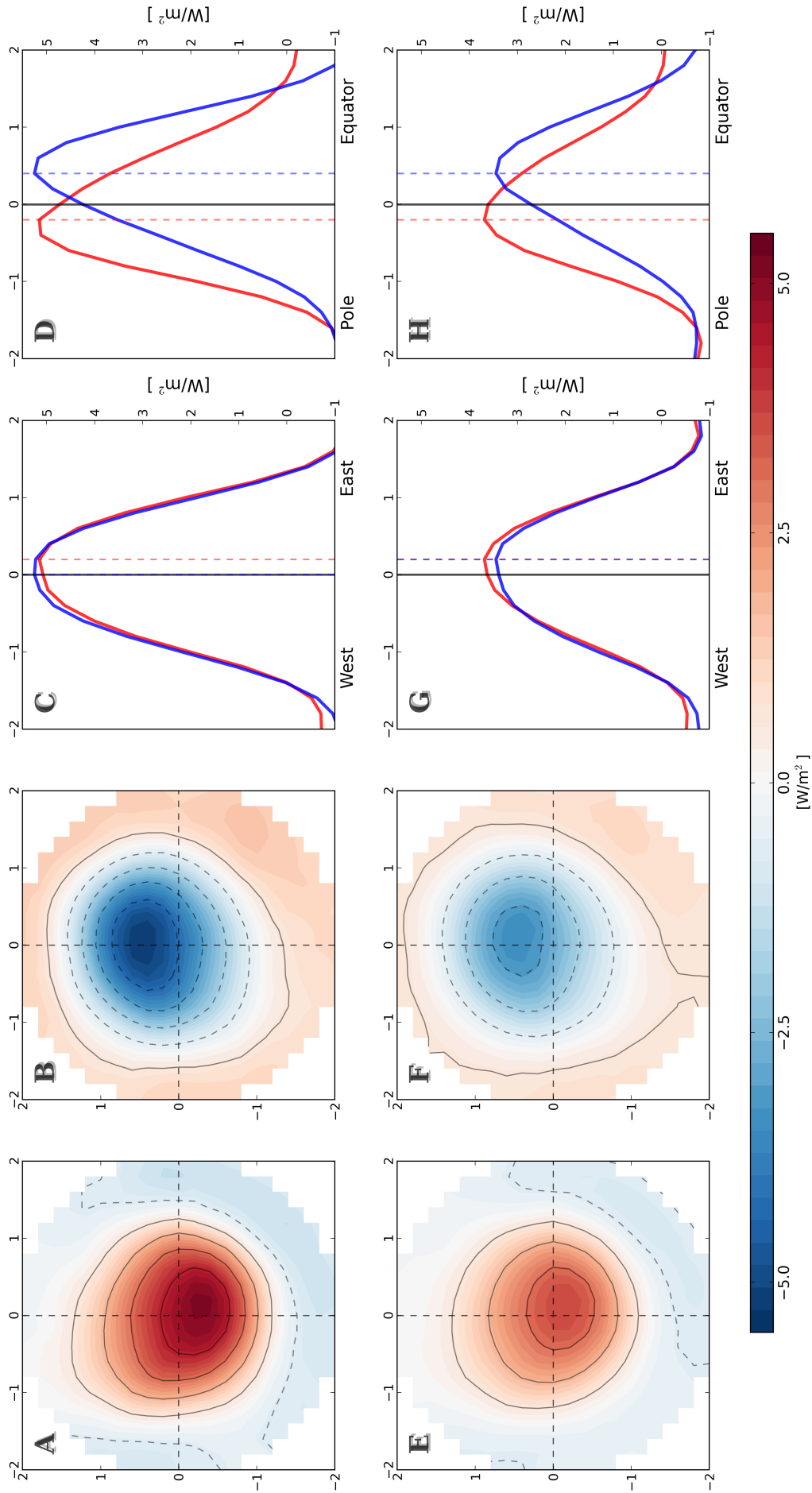


**Figure 32** – Similar to Figure 31, but for eddies with amplitudes in the 90–95<sup>th</sup> percentile range (18.8–27.3 cm). Contour intervals in the composite maps are shown every 1  $\text{W/m}^2$ .

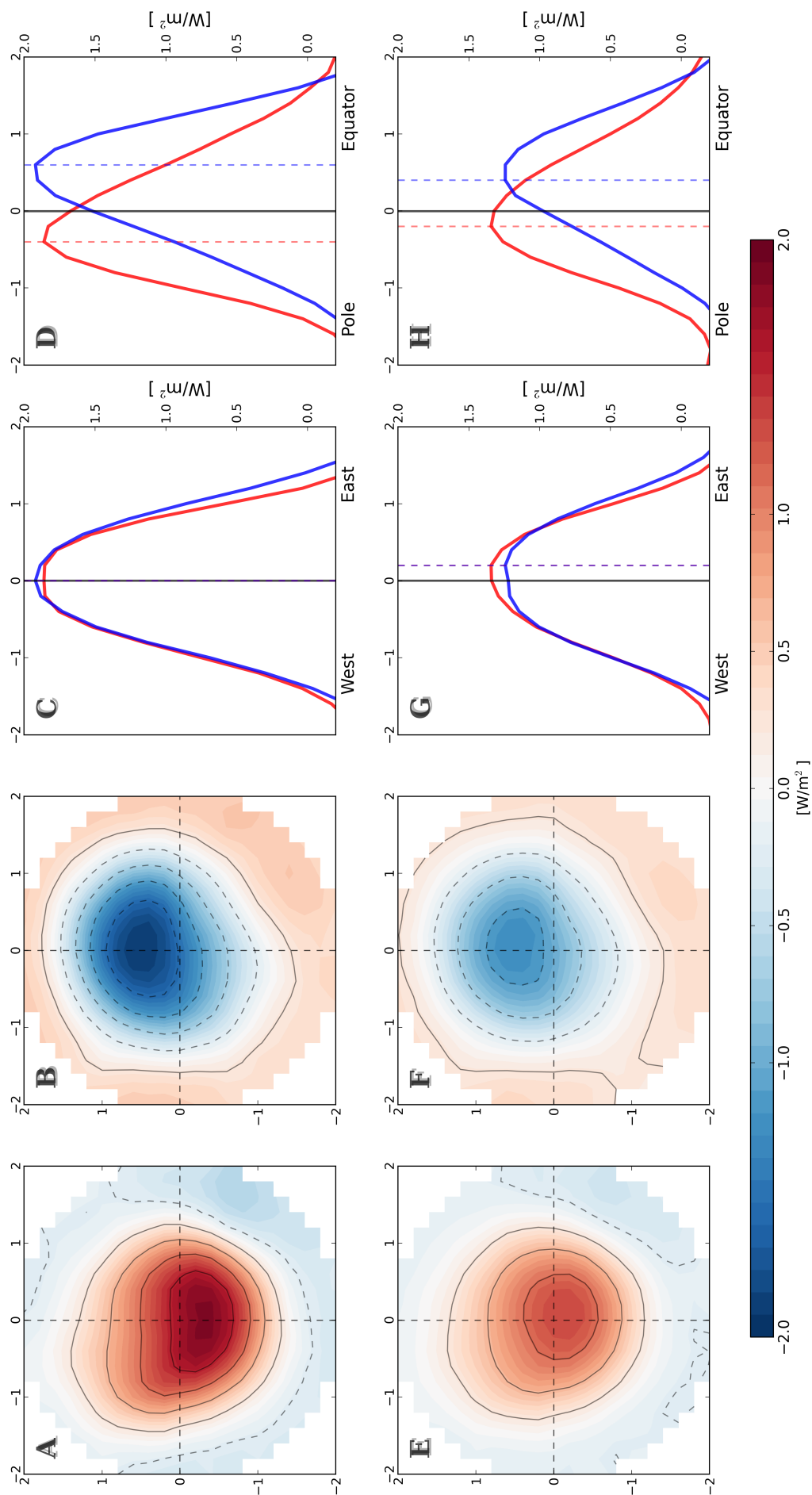


**Figure 33** – Similar to Figure 31, but for eddies with amplitudes between 12.1–18.8 cm, corresponding to  $\sim 8600$  anticyclonic and  $\sim 9000$  cyclonic eddies. Contour intervals in the composite maps are shown every  $0.4 W/m^2$ .

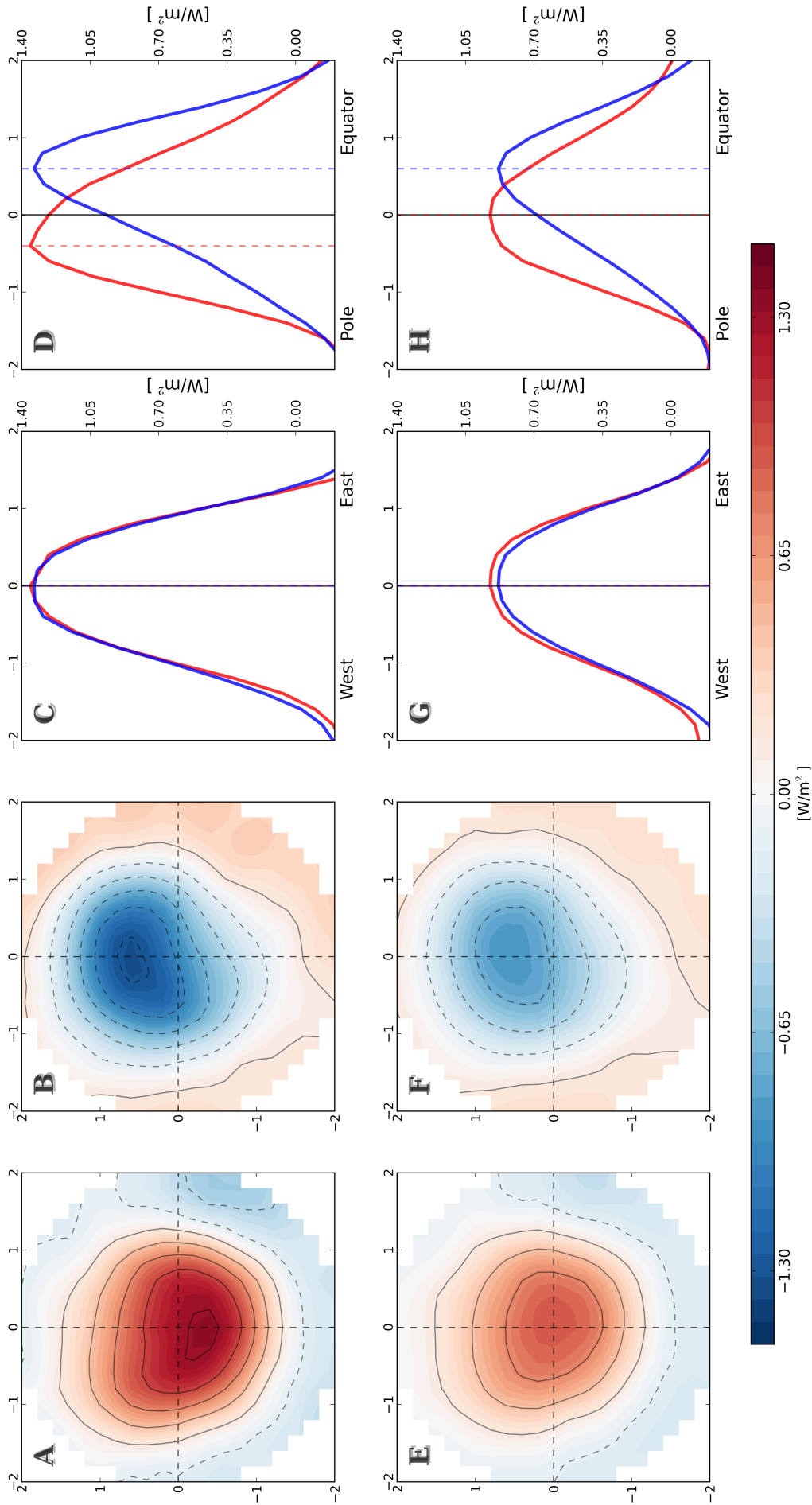
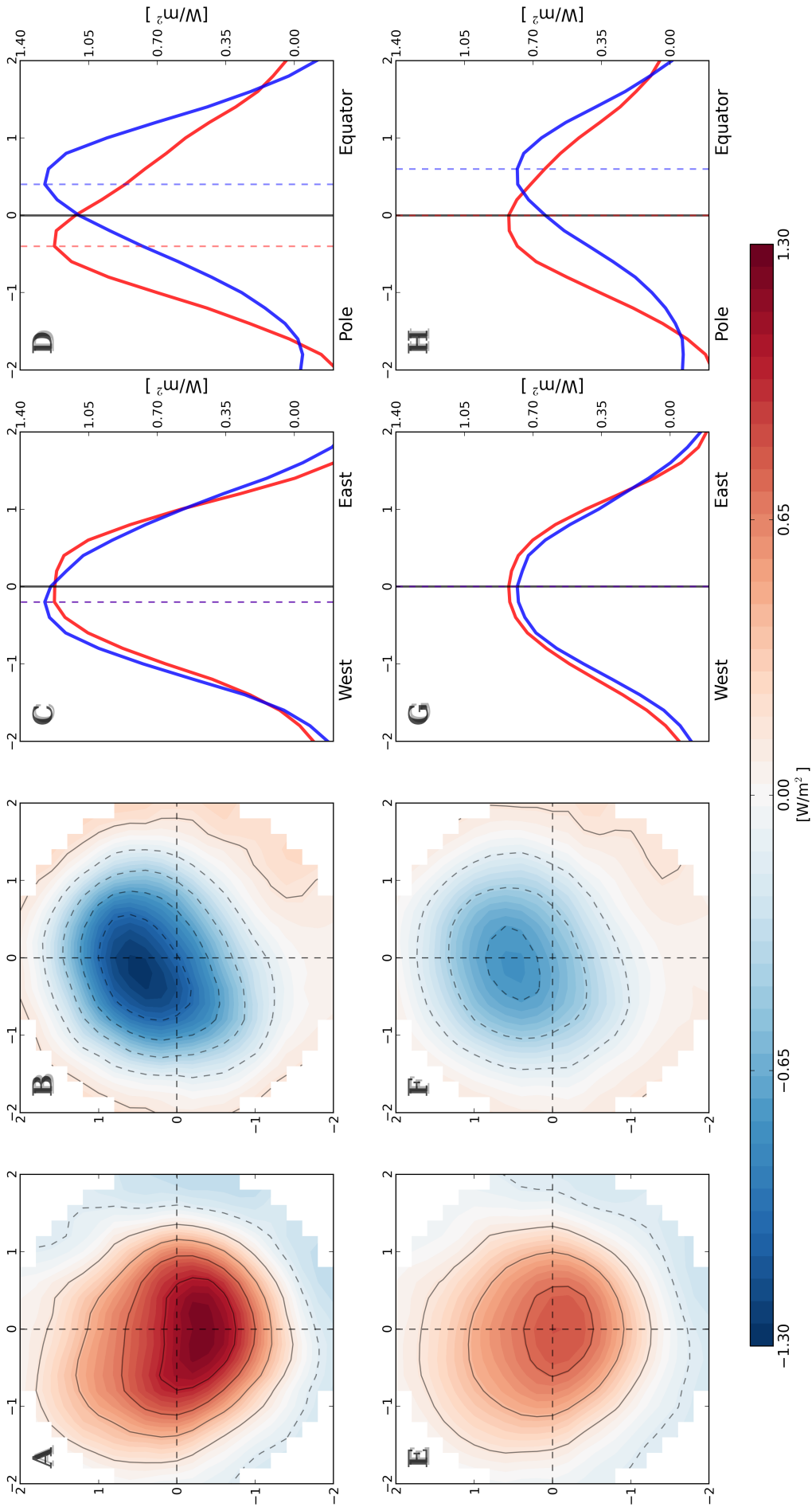
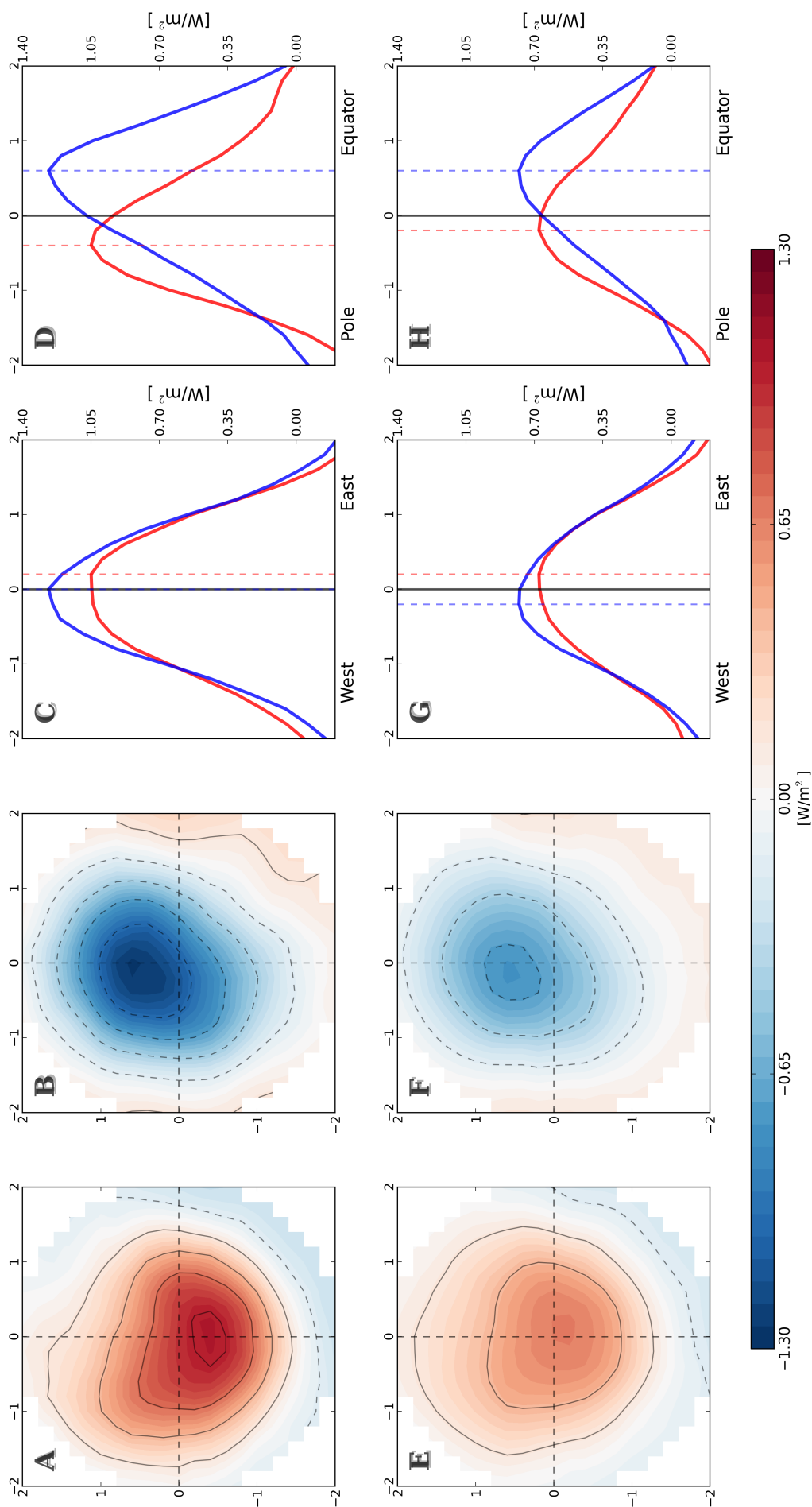


Figure 34 – Similar to Figure 33, but for eddies with amplitudes between 8.9–12.1 cm. Contour intervals in the composite maps are shown every  $0.3 W/m^2$ .



**Figure 35** – Similar to Figure 33, but for eddies with amplitudes between 6.8–8.9 cm. Contour intervals in the composite maps are shown every 0.3  $W/m^2$ .



**Figure 36** – Similar to Figure 33, but for eddies with amplitudes between 5.4–6.8 cm. Contour intervals in the composite maps are shown every 0.3  $W/m^2$ .

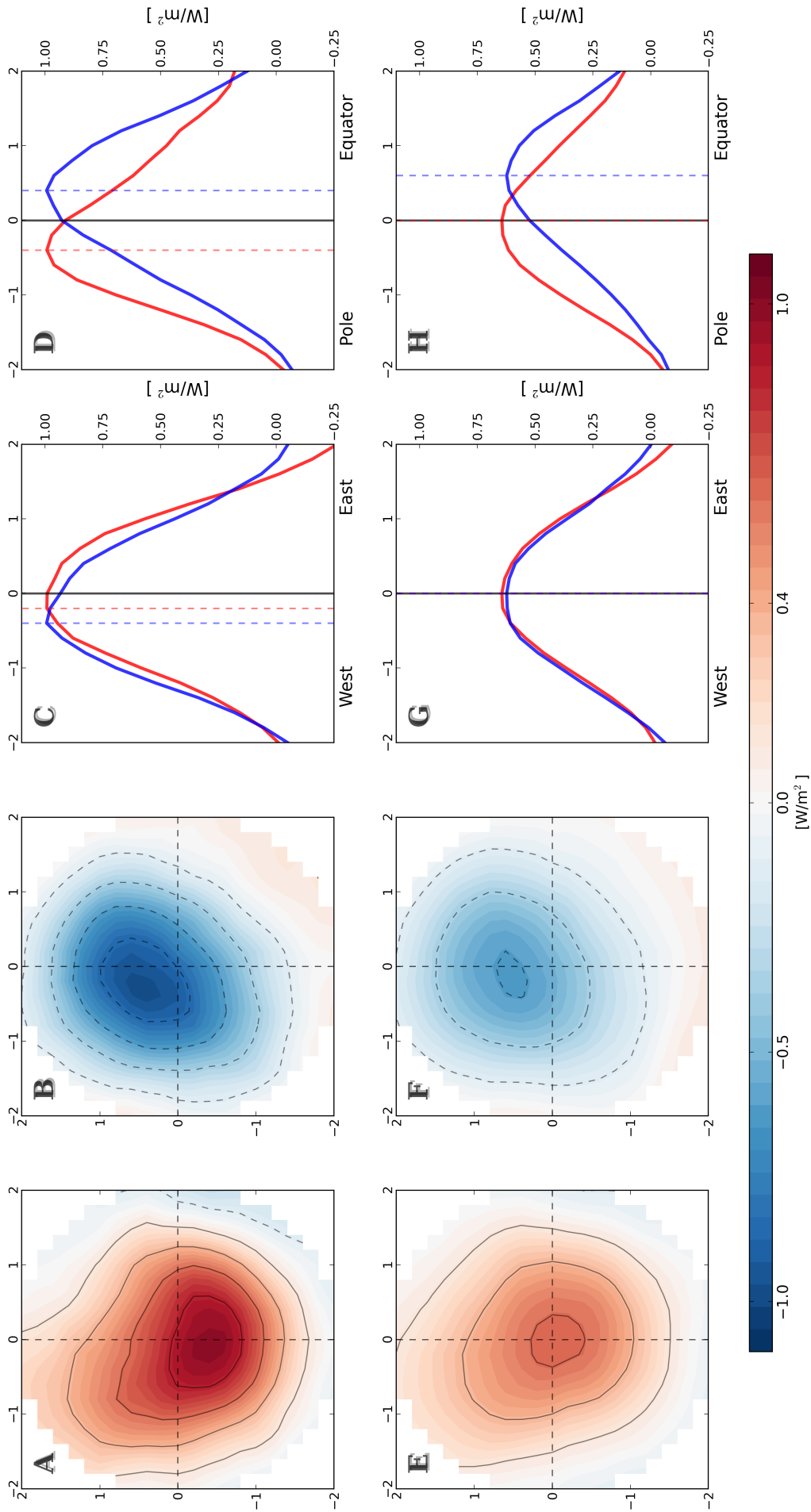


**Figure 37** – Similar to Figure 33, but for eddies with amplitudes between 4.3–5.4cm. Contour intervals in the composite maps are shown every 0.2 W/m<sup>2</sup>.

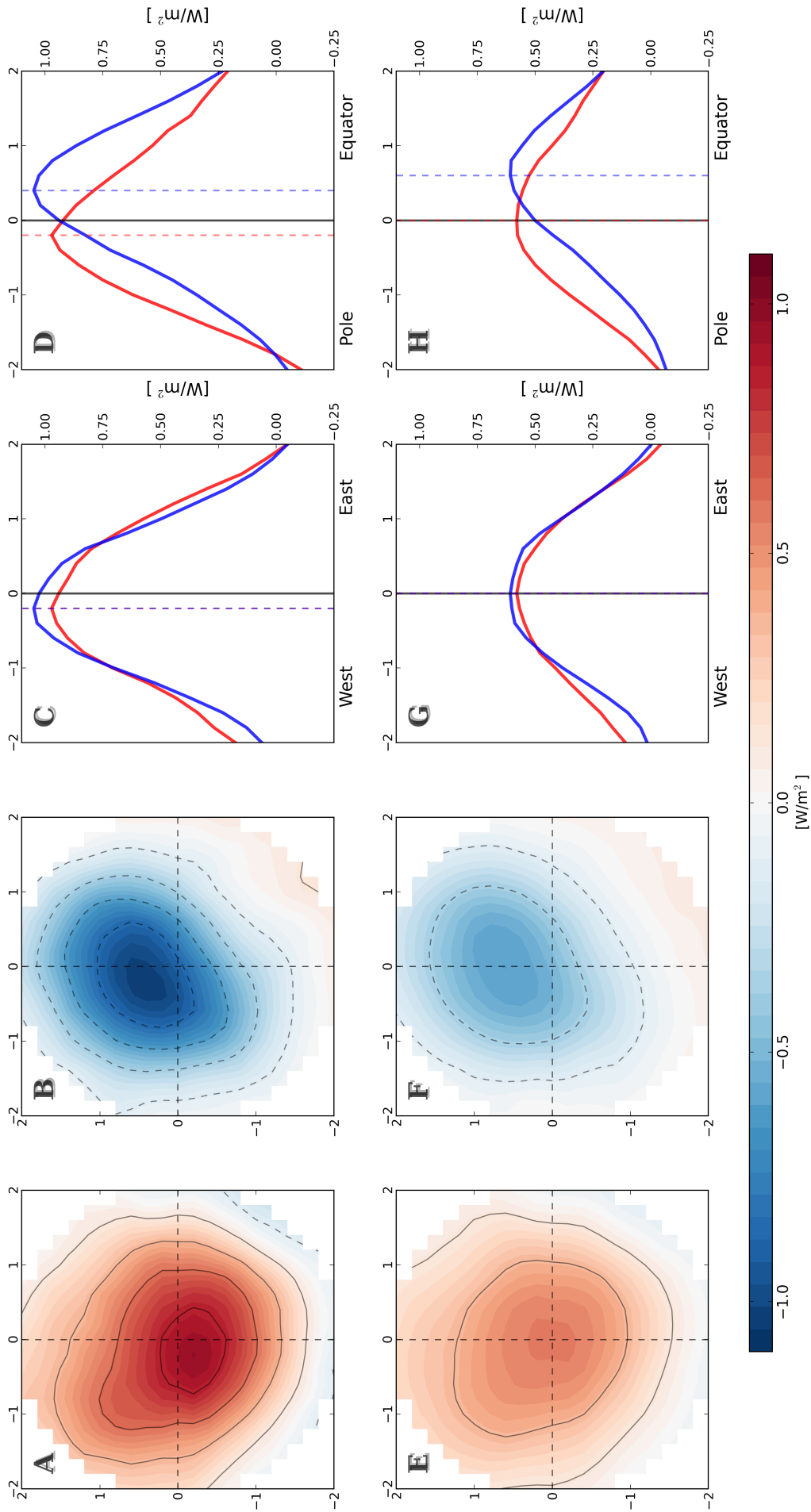


**Figure 38** – Similar to Figure 33, but for eddies with amplitudes between 3.5–4.3 cm. Contour intervals in the composite maps are shown every  $0.2 \text{ W/m}^2$ .

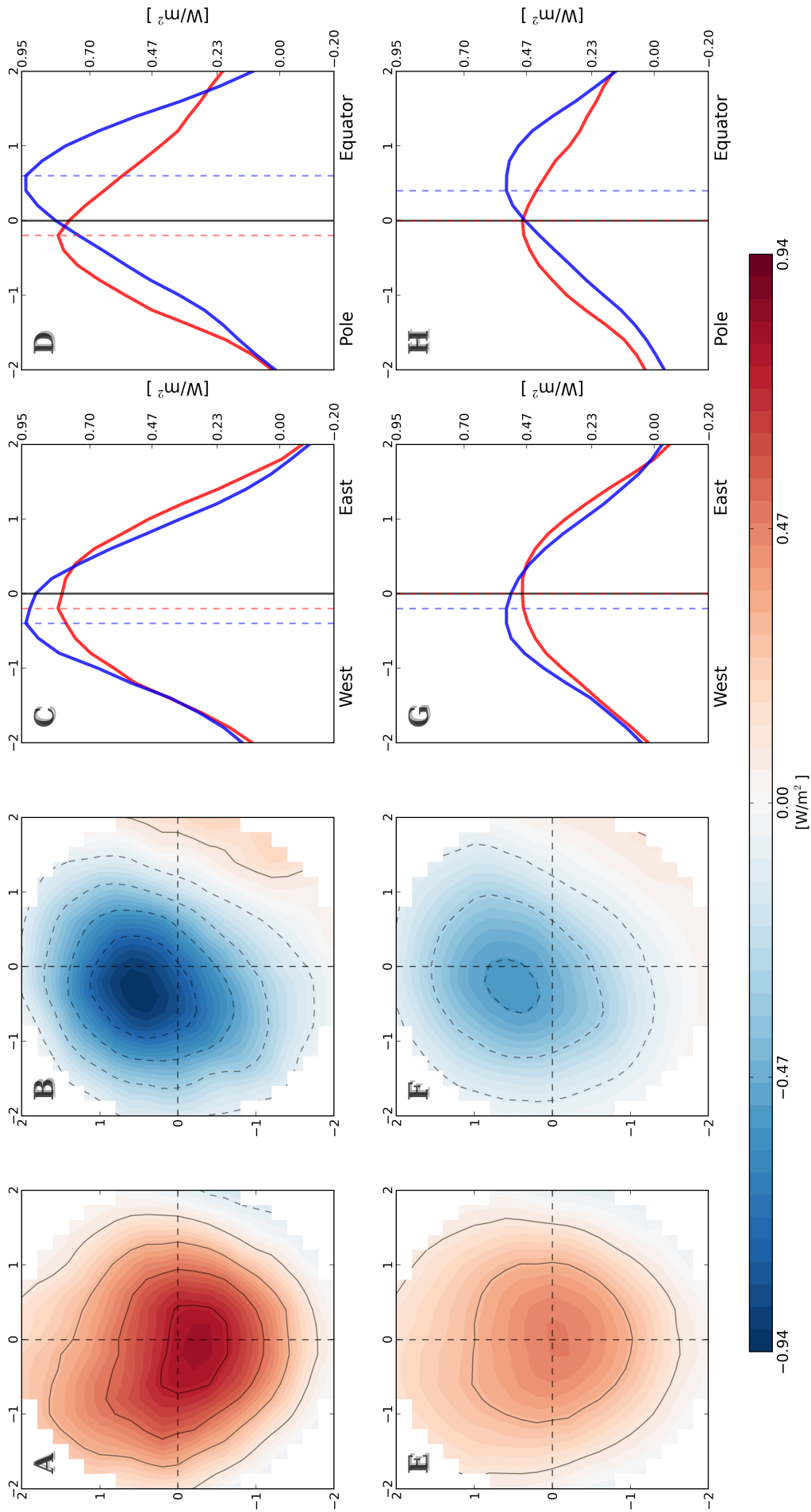


**Figure 39** – Similar to Figure 33, but for eddies with amplitudes between 2.9–3.5 cm. Contour intervals in the composite maps are shown every  $0.2 \text{ W/m}^2$ .

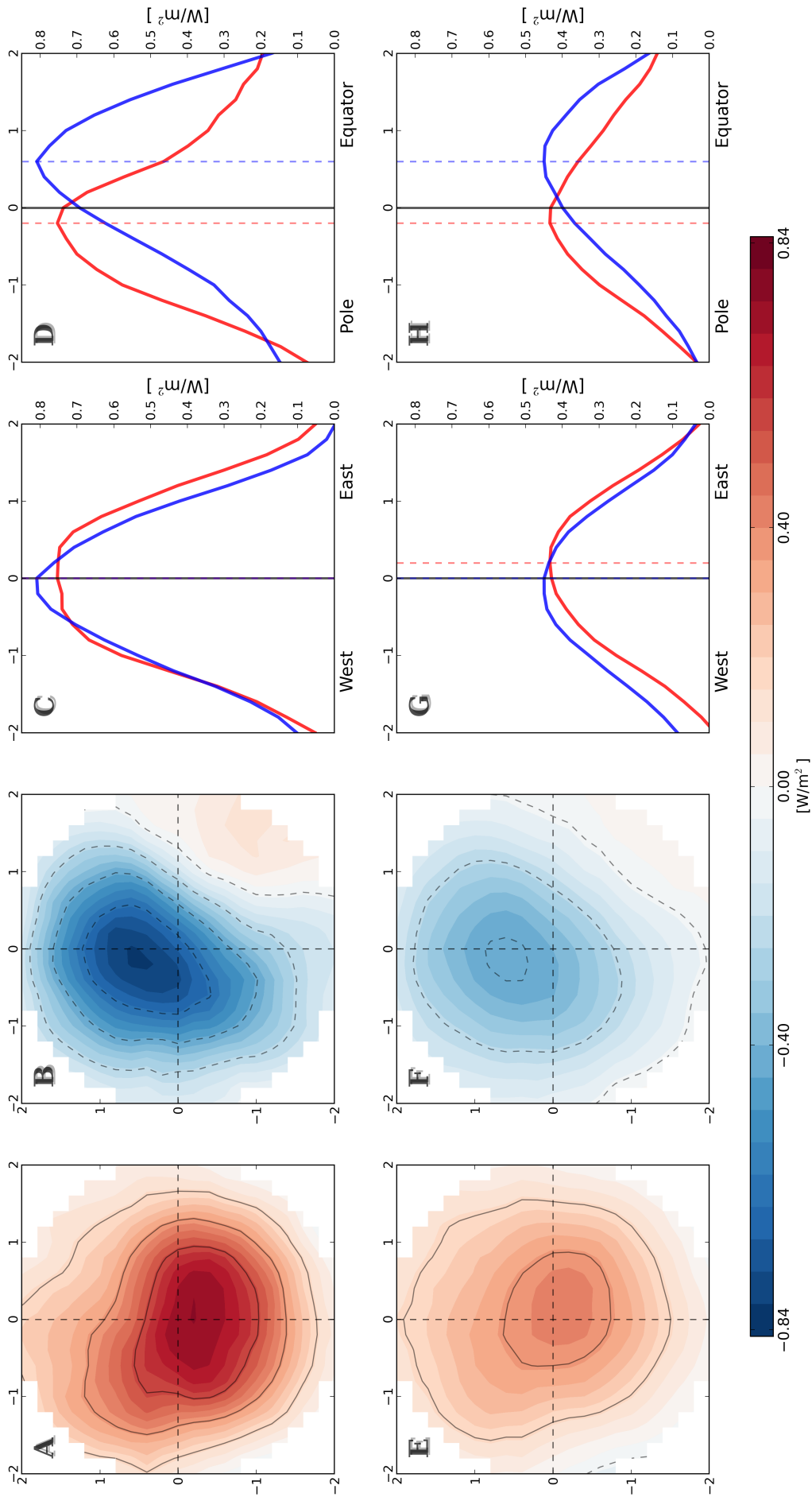


**Figure 40** – Similar to Figure 33, but for eddies with amplitudes between 2.4–2.9 cm. Contour intervals in the composite maps are shown every  $0.2 \text{ W/m}^2$ .

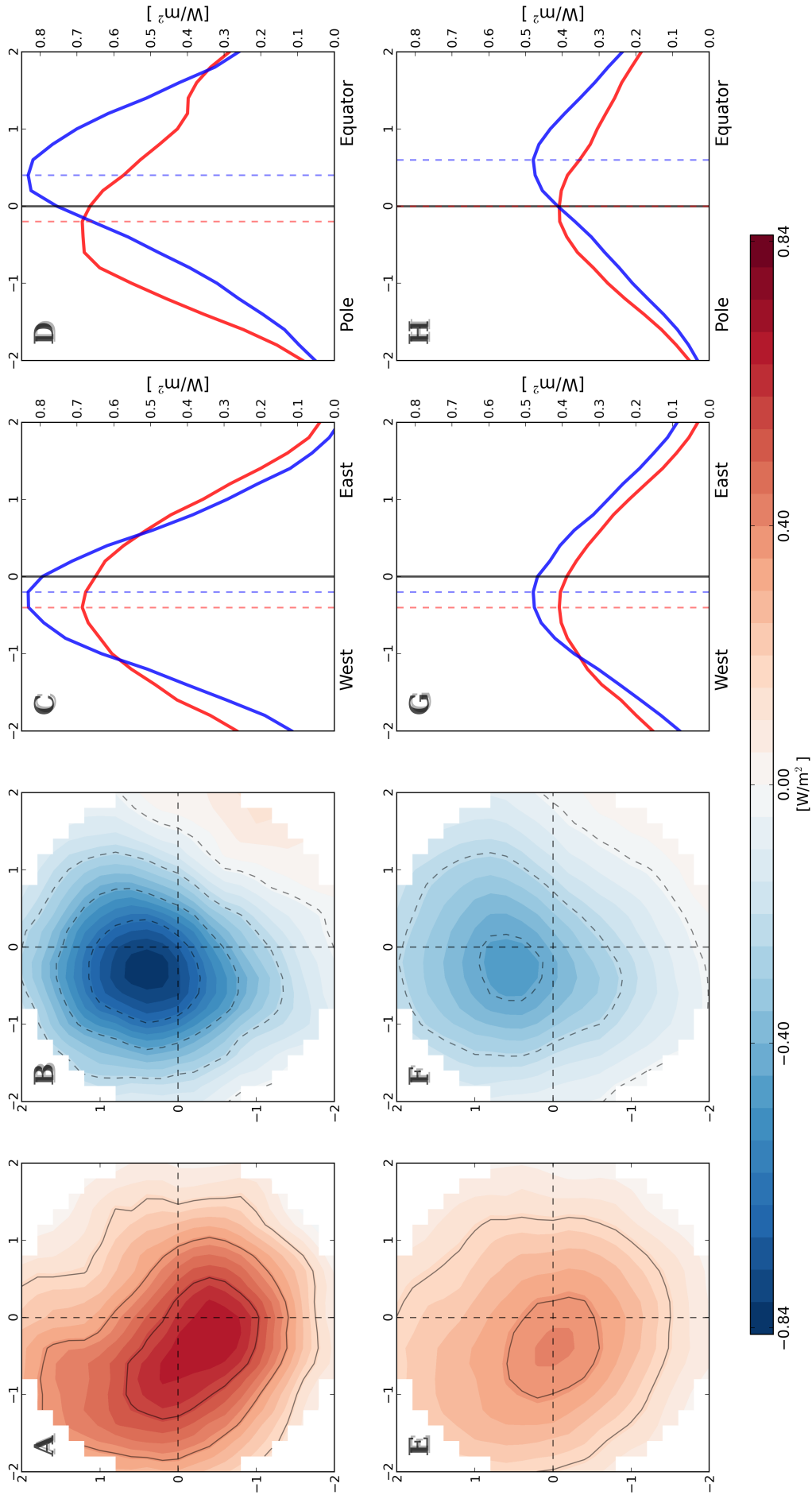


**Figure 41** – Similar to Figure 33, but for eddies with amplitudes between 2.1–2.4 cm. Contour intervals in the composite maps are shown every 0.2  $W/m^2$ .

## 5 Conclusions and Future Work

In this study, by combining 10 years of satellite altimetry and remotely-sensed surface turbulent heat flux estimations, we have provided evidence for the coupling between ocean and atmosphere at mesoscales.

In the first part of this work, we have identified mesoscale eddies from the AVISO SLA maps using the method proposed by Chaigneau *et al.* (2009), which is based on closed contours of SLA. In the most energetic regions of the SA the eddy frequency can reach up to 70%, which makes mesoscale eddies a fundamental part of the local ocean dynamics. Our results for the eddy identification and characterization of the main eddy parameters (such as radius and amplitude) are in very good agreement in comparison with works from other authors, such as Chelton *et al.* (2007), Chelton *et al.* (2011b) and Souza *et al.* (2011b). The importance of having chosen a robust eddy identification method, relies in the fact that it was fundamental to apply a method capable of determining the eddy properties with accuracy in order to guarantee precision in the definition of the turbulent heat fluxes associated with the eddies.

From an Eulerian framework, the mean surface latent and sensible heat flux anomalies caused by mesoscale eddies in the South Atlantic are stronger near the BMC and AGR regions, reaching up to  $\pm 20 \text{ W/m}^2$ . In those regions the mean anomalies can have the same order of magnitude as the large-scale signal, and eddies are capable of explaining up to 29% of the total variance in the surface turbulent heat flux signal. In addition, the averaged heat fluxes inside mesoscale eddies are remarkably distinct from the outside, confirming that eddies are the major contributors for the LHF and SHF variability at mesoscales. The anomalies associated with cyclonic eddies are negative, indicating ocean heat gain, while for anticyclonic eddies are positive, indicating ocean heat loss.

The geographical distribution of such anomalies in the SA are not spatially symmetric for cyclonic and anticyclonic eddies, depending on the distribution of the eddy polarity itself. Thus, regions where cyclonic (anticyclonic) eddies are dominant, there will have a tendency to be marked by ocean heat gain (loss) anomalies. In the BMC regions for examples, such asymmetry generates an area of negative anomalies in northern flank of the confluence, and positive in the southern flank, which should impact, at least locally, the atmospheric circulation. We conclude that in the energetic regions of the SA, eddies can significantly impact the LHF and SHF variability, affecting the heat exchanges at the air-sea interface. These results suggest that air sea interaction at mesoscales, more specifically, the contribution of eddies to the surface heat fluxes, should be taken into account in coupled climate models to improve the accuracy of their predictions.

Composite maps were constructed by averaging the turbulent heat fluxes anomaly distribution inside thousands of eddies in the SA. These maps revealed a well-defined quasi-circular imprint within the eddy interior, with relatively strong turbulent heat fluxes anomalies near the eddy center ( $\pm 10 \text{ W/m}^2$ ) that decays radially outward. Despite since the last few years some studies have been making significant effort to describe the impact of mesoscale eddies on atmospheric parameters (e.g. Hausmann and Czaja (2012), Frenger *et al.* (2013)), we remark that to the present moment, the work presented here is a pioneering study describing the overall impact of mesoscale eddies on the surface turbulent heat fluxes, considering a statistically significant number of eddies. Very recently, Ansorge *et al.* (2014) have used output data from a reanalysis numerical model to estimate the LHF and SHF anomalies over a single anticyclonic eddy in the south-west Indian ocean. The authors found that such eddy had an associated heat flux anomaly of approximately  $8\text{--}10 \text{ W/m}^2$ . These results are very close to ours, however it is important to note that the authors have analyzed a single case, using a product totally based in reanalysis. Thus, we cannot entirely compare the anomalies that they have obtained with our average results.

Moreover, we have found that anomalies within the eddy interiors are not meridionally symmetric in relation to the eddy center: the LHF and SHF peaks in the composite maps for cyclonic eddies are shifted equatorward, while poleward for anticyclonic. The persistence of such meridional asymmetry, regardless the eddy amplitude and location, let us to believe that this shifting is indeed resultant from the dynamics of the eddy itself, what could be explained by the  $\beta$ -effect. Despite of some zonal shifting have also been observed in the composite maps, we were not able to determine whether or not such shifting is significant.

The intensity of the surface heat fluxes anomalies caused by the eddies increase with the eddy amplitude, revealing that large-amplitude eddies have stronger impact on the surface turbulent heat fluxes than small amplitude eddies. As a result, the stronger LHF and SHF anomalies in the SA occur in the energetic regions of the BMC and AGR where large-amplitude eddies are more commonly observed. In addition, the BMC and AGR regions are marked by intense mesoscale activity and generation of mesoscale eddies. The signature of a young eddy on the SST, for example, could be progressively eroded by the surface heat fluxes, that act to minimize the air-sea gradients. Thus, it would be expected stronger LHF and SHF anomalies in regions of eddy genesis. To verify this hypothesis, would require further investigations on the evolution of the surface heat fluxes anomalies along the eddy trajectories.

The LHF and SHF anomalies caused by the eddies are a response of their capability to alter SST, wind, and air specific humidity (YU; WELLER, 2007; FRENGER *et al.*, 2013). Thus, when interacting with the atmosphere, eddies can lose energy by the surface heat fluxes. The effects of this energy exchange could have impact on the eddy decay

and lifetime. We suggest for future work the use of numerical and analytical models to explore the effects of surface heat loss and gain on the eddy dynamics. In addition, owing to the intensity of the heat flux anomalies, eddies could impact beyond the atmospheric boundary layer, having potential implications on the large-scale atmospheric circulation, as previously suggested by Chelton and Xie (2010). For further investigations on this matter, the representation of air–sea interactions at mesoscales in numerical weather prediction models would be necessary in order to quantify how eddies are capable of modifying the overlying atmosphere.

# APPENDIX A – The Okubo–Weiss method

The movement of particles in a Lagrangian framework involving complex flows has always been a subject of great interest for oceanographers. To describe the dispersion in the ocean surface, Okubo (1970) and Weiss (1991), showed by different means that the shapes of particle trajectories and the evolution of the vorticity gradients are governed by the sign of a particular parameter. Considering a two dimensional flow such that  $u$  and  $v$  are the zonal and meridional velocity components and  $(x, y)$  subscripts represent partial derivatives, we can define the Okubo-Weiss parameter ( $W$ ) as:

$$W = (v_x + u_y)^2 + (u_x - v_y)^2 - (v_x - u_y)^2, \quad (\text{A.1})$$

where the first two terms of the right-hand side of the equation represent the normal and shearing strain (associated with the deformation of the flow) and the third one is the relative vorticity (associated with the rotation of the flow). Therefore, the Okubo-Weiss parameter measures the relative importance between deformation and rotation of the flow. Using  $S_s$  and  $S_n$  to represent strain components and  $\zeta$  to represent relative vorticity, we can write equation A.1 on a more compact way:

$$W = S_n^2 + S_s^2 - \zeta^2. \quad (\text{A.2})$$

By concept, strain is associated with deformation and vorticity is associated with rotation, thus the Okubo-Weiss parameter ( $W$ ), weighs the relative importance between deformation and rotation in a flow. Therefore, regions in the flow field where  $W < 0$  are dominated by rotation. In contrast, if  $W > 0$  the flow is dominated by deformation. Based on the principle that an eddy exists where rotation dominates deformation (ISERN-FONTANET *et al.*, 2003; MORROW *et al.*, 2004; CHELTON *et al.*, 2007), eddies can be identified as regions with the same sign of vorticity (either negative for cyclonic eddies or positive for anticyclonic eddies in the southern hemisphere) where the OW parameter is less than a negative threshold value  $W_0$ .

Despite of the fundamentals behind the OW method being relatively simple, the method itself has some intrinsic weaknesses, as recently pointed out by (CHELTON *et al.*, 2011b).

- (i) The identification of eddies by an OW-based method depends on the choice of a threshold value  $W_0$ . Thus, its efficiency can significantly vary from region to region

in the sense that there is no way to choose an optimal value for  $W_0$ . If the threshold is set too low it can give rise to very large false-eddies, even enclosing regions with opposite polarities. In contrast, setting it too high, the search can lead to missing the identification of smaller eddies.

- (ii) Relative to the geostrophic balance in equation 1.7, the OW parameter can be written in terms of  $\eta$  as:

$$W = 4 \frac{g^2}{f_0^2} (\eta_{xy}^2 - \eta_{xx}\eta_{yy}). \quad (\text{A.3})$$

Therefore, the calculation of the OW parameter involves products of second derivatives of the SLA. The noise to signal ratio on the AVISO SLA fields is non-negligible and it could be amplified by each numerical differentiation and multiplication in the computation of  $W$ . Chelton *et al.* (2007) proposed a solution for this problem smoothing both the SLA and the  $W$  field in order to reduce the noise. However, the filtering introduces a negative bias in the amplitude of the eddies and a positive bias in their horizontal scales.

- (iii) Furthermore, in the OW-based method closed contours of  $W$  not always coincide with closed contours of SLA. This discrepancy between the two fields might result in opposite polarities coexisting within a single contour of  $W$ .

Hence, based on the points mentioned above, we conclude that considering noisy SSH, the OW parameter is not the best option to identify mesoscale eddies. As a consequence of the noise amplification, it is strongly recommended to define eddies by a method that eliminates the necessity of differentiation of the SSH/SLA fields (CHELTON *et al.*, 2011b). Being so, we have decided not to use the OW-based method and instead, analyze our data through the threshold-free method proposed by Chaigneau *et al.* (2009), described in Section 3.1.2.

# Bibliography

- ADEM, J. A series solution for the barotropic vorticity equation and its application in the study of atmospheric vortices. *Tellus*, Wiley Online Library, v. 8, n. 3, p. 364–372, 1956.
- ANSORGE, I.; JACKSON, J.; REID, K.; DURGADOO, J.; SWART, S.; EBERENZ, S. Evidence of a southward eddy corridor in the south-west Indian ocean. *Deep Sea Research Part II: Topical Studies in Oceanography*, Elsevier, 2014.
- BALLEGOOYEN, R. C.; GRÜNDLINGH, M. L.; LUTJEHARMS, J. R. Eddy fluxes of heat and salt from the southwest Indian Ocean into the southeast Atlantic Ocean: A case study. *Journal of Geophysical Research: Oceans (1978–2012)*, Wiley Online Library, v. 99, n. C7, p. 14053–14070, 1994.
- BEAL, L. M.; RUIJTER, W. P. D.; BIASTOCH, A.; ZAHN, R. *et al.* On the role of the Agulhas system in ocean circulation and climate. *Nature*, Nature Publishing Group, v. 472, n. 7344, p. 429–436, 2011.
- BENTAMY, A. *New Release of Satellite Turbulent Fluxes 1999–2009*. [S.l.], 2013.
- BENTAMY, A.; AYINA, L.; DRENNAN, W.; KATSAROS, K.; MESTAS-NUÑEZ, A.; PINKER, R. 15 years of ocean surface momentum and heat fluxes from remotely sensed observations. *FLUX NEWS, No. 5, World Climate Research Programme, Geneva, Switzerland, pp.*, p. 14–16, 2008.
- BENTAMY, A.; GRODSKY, S. A.; KATSAROS, K.; MESTAS-NUÑEZ, A. M.; BLANKE, B.; DESBIOLLES, F. Improvement in air–sea flux estimates derived from satellite observations. *International Journal of Remote Sensing*, Taylor & Francis, v. 34, n. 14, p. 5243–5261, 2013.
- BIASTOCH, A.; BÖNING, C. W.; LUTJEHARMS, J. Agulhas leakage dynamics affects decadal variability in Atlantic overturning circulation. *Nature*, Nature Publishing Group, v. 456, n. 7221, p. 489–492, 2008.
- BOEBEL, O.; LUTJEHARMS, J.; SCHMID, C.; ZENK, W.; ROSSBY, T.; BARRON, C. The Cape Cauldron: a regime of turbulent inter-ocean exchange. *Deep Sea Research Part II: Topical Studies in Oceanography*, Elsevier, v. 50, n. 1, p. 57–86, 2003.
- BOURASSA, M. A.; GILLE, S. T.; JACKSON, D. L.; ROBERTS, J. B.; WICK, G. A. Ocean winds and turbulent air-sea fluxes inferred from remote sensing. *Oceanography*, Oceanography Society, v. 23, n. 4, p. 36–51, 2010.
- BYRNE, D. A.; GORDON, A. L.; HAXBY, W. F. Agulhas eddies: A synoptic view using Geosat ERM data. *Journal of Physical Oceanography*, v. 25, n. 5, p. 902–917, 1995.
- CAMPOS, E.; IKEDA, Y.; CASTRO, B.; GAETA, S.; LORENZZETTI, J.; STEVENSON, M. Experiment studies circulation in the Western South Atlantic. *Eos, Transactions American Geophysical Union*, Wiley Online Library, v. 77, n. 27, p. 253–259, 1996.

- CASTELÃO, G. P.; VILLAS BÔAS, A. B.; IRBER JR., L. C. *MAUD: Moving Average for Uneven Data*. 2013. <<https://pypi.python.org/pypi/maud>>.
- CAYAN, D. R. Latent and sensible heat flux anomalies over the northern oceans: Driving the sea surface temperature. *Journal of Physical Oceanography*, v. 22, n. 8, p. 859–881, 1992.
- CHAIGNEAU, A.; ELDIN, G.; DEWITTE, B. Eddy activity in the four major upwelling systems from satellite altimetry (1992–2007). *Progress in Oceanography*, v. 83, n. 1–4, p. 117 – 123, 2009.
- CHAIGNEAU, A.; GIZOLME, A.; GRADOS, C. Mesoscale eddies off Peru in altimeter records: Identification algorithms and eddy spatio-temporal patterns. *Progress in Oceanography*, v. 79, n. 2–4, p. 106 – 119, 2008. ISSN 0079-6611.
- CHAIGNEAU, A.; TEXIER, M. L.; ELDIN, G.; GRADOS, C.; PIZARRO, O. Vertical structure of mesoscale eddies in the eastern South Pacific Ocean: A composite analysis from altimetry and argo profiling floats. *Journal of Geophysical Research: Oceans*, v. 116, n. C11, 2011. ISSN 2156-2202.
- CHELTON, D. B.; DESZOEKE, R. A.; SCHLAX, M. G.; NAGGAR, K. E.; SIWERTZ, N. Geographical variability of the first baroclinic Rossby radius of deformation. *Journal of Physical Oceanography*, v. 28, n. 3, p. 433–460, 1998.
- CHELTON, D. B.; GAUBE, P.; SCHLAX, M. G.; EARLY, J. J.; SAMELSON, R. M. The influence of nonlinear mesoscale eddies on near-surface oceanic chlorophyll. *Science*, American Association for the Advancement of Science, v. 334, n. 6054, p. 328–332, 2011.
- CHELTON, D. B.; SCHLAX, M. G.; SAMELSON, R. M. Global observations of nonlinear mesoscale eddies. *Progress in Oceanography*, v. 91, p. 167–216, 2011.
- CHELTON, D. B.; SCHLAX, M. G.; SAMELSON, R. M.; SZOEKE, R. A. de. Global observations of large oceanic eddies. *Geophysical Research Letters*, v. 34, n. 15, p. n/a–n/a, 2007. ISSN 1944-8007.
- CHELTON, D. B.; SCHLAX, M. G.; WITTER, D. L.; RICHMAN, J. G. Geosat altimeter observations of the surface circulation of the Southern Ocean. *Journal of Geophysical Research: Oceans (1978–2012)*, Wiley Online Library, v. 95, n. C10, p. 17877–17903, 1990.
- CHELTON, D. B.; XIE, S.-P. Coupled ocean-atmosphere interaction at oceanic mesoscales. *Oceanography*, Oceanography Society, v. 23, n. 4, p. 52–69, 2010.
- CHOI, S. C. *Introductory Applied Statistics in Science*. Prentice Hall, 1978. ISBN 9780135016190. Disponível em: <<http://amazon.com/o/ASIN/0135016193/>>.
- CHOU, S.-H.; NELKIN, E.; ARDIZZONE, J.; ATLAS, R. M. A comparison of latent heat fluxes over global oceans for four flux products. *Journal of climate*, v. 17, n. 20, p. 3973–3989, 2004.
- COLAS, F.; MCWILLIAMS, J. C.; CAPET, X.; KURIAN, J. Heat balance and eddies in the Peru-Chile current system. *Climate dynamics*, Springer, v. 39, n. 1-2, p. 509–529, 2012.

- DEWAR, W. K.; FLIERL, G. R. Some effects of the wind on rings. *Journal of physical oceanography*, v. 17, n. 10, p. 1653–1667, 1987.
- DIBARBOURE, G.; LAURET, O.; MERTZ, F.; ROSMORDUC, V.; MAHEU, C. SSALTO/DUACS user handbook:(M) SLA and (M) ADT near-real time and delayed time products. *Rep. CLS-DOS-NT*, v. 6, p. 39, 2008.
- DUCET, N.; TRAON, P.-Y. L.; REVERDIN, G. Global high-resolution mapping of ocean circulation from TOPEX/Poseidon and ERS-1 and-2. *Journal of Geophysical Research: Oceans (1978–2012)*, Wiley Online Library, v. 105, n. C8, p. 19477–19498, 2000.
- DUNCAN, C. An eddy in the subtropical convergence southwest of South Africa. *Journal of Geophysical Research*, Wiley Online Library, v. 73, n. 2, p. 531–534, 1968.
- EARLY, J. J.; SAMELSON, R.; CHELTON, D. B. The evolution and propagation of quasigeostrophic ocean eddies\*. *Journal of Physical Oceanography*, v. 41, n. 8, p. 1535–1555, 2011.
- EMERY, W. J.; THOMSON, R. E. *Data analysis methods in physical oceanography*. 2nd ed. [S.l.]: Elsevier, 2001.
- FAIRALL, C.; BRADLEY, E. F.; HARE, J.; GRACHEV, A.; EDSON, J. Bulk parameterization of air-sea fluxes: Updates and verification for the COARE algorithm. *Journal of Climate*, v. 16, n. 4, p. 571–591, 2003.
- FEDOROV, A. V. Ocean–atmosphere coupling. *The Oxford Companion to Global Change*, p. 369–374, 2008.
- FIRING, E.; BEARDSLEY, R. C. The behavior of a barotropic eddy on a  $\beta$ -plane. *Journal of Physical Oceanography*, v. 6, n. 1, p. 57–65, 1976.
- FLIERL, G. R. Rossby wave radiation from a strongly nonlinear warm eddy. *Journal of Physical Oceanography*, v. 14, n. 1, p. 47–58, 1984.
- FRENGER, I.; GRUBER, N.; KNUTTI, R.; MÜNNICH, M. Imprint of Southern Ocean eddies on winds, clouds and rainfall. *Nature Geoscience*, Nature Publishing Group, v. 6, n. 8, p. 608–612, 2013.
- FU, L.-L.; CHELTON, D. B.; TRAON, P.-Y. L.; MORROW, R. Eddy dynamics from satellite altimetry. *Oceanography*, Oceanography Society, v. 23, n. 4, p. 14–25, 2010.
- FU, L. L.; TRAON, P.-Y. L. Satellite altimetry and ocean dynamics. *Comptes Rendus Geoscience*, Elsevier, v. 338, n. 14, p. 1063–1076, 2006.
- FUGLISTER, F. C. *Cyclonic rings formed by the Gulf Stream 1965-66*. [S.l.]: Woods Hole Oceanographic Institution, 1972.
- GARCIA, C. A.; SARMA, Y.; MATA, M. M.; GARCIA, V. M. Chlorophyll variability and eddies in the Brazil–Malvinas Confluence region. *Deep Sea Research Part II: Topical Studies in Oceanography*, Elsevier, v. 51, n. 1, p. 159–172, 2004.
- GARZOLI, S. L. Geostrophic velocity and transport variability in the Brazil–Malvinas Confluence. *Deep Sea Research Part I: Oceanographic Research Papers*, Elsevier, v. 40, n. 7, p. 1379–1403, 1993.

GARZOLI, S. L.; BARINGER, M. O.; DONG, S.; PEREZ, R. C.; YAO, Q. South Atlantic meridional fluxes. *Deep Sea Research Part I: Oceanographic Research Papers*, Elsevier, v. 71, p. 21–32, 2013.

GARZOLI, S. L.; GARRAFFO, Z. Transports, frontal motions and eddies at the Brazil-Malvinas Currents Confluence. *Deep Sea Research Part A. Oceanographic Research Papers*, Elsevier, v. 36, n. 5, p. 681–703, 1989.

GARZOLI, S. L.; MATANO, R. The South Atlantic and the Atlantic meridional overturning circulation. *Deep Sea Research Part II: Topical Studies in Oceanography*, Elsevier, v. 58, n. 17, p. 1837–1847, 2011.

GARZOLI, S. L.; RICHARDSON, P. L.; RAE, D.; CHRISTOPHER, M.; FRATANTONI, D. M.; GOÑI, G. J.; ROUBICEK, A. J. Three Agulhas rings observed during the Benguela Current experiment. *Journal of Geophysical Research: Oceans (1978–2012)*, Wiley Online Library, v. 104, n. C9, p. 20971–20985, 1999.

GAUBE, P.; CHELTON, D.; STRUTTON, P.; BEHRENFELD, M. Satellite observations of chlorophyll, phytoplankton biomass, and Ekman pumping in nonlinear mesoscale eddies. *Journal of Geophysical Research: Oceans*, Wiley Online Library, 2013.

GILL, A. E. *Atmosphere-Ocean Dynamics*. 1. ed. [S.l.]: Academic Press, 1982. ISBN 9780122835223.

GONI, G.; KAMHOLZ, S.; GARZOLI, S.; OLSON, D. Dynamics of the Brazil-Malvinas Confluence based on inverted echo sounders and altimetry. *Journal of Geophysical Research: Oceans (1978–2012)*, Wiley Online Library, v. 101, n. C7, p. 16273–16289, 1996.

GONI, G. J.; GARZOLI, S. L.; ROUBICEK, A. J.; OLSON, D. B.; BROWN, O. B. Agulhas ring dynamics from TOPEX/POSEIDON satellite altimeter data. *Journal of Marine Research*, Sears Foundation for Marine Research, v. 55, n. 5, p. 861–883, 1997.

GORDON, A. L. Brazil-Malvinas Confluence–1984. *Deep Sea Research Part A. Oceanographic Research Papers*, Elsevier, v. 36, n. 3, p. 359–384, 1989.

GORDON, A. L.; HAXBY, W. F. Agulhas eddies invade the South Atlantic: Evidence from Geosat altimeter and shipboard conductivity-temperature-depth survey. *Journal of Geophysical Research: Oceans (1978–2012)*, Wiley Online Library, v. 95, n. C3, p. 3117–3125, 1990.

GULEV, S. K.; BELYAEV, K. Probability distribution characteristics for surface air-sea turbulent heat fluxes over the global ocean. *Journal of Climate*, v. 25, n. 1, p. 184–206, 2012.

HAUSMANN, U.; CZAJA, A. The observed signature of mesoscale eddies in sea surface temperature and the associated heat transport. *Deep Sea Research Part I: Oceanographic Research Papers*, Elsevier, 2012.

HOLTE, J.; STRANEO, F.; MOFFAT, C.; WELLER, R.; FARRAR, J. T. Structure and surface properties of eddies in the southeast Pacific Ocean. *Journal of Geophysical Research: Oceans*, Wiley Online Library, v. 118, n. 5, p. 2295–2309, 2013.

- ISERN-FONTANET, J.; GARCÍA-LADONA, E.; FONT, J. Identification of marine eddies from altimetric maps. *Journal of Atmospheric and Oceanic Technology*, v. 20, n. 5, p. 772–778, 2003.
- KUBOTA, M.; IWASAKA, N.; KIZU, S.; KONDA, M.; KUTSUWADA, K. Japanese ocean flux data sets with use of remote sensing observations (J-OFURO). *Journal of Oceanography*, Springer, v. 58, n. 1, p. 213–225, 2002.
- KURCZYN, J. A.; BEIER, E.; LAVÍN, M. F.; CHAIGNEAU, A. Mesoscale eddies in the northeastern Pacific tropical-subtropical transition zone: Statistical characterization from satellite altimetry. *Journal of Geophysical Research: Oceans*, v. 117, n. C10, 2012. ISSN 2156-2202.
- LARGE, W.; YEAGER, S. The global climatology of an interannually varying air–sea flux data set. *Climate Dynamics*, Springer, v. 33, n. 2-3, p. 341–364, 2009.
- LEGECKIS, R.; GORDON, A. L. Satellite observations of the Brazil and Falkland currents—1975 1976 and 1978. *Deep Sea Research Part A. Oceanographic Research Papers*, Elsevier, v. 29, n. 3, p. 375–401, 1982.
- LENTINI, C. A.; OLSON, D. B.; PODESTÁ, G. P. Statistics of Brazil Current rings observed from AVHRR: 1993 to 1998. *Geophysical Research Letters*, v. 29, n. 16, p. 58–1, 2002.
- LIU, J.; CURRY, J. A. Variability of the tropical and subtropical ocean surface latent heat flux during 1989–2000. *Geophysical Research Letters*, v. 33, n. 5, 2006.
- LIU, W. T. Progress in scatterometer application. *Journal of Oceanography*, Springer, v. 58, n. 1, p. 121–136, 2002.
- LIU, W. T.; KATSAROS, K. B.; BUSINGER, J. A. Bulk parameterization of air-sea exchanges of heat and water vapor including the molecular constraints at the interface. *Journal of the Atmospheric Sciences*, v. 36, n. 9, p. 1722–1735, 1979.
- MCWILLIAMS, J. C.; FLIERL, G. R. On the evolution of isolated, nonlinear vortices. *Journal of Physical Oceanography*, v. 9, n. 6, p. 1155–1182, 1979.
- MILLS, E. Discovery, George Deacon and the hydrology of the Southern Ocean. *Ocean Challenge*, v. 13, n. 3, p. 23 – 29, 2004.
- MORROW, R.; BIROL, F.; GRIFFIN, D.; SUDRE, J. Divergent pathways of cyclonic and anti-cyclonic ocean eddies. *Geophysical Research Letters*, v. 31, p. doi: 10.1029/2004GL020974, 2004.
- MORROW, R.; TRAON, P.-Y. L. 15 years of satellite altimetry and mesoscale ocean dynamics. In: *Proc. ESA Int. Workshop Paper*. [S.l.: s.n.], 2006. v. 889, p. 1585–1588.
- MUNK, W. H. On the wind-driven ocean circulation. *Journal of Meteorology*, v. 7, n. 2, p. 80–93, 1950.
- NEIMAN, P. J.; SHAPIRO, M. The life cycle of an extratropical marine cyclone. Part I: Frontal-cyclone evolution and thermodynamic air-sea interaction. *Monthly weather review*, v. 121, n. 8, p. 2153–2176, 1993.

NENCIOLI, F.; DONG, C.; DICKEY, T.; WASHBURN, L.; MCWILLIAMS, J. C. A vector geometry-based eddy detection algorithm and its application to a high-resolution numerical model product and high-frequency radar surface velocities in the Southern California Bight. *Journal of Atmospheric and Oceanic Technology*, v. 27, p. 564–579, 2010.

OKUBO, A. Horizontal dispersion of floatable particles in the vicinity of velocity singularities such as convergence. *Deep Sea Res.*, v. 17, p. 445–454, 1970.

OLSON, D. B. Rings in the ocean. *Annual Review of Earth and Planetary Sciences*, v. 19, p. 283, 1991.

OLSON, D. B.; EVANS, R. H. Rings of the Agulhas Current. *Deep Sea Research Part A. Oceanographic Research Papers*, Elsevier, v. 33, n. 1, p. 27–42, 1986.

OLSON, D. B.; PODESTÁ, G. P.; EVANS, R. H.; BROWN, O. B. Temporal variations in the separation of Brazil and Malvinas Currents. *Deep Sea Research Part A. Oceanographic Research Papers*, Elsevier, v. 35, n. 12, p. 1971–1990, 1988.

PEDLOSKY, J. *Geophysical Fluid Dynamics*. 2nd. ed. [S.l.]: Springer, 1987. ISBN 9780387963877.

PETERSON, R. G.; STRAMMA, L. Upper-level circulation in the South Atlantic Ocean. *Progress in Oceanography*, Elsevier, v. 26, n. 1, p. 1–73, 1991.

PICHEVIN, T.; NOF, D.; LUTJEHARMS, J. Why are there Agulhas rings? *Journal of physical oceanography*, v. 29, n. 4, p. 693–707, 1999.

PIOLA, A.; MATANO, R. Brazil and Falklands (Malvinas) currents. *Ocean Currents: A Derivative of the Encyclopedia of Ocean Sciences*, p. 35–43, 2001.

POND, S. Air-sea interaction. *Eos, Transactions American Geophysical Union*, Wiley Online Library, v. 52, n. 6, p. IUGG389–IUGG394, 1971.

RAE, C.; GARZOLI, S.; GORDON, A. The eddy field of the southeast Atlantic Ocean: A statistical census from the Benguela Sources and Transports Project. *Journal of Geophysical Research: Oceans (1978–2012)*, Wiley Online Library, v. 101, n. C5, p. 11949–11964, 1996.

RASMUSSEN, E. M.; CARPENTER, T. H. Variations in tropical sea surface temperature and surface wind fields associated with the Southern Oscillation/El Niño. *Monthly Weather Review*, v. 110, n. 5, p. 354–384, 1982.

REYNOLDS, R. W.; SMITH, T. M.; LIU, C.; CHELTON, D. B.; CASEY, K. S.; SCHLAX, M. G. Daily high-resolution-blended analyses for sea surface temperature. *Journal of Climate*, v. 20, n. 22, 2007.

ROBINSON, A. R. *Eddies in marine science*. 4th. ed. Berlin: Springer-Verlag, 1983. 609pp p.

ROBINSON, I. S. *Discovering the ocean from space: The unique applications of satellite oceanography*. [S.l.]: Springer, 2010.

SARACENO, M.; PROVOST, C. On eddy polarity distribution in the Southwestern Atlantic. *Deep Sea Research Part I: Oceanographic Research Papers*, v. 69, n. 0, p. 62 – 69, 2012. ISSN 0967-0637.

SARACENO, M.; PROVOST, C.; PIOLA, A. R.; BAVA, J.; GAGLIARDINI, A. Brazil Malvinas Frontal System as seen from 9 years of advanced very high resolution radiometer data. *Journal of Geophysical Research: Oceans (1978–2012)*, v. 109, n. C5, 2004.

SCHONTEN, M. W.; RUIJTER, W. P.; LEEUWEN, P. J.; LUTJEHARMS, J. R. Translation, decay and splitting of Agulhas rings in the Southeastern Atlantic Ocean. *Journal of Geophysical Research: Oceans (1978–2012)*, Wiley Online Library, v. 105, n. C9, p. 21913–21925, 2000.

SEBILLE, E. van; LEEUWEN, P. J. V.; BIASTOCH, A.; RUIJTER, W. P. de. On the fast decay of Agulhas rings. *Journal of Geophysical Research: Oceans (1978–2012)*, v. 115, n. C3, 2010.

SILVEIRA, I. C. da; MIRANDA, L. B.; BROWN, W. S. On the origins of the North Brazil Current. *Journal of Geophysical Research: Oceans (1978–2012)*, Wiley Online Library, v. 99, n. C11, p. 22501–22512, 1994.

SMITH, S. W. Moving average filters. In: *The scientist and engineer's guide to digital signal processing*. [S.l.]: California Technical Pub. San Diego, 1997. p. 277–284.

SONG, Q.; CHELTON, D. B.; ESBENSEN, S. K.; THUM, N.; O'NEILL, L. W. Coupling between sea surface temperature and low-level winds in mesoscale numerical models. *Journal of Climate*, v. 22, n. 1, 2009.

SOUZA, J.; MONTÉGUT, C. de B.; CABANES, C.; KLEIN, P. Estimation of the Agulhas ring impacts on meridional heat fluxes and transport using ARGO floats and satellite data. *Geophysical Research Letters*, v. 38, n. 21, 2011.

SOUZA, J. M. A. C.; MONTÉGUT, C. d. B.; TRAON, P. L. Comparison between three implementations of automatic identification algorithms for the quantification and characterization of mesoscale eddies in the South Atlantic Ocean. *Ocean Science*, Copernicus Publications, v. 7, p. 317–334, 2011.

SOUZA, R. B. de; MATA, M. M.; GARCIA, C. A.; KAMPEL, M.; OLIVEIRA, E. N.; LORENZZETTI, J. A. Multi-sensor satellite and in situ measurements of a warm core ocean eddy south of the Brazil–Malvinas Confluence region. *Remote sensing of environment*, Elsevier, v. 100, n. 1, p. 52–66, 2006.

STOMMEL, H. The westward intensification of wind-driven ocean currents. *Trans. Amer. Geophys. Union*, v. 29, n. 2, p. 202–206, 1948.

STRAMMA, L.; PETERSON, R. G. The South Atlantic Current. *Journal of Physical Oceanography*, v. 20, n. 6, p. 846–859, 1990.

SVERDRUP, H. U. Wind-driven currents in a baroclinic ocean; with application to the equatorial currents of the eastern Pacific. *Proceedings of the National Academy of Sciences of the United States of America*, National Academy of Sciences, v. 33, n. 11, p. 318, 1947.

TALLEY, L. D.; PICKARD, G. L.; EMERY, W. J.; SWIFT, J. H. *Descriptive physical oceanography: an introduction*. [S.l.]: Academic Press, 2011.

TRAON, P. L.; FAUGÈRE, Y.; HERNANDEZ, F.; DORANDEU, J.; MERTZ, F.; ABLAIN, M. Can we merge GEOSAT Follow-On with TOPEX/Poseidon and ERS-2 for an improved description of the ocean circulation? *Journal of Atmospheric and Oceanic Technology*, v. 20, n. 6, p. 889–895, 2003.

TRENBERTH, K. E.; FASULLO, J. T.; KIEHL, J. Earth's global energy budget. *Bulletin of the American Meteorological Society*, v. 90, n. 3, 2009.

WEARE, B. C. Interannual moisture variations near the surface of the tropical Pacific Ocean. *Quarterly Journal of the Royal Meteorological Society*, Wiley Online Library, v. 110, n. 464, p. 489–504, 1984.

WEISS, J. The dynamics of enstrophy transfer in two-dimensional hydrodynamics. *Physica D*, v. 48, p. 273–294, 1991.

YU, L.; WELLER, R. A. Objectively analyzed air–sea heat fluxes for the global ice-free oceans (1981–2005). *Bulletin of the American Meteorological Society*, v. 88, n. 4, 2007.